CALCULATION OF THE THERMODYNAMIC AND SPECTROSCOPIC QUANTITIES IN MOLECULAR CRYSTALS CLOSE TO THE PHASE TRANSITONS

A THESIS SUBMITTED TO
THE GRADUATE SCHOOL OF NATURAL AND APPLIED SCIENCE
OF
MIDDLE EAST TECHNICAL UNIVERSITY

BY

DİLAN KAVRUK

IN PARTIAL FULFILLMENT OF THE REQUIREMENTS
FOR
THE DEGREE OF DOCTOR OF PHILOSOPHY
IN
PHYSICS

FEBRUARY 2011

Approval of the thesis:

CALCULATION OF THE THERMODYNAMIC AND SPECTROSCOPIC QUANTITIES IN MOLECULAR CRYSTALS CLOSE TO THE PHASE TRANSITONS

submitted by **DİLAN KAVRUK** in partial fulfillment of the requirements for the degree of **Doctor of Philosophy in Physics Department, Middle East Technical University** by,

Prof. Dr. Canan Özgen _____
Dean, Graduate School of **Natural and Applied Sciences**

Prof. Dr. Sinan Bilikmen _____
Head of Department, **Physics**

Prof. Dr. Hamit Yurtseven _____
Supervisor, **Physics Dept., METU**

Examining Committee Members:

Prof. Dr. Şenay Katırcıoğlu
Physics Dept., METU _____

Prof. Dr. Hamit Yurtseven
Physics Dept., METU _____

Prof. Dr. Bekir Sıtkı Kandemir
Physics Dept., Ankara University _____

Assoc. Prof. Dr. Akif Esendemir
Physics Dept., METU _____

Assoc. Prof. Dr. Enver Bulur
Physics Dept., METU _____

Date: _____

I hereby declare that all information in this document has been obtained and presented in accordance with academic rules and ethical conduct. I also declare that, as required by these rules and conduct, I have fully cited and referenced all material and results that are not original to this work.

Name, Last name : Dilan KAVRUK

Signature :

ABSTRACT

CALCULATION OF THE THERMODYNAMIC AND SPECTROSCOPIC QUANTITIES IN MOLECULAR CRYSTALS CLOSE TO THE PHASE TRANSITONS

Kavruk, Dilan

Ph.D., Department of Physics

Supervisor: Prof. Dr. Hamit Yurtseven

February 2011, 92 pages

We study in this thesis work the spectroscopic and thermodynamic quantities of some substances such as ammonium halides (NH_4Cl, NH_4I), ferroelectric crystals of tris-sarcosine calcium chloride (TSCC), tris-sarcosine calcium bromide (TSCB), organic compounds of carbon tetrachloride (CCl_4) and s-triazine ($C_3N_3H_3$) close to the phase transitions. Various physical and chemical properties of those materials have been measured near the critical points and have been reported in the literature.

In this study, the spectroscopic parameters of the frequency shifts, intensity and bandwidths are calculated as functions of temperature or pressure near the phase transitions in ammonium halides using the experimental data from the literature. The spectroscopic parameters are related to the crystal volume and the specific heat in these compounds. The thermodynamic quantities of the specific heat, thermal expansion and the isothermal compressibility are also calculated in the solid and liquid phases of carbon tetrachloride using the experimental data.

In another part of this thesis work, we analyze the temperature dependence of the spontaneous polarization and the dielectric susceptibility at fixed pressures for TSCC and TSCB by using the experimental data from the literature. The temperature dependence of the damping constant for the s-triazine is also calculated here close to the I-II transition. We use the theoretical models on the basis of the observations in the literature to calculate the critical behaviour of these physical quantities and we compare the results with the observed data. Various experimental studies in the literature give us the opportunity to find the proper way of fitting the calculated and observed results.

This study gives us the chance of a better understanding of the critical behavior of the studied materials by verifying the values of some critical exponents and the types of transitions as expected by different theoretical models.

Keywords: Spectroscopic Parameters, Thermodynamic Quantities, Molecular Crystals, Phase Transitions, Raman Scattering

ÖZ

FAZ GEÇİŞİ YAKININDA MOLEKÜLER KRİSTALLERİN TERMODİNAMİK VE SPEKTROSKOPİK NİCELİKLERİNİN HESAPLANMASI

Kavruk, Dilan

Doktora, Fizik Bölümü

Tez Yöneticisi: Prof. Dr. Hamit Yurtseven

Şubat 2011, 92 sayfa

Bu tez çalışmasında amonyum halojenlerin (NH_4Cl, NH_4I), tris-sarkozin kalsiyum klorür (TSCC) ve tris-sarkozin kalsiyum bromür (TSCB) gibi ferroelektrik kristallerin, karbon tetraklorür (CCl_4) ve s-triazin ($C_3N_3H_3$) gibi organik bileşiklerden oluşan bazı maddelerin faz geçişi yakınında spektroskopik ve termodinamik niceliklerini çalışmaktayız. İncelenen maddelerin çeşitli fiziksel ve kimyasal özellikleri kritik nokta yakınlarında ölçülmüş ve literatürde rapor edilmiştir.

Bu çalışmada, literatürdeki deneysel veriler kullanılarak, amonyum halojenlerde frekans kayması, şiddet ve bant genişliği gibi spektroskopik nicelikler sıcaklık ya da basıncın fonksiyonu olarak hesaplanmaktadır. Bu bileşiklerdeki spektroskopik parametreler kristalin hacmi ve öz ısıyla ilişkilendirilmiştir. Ayrıca karbon tetraklorürün katı ve sıvı fazlardaki deneysel verileri kullanılarak öz ısısı, ısısal genleşmesi ve eşsıcaklıklı sıkıştırılabilirliği gibi termodinamik nicelikleri de hesaplanmaktadır.

Bu tez çalışmasının diğer bir bölümünde TSCC ve TSCB bileşikleri için sabit basınçlarda anlık polarizasyon ve dielektrik alınganlık değerlerinin sıcaklık

bağımlılığı incelenmektedir. Ayrıca s-triazin için sönüm sabitinin sıcaklık bağımlılığı da I-II faz geçişi yakınında hesaplanmaktadır. Bu fiziksel niceliklerin kritik davranışlarını hesaplamak için literatürde yer alan gözlemleri esas alarak teorik modelleri kullanmakta ve sonuçları yine gözlenmiş verilerle karşılaştırmaktayız. Literatürden alınan çeşitli deneysel çalışmalar bize hesaplanan ve literatürde gözlemlenen verileri örtüştürmek için kullanılacak doğru yöntemi bulma fırsatı vermektedir.

Bu çalışma bize çalışılan maddelerin kritik üs değerlerini ve faz geçişi türlerini farklı teorik modellerde öngörüldüğü biçimde doğrulayarak onların kritik davranışlarını daha iyi anlayabilme olanağı sunmaktadır.

Anahtar Kelimeler: Spektroskopik Parametreler, Termodinamik Nicelikler, Moleküler Kristaller, Faz Geçişleri, Raman Saçılması

ACKNOWLEDGMENTS

I would like to express my deepest gratitude to my supervisor Prof. Dr. Hamit Yurtseven. Without his endless support, encouragement, guidance, patience and understanding from the initial to the final level, it would not be possible to complete this work.

I owe an appreciation to my husband Fatih because of his heartening attitude and support under any circumstances during my life. My son Onur deserves a great gratitude for making me a happy mother in the period of this study. They both let me feel lucky. My sincere thanks are also for all other members of my family, especially for my mother and father for their continuous help in any respect.

TABLE OF CONTENTS

LIST OF FIGURES

LIST OF TABLES

CHAPTER 1

INTRODUCTION

1.1 Phase Transitions and Critical Phenomena

One of the most interested subjects of physical sciences is the change of phase in matter. Two distinct phases seem to be separate and the transition between them can occur suddenly. This abrupt change is observed at the critical point until which there is a homogeneous phase at the equilibrium. Below and after this point the stable phase exhibits continuous changes by varying the thermodynamic quantities such as temperature or pressure. The examples of the critical point can be the liquid-vapor transition temperature T_c, the Curie point of a ferromagnetic crystal at which the spontaneous magnetization occurs or the critical point of a binary fluid mixture above (or below) which the components mix homogeneously in all portions [1].

The first classification of phase transitions was Ehrenfest classification. In this scheme, the degree of transition was named according to lowest discontinuous derivative of the free energy [1,2]. First order phase transitions have the discontinuity in the first derivative of the free energy with respect to the temperature. In many solid-liquid or liquid-gas transitions the density (first derivative of the free energy with respect to the chemical potential) is discontinuous. When the first derivative is continuous and the second derivative is discontinuous, the degree of the transition is said to be second order. In

ferromagnetic phase transitions, magnetization (the first derivative of the free energy with respect to the field strength) is continuous as the temperature decreased but magnetic susceptibility (second derivative) is discontinuous.

The Ehrenfest classification was not including the case where a derivative of the free energy diverges such as the heat capacity in the ferromagnetic phase transition [1,2]. This approach left its place to a modern classification which is dividing the phase transitions into two classes similarly to Ehrenfest's scheme. According to this modern approach first order phase transitions involve a latent heat. The transition process occurs together with a large amount of absorption or release of energy and during the transition the temperature of the system remains constant. Mainly, two phases take place together as the transition occurs and hence, the dynamics of the system is hard to study. The second class transitions are the second order transitions which also called as continuous phase transitions. Ferromagnetic and superfluid transitions are second order transitions. There is not a latent heat in these transitions and they include divergent susceptibility and power-law decay correlations.

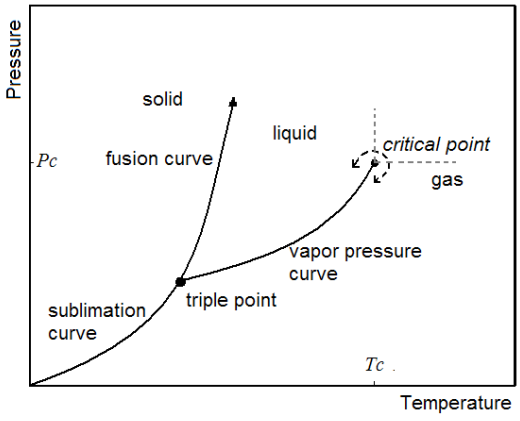

Figure 1.1 A typical fluid phase diagram.

In a solid-liquid-gaseous transition which is an example of the first order transition [3], the solid and gaseous phases are in equilibrium along the sublimation curve (line between solid and gaseous phases), the liquid and gaseous phases are in equilibrium along the vapor pressure curve (line between the liquid and gaseous phases) and the solid and liquid phases are in equilibrium along the fusion curve (line between the solid and liquid phases) [4]. On these curves, at any point two or more phases can exist together and they are in an equilibrium state. The triple point which is the intersection of these three curves represents a temperature and pressure combination that three phases coexist in an equilibrium state. Different from the fusion curve, the vapor pressure curve terminates at a point which is called the critical point. This means that one can change the state from liquid to gas without intersecting the phase transition line. The transition becomes second order at this point [2]. The coordinates of the critical point are denoted by T_c and P_c which are the critical temperature and the critical pressure, respectively. The term 'critical point' is used for the second order transitions.

The critical phenomena is associated with the second order (or continuous) transitions which deal with the critical points and critical exponents [2]. Continuous phase transitions are characterized by critical exponents. As we approach to the critical point, to describe the behavior of any quantity related to the temperature in the system, we use the function $f(T)\sim(T-T_c)^{\beta}$ with the exponent β. Other quantities depending on some other parameters may also have the similar behavior as $f(x)\sim(x)^{\beta}$. Here, β is the critical exponent. The temperature dependence is commonly studied with the dimensionless variable $\varepsilon \equiv \frac{(T-T_c)}{T}$ instead of $T-T_c$ [4]. The function $f(\varepsilon)$ is assumed to be positive for sufficiently small positive values of ε. This function is generally in the form [4]

$$f(\varepsilon) = A\varepsilon^{x}(1+B\varepsilon^{y}+...), \qquad (y>0).$$

Since the behavior of the leading terms dominate near the critical point, we focus on the critical exponents. This function f may be measured experimentally with respect to a thermodynamic parameter. Generally, the plot of these data displays

an abrupt behavior close to the critical point. The log-log plot of the experimental data gives a straight line near the critical point and the slope of this line is the critical exponent and there are many relations among these exponents [4]. These relations are a set of inequalities which does not differ between different systems. This is known as the universality of the critical exponents.

1.2 Properties of the Studied Materials

1.2.1 Ammonium Halides

Ammonium halides have many interesting structural and thermodynamic properties in terms their phase diagrams. In particular, NH_4Cl, NH_4Br and NH_4I exhibit varying orientational ordering and disordering of NH_4^+ ions [5]. In phase II, these ammonium halides are in cubic structure with halide ions, located at the corners of the unit cell. The H atoms are in a tetrahedral arrangement with the N atom at the center to form NH_4^+ ions. N atom is at the body center of a cubic structure and H atoms lie along the body diagonals. Ammonium ions have two energetically equivalent orientations with a difference by 90° rotation [6]. These two states are randomly distributed in phase II, therefore this phase is a orientationally disordered phase (β). As the temperature is decreased phase II changes into a ferro-ordered phase (δ) in which all the ammonium ions are parallel ordered. This transition is a λ-type phase transition [7]. It is continuous under a pressure of a few hundred megapascals, and in terms of the molecular orientations it is an order-disorder phase transition [5]. Many studies by using various techniques have been done to investigate the phase transitions in ammonium halides. Thermal conductivity and heat capacity measurements have been conducted under pressure [5]. The equilibrium transition temperature and activation energy for the α-β phase transition have been measured by dispersive powder diffraction [8]. Surface phase transition and temperature dependence of the lattice constant has been related to the order parameter in ammonium halides

near a tricritical point by x-ray diffraction [9]. Another study covering the measurements of the resistance in ammonium chloride, fluoride and bromide, conducted at a pressure range of 20-50 GPa and a temperature range of 77-400 K has been reported that all the ammonium halides show metal-like behavior under high pressures similar to that of alkali halides [10]. The order-disorder transitions in ammonium halides have been explained using theoretical models. An Ising pseudospin-phonon coupled model has been developed for ammonium halides [11]. A model with competing interactions between the NH_4^+ ions [12], an electrostatic model [13] and a microscopic model [14] have been reported.

1.2.1.1 Ammonium Chloride

Ammonium chloride (NH_4Cl) is a water-soluble white crystalline salt and found near the volcanoes in nature. It is used in manufacture of dry cells, fertilizing, metal cleaning materials, washing powders, and pharmacy. Its water solution is slightly acidic [15]. NH_4Cl is one of the most studied crystal in ammonium halides since it exhibits weakly first order, tricritical and second order phase transitions at 0, ~1.6 and ~2.8 kbar, respectively. The λ-type phase transition occurs at zero pressure (T_c=241 K), and it is weakly first order. At a higher pressure of ~1.6 kbar (T_c=257 K) the discontinuous character of the transition changes into a continuous one which is a tricritical phase transition. At ~2.8 kbar (T_c=268 K), a continuous transition takes place which is of a second order. All these transitions take place from the disordered β phase to the ferro-ordered δ phase as the temperature decreases. A master *P*-*T* phase diagram showing these β and δ phases has been obtained experimentally (Fig. 1.2) [16]. Theoretical phase diagrams of ammonium halides have been obtained in the literature [12,13]. Also pressure versus temperature (*P*-*T*) [17] and temperature versus concentration *T*-*X* [18] phase diagrams of ammonium halides have been obtained by using the mean field theory.

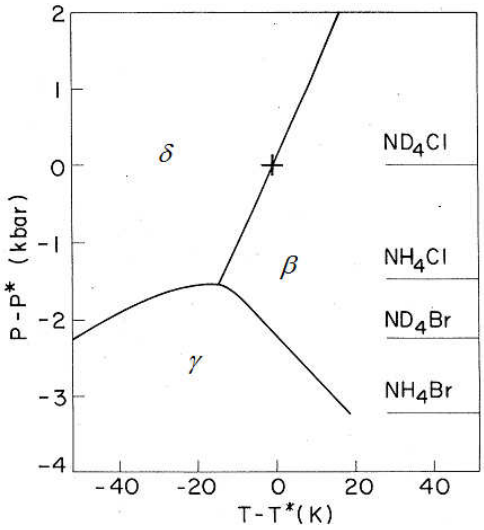

Figure 1.2 Master phase diagram for ammonium chloride and bromide [16]. The β-δ multicritical point P^*, T^* (indicated by + symbol) is at 3.2 kbar, 215.8 K for NH_4Br; 2.2 kbar 215 K for ND_4Br; 1.5 kbar, 256 K for NH_4Cl; 1 kbar 249.4 K for ND_4Cl. The location of P=0 is indicated for each salt.

First observations of the tricritical behavior of NH_4Cl were done by length-change measurements [19]. This is an intermediate transition between a first order at zero pressure and a second order at 2.8 kbar. Specific heat changes discontinuously at the first order transition (P=0), and continuously at the second order (P=2.8 kbar). The discontinuous and continuous changes occur together during the tricritical phase transition at P=1.6 kbar and T_c=257 K in NH_4Cl. The critical point behavior of the specific heat in NH_4Cl is described by a power law formula with a critical exponent. In ammonium halides, particularly NH_4Cl, the specific heat exhibits a similar behavior as the frequency shifts of phonons involved in the mechanism of the phase transition. The frequency shifts of the phonon modes below and above the critical temperature can be analyzed to deduce the critical exponent and then this exponent can be used to calculate the temperature dependence of the specific heat close to the phase transition.

1.2.1.2 Ammonium Iodide

Ammonium iodide (NH_4I) is a white crystalline powder which is used in medicines and photographic chemicals. The fumes generated by the decomposition of ammonium iodide solution irritate eyes and mucous membranes. It is soluble in water, alcohol and aqueous ammonia. Its crystal and solution turns into yellow when exposed to light or air due to the liberation of iodine [20]. At high temperatures phase I (α phase) has the NaCl structure. At atmospheric pressure and about 256 K temperature, it is in a disordered β phase (phase II) with a CsCl-type structure. Phases I and II have the $O_h^5 - F_m 3_m$ and $O_h^1 - P_m 3_m$ symmetries, respectively. As the temperature lowered the ammonium ions become ordered and the tetragonal ordered γ phase (phase III) occurs. In this phase NH_4^+ ions are parallel ordered along c axis and antiparallel-ordered in the a-b plane which creates an antiferro-ordered structure [21]. The following transition is to phase IV and it occurs at temperatures below 170 K. In this phase, the ammonium ions are completely parallel ordered along c axis and this causes a ferro-ordered structure [22]. The triple point width is given as P=5.5±0.1 kbar and T=170±2 K in the P-T phase diagram of NH_4I [23]. Phase V has been obtained at very high pressures (above 30 kbar) from the Raman spectrum of NH_4I [24]. A new phase at 110 K and atmospheric pressure has been suggested [25] using the Raman and infrared techniques and a P-T phase diagram has been obtained [26] including the phases II, III and IV by the mean field theory. Because of these various phase transitions, it is interesting to investigate the physical properties of NH_4I and many experimental techniques have been used for this system. Among the spectroscopic studies, the temperature-induced [22] and pressure-induced [27,28] I-II phase transitions have been studied by Raman spectroscopy. It is shown that the librational modes are the indicators to investigate the mechanism of the phase transition in NH_4I, since their Raman frequencies appear and disappear within small temperature regions. The librational mode (ν_6) and its

second harmonic ($2v_6$) have been observed in phase III and they both disappear in phase II as the temperature decreases [23].

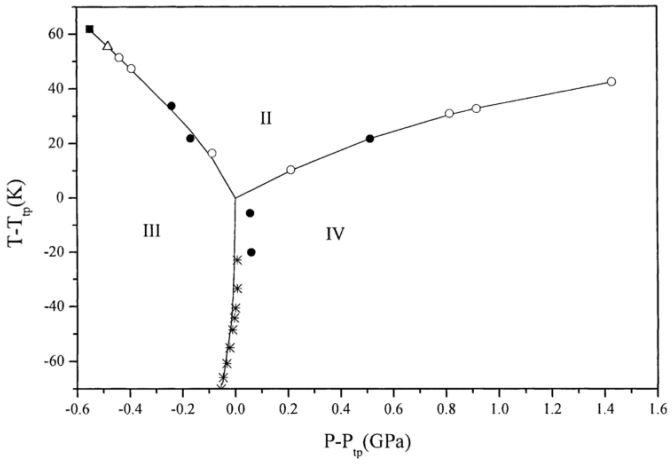

Figure 1.3 A phase diagram for ammonium iodide [26].

At low temperatures in phase IV, only the second harmonic ($2v_6$) has been observed. Also the lattice modes of TO (Γ) and LO (M) appear and disappear within a small pressure range at the transitions II-III-IV in NH_4I [23]. A new low temperature phase (110 K and 0 kbar) has been suggested from an experimental study [25] by the Raman and infrared spectra of the fundamental librational mode (v_6) and its overtone ($2v_6$) mode.

1.2.2 Organic Compounds

1.2.2.1 Tris-Sarcosine Calcium Chloride

Tris-sarcosine calcium chloride $(CH_3NHCH_2COOH)_3CaCl_2$ or TSCC is a uniaxial ferroelectric substance which is used as a model for many ferroelectricity studies. It exhibits ferroelectric phase transition under hydrostatic pressures [29]. The structure of this crystal is chemically important in the study of interactions

between aminoacids and some non-transition metal ions found in biological systems. TSCC belongs to a space group $D_{2h}^{16} - P_{nma}$ [30] and its low temperature (ferroelectric) space group is $C_{2v}^{9} - P_{n2_1a}$ [31]. In the paraelectric phase, it is orthorhombic with the four formula units per unit cell [30]. In the ferroelectric phase, it is also orthorhombic (Z=4) [32]. TSCC undergoes a ferroelectric phase transition at 127 K at atmospheric pressure, which is of a second order type [33]. By the dielectric susceptibility measurements a paraelectric-ferroelectric phase transition has been studied under hydrostatic pressures, and it is shown that the transition remains a second order [32,34] as in the case at 1 bar [35] through all the pressure range studied. The temperature dependence of the static dielectric constant ε, spontaneous polarization P(T) and the electric field dependence of the polarization P(E) in TSCC have been measured [36] regarding their behavior close to the paraelectric-ferroelectric phase transition. The critical exponents γ, β and δ for ε, P(T), P(E), respectively, have been determined from the experimental data according to the power law formulas.

1.2.2.2 Tris-Sarcosine Calcium Bromide

TSCB (Tris-sarcosine calcium bromide) or $(CH_3NHCH_2COOH)_3CaBr_2$ is another quantum ferroelectric under hydrostatic pressures [29] and it exhibits no ferroelectric phase transition down to liquid helium temperature [37]. Pressure effect on the ferroelectric phase transition has been investigated by dielectric measurements at various temperatures for constant pressures from 1 bar to 3 kbar [29]. At atmospheric pressure the dielectric constant remains at the same value between the temperatures 4.2 K and 50 K. In the same temperature range, at a higher pressure of 0.70 kbar a slight decrease occurs in the dielectric constant, but at 0.72 kbar a larger decrease in the dielectric constant has been observed around 6 K as an indication of a ferroelectric phase transition. However, λ- type peaks can be seen more clearly at higher pressures between 0.78 and 3 kbars which are the

evidence of ferroelectric phase transition. The dielectric anomaly increases together with the critical temperature with increasing pressure [29]. Another study has indicated that at a higher pressure of 7 kbar, critical temperature of the ferroelectric phase transition becomes 108 K [38].

1.2.2.3 Carbon Tetrachloride

CCl_4 or carbon tetrachloride is a harmful, clear liquid which is used in refrigeration fluids, aerosol cans, pesticides, detergents and fire extinguishers. It has a sweet smell. It is mostly found in the air as a colorless gas. It can cause kidney, liver and central nervous system damage if highly breathed or exposed by skin. [39]. It is not flammable but under high temperatures it is poisonous. For infrared spectroscopy it is sometimes used as a solvent [40]. At atmospheric pressure, carbon tetrachloride exhibits two phase transitions at 245 K and 225 K into its solid form; one from the phase Ia (face-centered cubic) to the phase Ib (rhombohedral) and the other from the phase Ib to the phase II (monoclinic). Many studies have been done to characterize these three phases [41-47]. At higher pressures phase III (monoclinic) [48] and phase IV (at 520 K and 2 GPa) [49] occur. Above 2 GPa, the Raman spectra have been obtained for this II-IV transition [50].

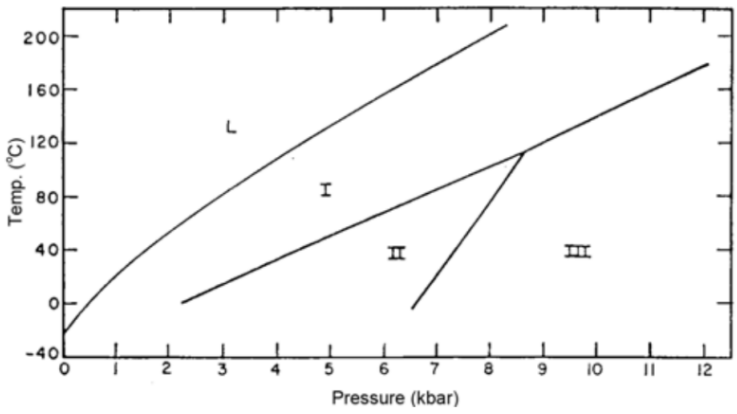

Figure 1.4 A *T-P* phase diagram of CCl_4 [51].

Two component systems have also been studied including CCl_4. For example, in $(CH)_3CCl_3$+CCl_4 [52], as the temperature decreases, methylchloromethanes changes from phase Ia to phase Ib. Both phases are orientationally disordered. The Raman and infrared measurements of $Cd(CN)_2CCl_4$ clathrate have been obtained from gaseous CCl_4 to its clathrate [53]. Also by X-ray powder diffraction and thermal analysis, the phase diagram between two halomethanes, CCl_4 and $CBrCl_3$, has been obtained for the system CCl_4+$CBrCl_3$ [54].

At high pressures, in the melting region of carbon tetrachloride, volume measurements have been done and its thermal expansivity has been measured at the fixed temperatures of 283, 301.5, 302, 325 K [55]. It has been indicated that CCl_4 undergoes a second order phase transition with the premelting effects as shown by the thermal expansivity α_p [55]. Divergence behavior of α_p has been described by a power-law formula near the melting point.

1.2.2.4 S-triazine

S-triazine ($C_3N_3H_3$) compounds have been used as herbicides for the weed control in agriculture. It is known that there is a weakly first order ferroelastic phase transition in s-triazine [56]. A *P*-*T* phase diagram of s-triazine is given in Fig. 1.5 [56]. At 198 K, the high temperature phase (phase I) with the rhombohedral crystal structure transforms into the low-temperature phase (phase II) with the monoclinic crystal structure [57,58]. Below this transition temperature, at 150 K, the crystal structure has been determined as the monoclinic structure from the X-ray diffraction measurements of the shear strain angle (order parameter) and the molecular rotation angle [59].

Another study has indicated that the transverse acoustic (TA) phonon with the wave vector in hexagonal direction and polarization along c-axis has a velocity at k=0, which is temperature dependent [60].

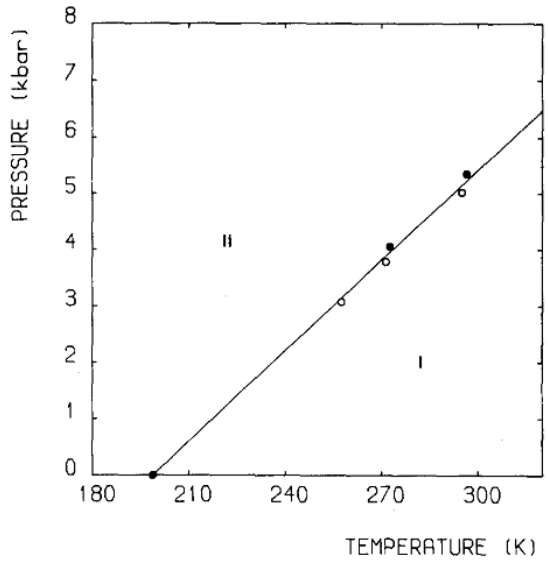

Figure 1.5 The phase diagram of s-triazine [56].

Its velocity becomes small at the transition temperature. On approaching the T_c, the elastic constant c_{44} corresponding to this shear mode is expected to vanish [61]. The transition is driven by this soft mode in the center of the Brillouin zone. The rhombohedral symmetry of the high- temperature low-pressure phase (phase I) is broken by two principal mechanisms [56]. First mechanism is the formation of a monoclinic unit cell by the spontaneous distortion of the unit cell as the temperature decreases below T_c (phase II). The second mechanism due to the small symmetry-breaking rotations of the molecules about axes perpendicular to the shear plane [56]. The ferroelastic I-II phase transition is accompanied by a soft acoustic mode which has been observed by coherent inelastic neutron scattering measurements [61,62] and in Brillouin scattering measurements[63]. This transition has also been described by the Landau phenomenological theory [64].

Different approaches concerning the microscopic origin of the ferroelastic phase transition in s-triazine have the common emphasis on the importance of coupling between the orientations of the molecules and the acoustic phonons [56].

CHAPTER 2

THEORY

2.1 Types of Phase Transitions

Many systems exhibit critical phenomena but the most familiar example of the critical point can be (*i*) the liquid-vapor transition at a characterictic temperature T_c, pressure P_c and density ρ_c. (*ii*) The Curie point is another example for the critical point in a system of a ferromagnetic (ferroelectric) crystal at which the spontaneous magnetization (electric polarization) occurs or the critical point of a (*iii*) binary fluid mixture or (*iv*) a binary metallic alloy above (or below) which the components mix homogeneously in all portions. (*v*) The Néel point of an antiferromagnet at which the alternating spin order goes to zero so that two phases become indistinguishable; (*vi*) the ordering temperature T_c of a binary crystal (*vii*) the lambda point of liquid Helium 4 (*viii*) the critical point of a superconductor [1].

Among these phase transitions, we mainly concentrate on the fluid, ferromagnetic and ferroelectric systems.

2.1.1 Fluid Systems

In a fluid system the equation of state is in the form $f(P,\rho,T) = 0$ and it relates the three thermodynamic parameters: pressure, density and temperature.

The relation between the pressure and temperature is usually represented by a *P*-*T* phase diagram of which an example was given in Chapter 1. In a typical fluid, *P*-*T* diagram, there are three separate regions, corresponding to the three phases of matter: solid, liquid and gas. The lines separating each of two phases are sublimation, vapor pressure and fusion curves as shown in Fig 1.1. Each of these curves consists of the points which represent an equilibrium state. The triple and critical points on this diagram were also defined in the previous chapter. We focus on the critical point existing on the liquid-gas transition line. It has the coordinates (P_c,ρ_c,T_c) which are the critical pressure, critical density and critical temperature, respectively. The *P*-ρ and ρ-*T* phase diagrams are also useful to understand the qualitative features of the critical point.

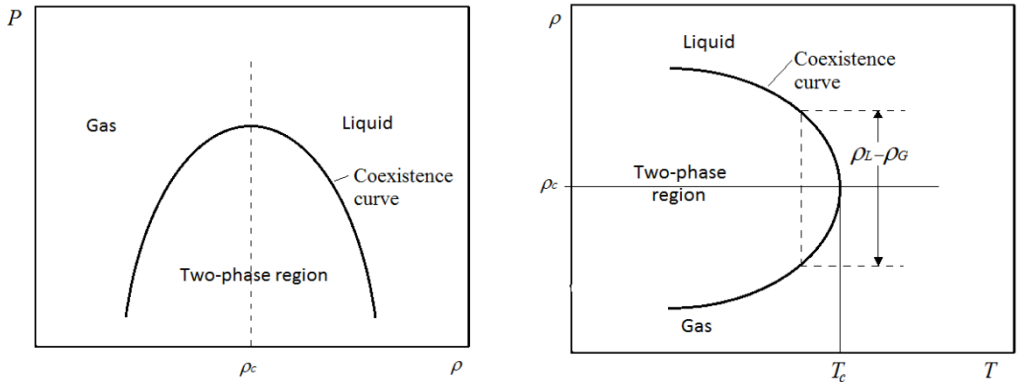

Figure 2.1 *P*-ρ and ρ-*T* diagrams for a typical liquid-gas transition.

Since ρ_L-ρ_G is non-zero only in the ordered phase it is called the order parameter for the liquid-gas critical point. We can define the critical exponent β by ρ_L- $\rho_G \sim (-\varepsilon)^{\beta}$ for $T<T_c$ with the dimensionless variable $\varepsilon \equiv \frac{(T-T_c)}{T_c}$ defined in the previous chapter. The value of this exponent is quite general (β=1/3) for different gas systems which is known as the universality of the critical exponents [1,4].

The divergence of the isothermal compressibility in a liquid-gas system characterizes the critical point. It is defined as

$$\kappa_T = -\frac{1}{V}\left(\frac{\partial V}{\partial P}\right)_T = \frac{1}{\rho}\left(\frac{\partial \rho}{\partial P}\right)_T . \qquad (2.1)$$

Then this divergence can be written as $\kappa_T \sim (-\varepsilon)^{-\gamma}$ while approaching the critical temperature T_c from the $T > T_c$ side.

2.1.2 Ferromagnetic Systems

The best way to understand the magnetic systems is usually to make analogy with the fluid systems. While applying pressure to a fluid system increases the density, applying magnetic field H to a ferromagnetic system increases the magnetization M. Here, magnetic field is analogous to pressure and magnetization is to density. Similarly, the equation of states in a magnetic system is given with the variables (H,M,T) which corresponds to the parameters (P,ρ,T) in the fluid system[4].

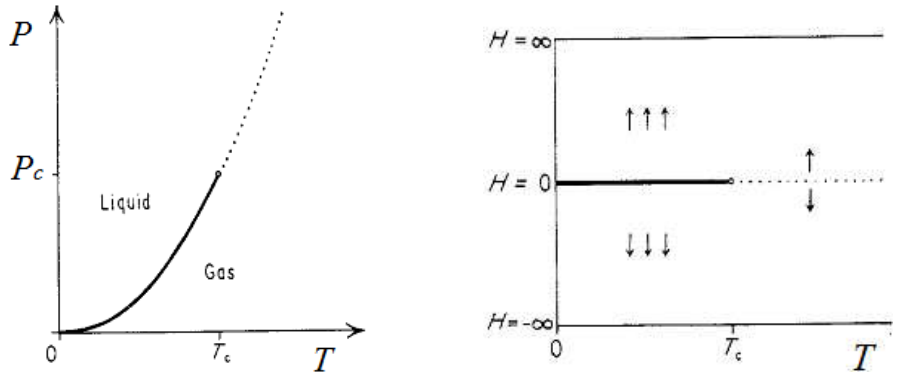

(a) (b)

Figure 2.2 A comparison of (a) the P-T phase diagram of a simple fluid, with (b) the H-T diagram for a simple ferromagnet.

The figure given above is a comparison of (a) the P-T phase diagram of a simple fluid, with (b) the H-T diagram for a simple ferromagnet. The

dotted lines above T_c represent the critical isochore ($P=P_c$) and critical isomomental (M=0), respectively. The arrows suggest the predominant spin configurations in different regions of the phase diagram [1].

The Curie temperature point at which a ferromagnetic material becomes a paramagnetic while the temperature is increasing. Below this critical temperature, system is under an internal magnetic field. As this magnetic field passes through zero, the equilibrium magnetization changes sign. Above T_c in the *paramagnetic* region the magnetization varies continuously as the magnetic field changes sign[1]. The order parameter is the magnetization M in a magnetic system which is analogous to the density in the fluid systems. Similar to that of fluid systems, the order parameter of the magnetic systems can be written as $M \sim (-\varepsilon)^{\beta}$ and the critical exponent β here again has a typical value in the range 0.3-0.5 [4].

The isothermal susceptibility is defined as

$$\chi_T = (\frac{\partial M}{\partial H})_T . \qquad (2.2)$$

Above the critical point T_c the isothermal susceptibility in zero field diverges as approaching the critical point. We can characterize this behavior as $\chi_T \sim (-\varepsilon)^{-\gamma}$ for $T>T_c$.

2.1.3 Ferroelectric Systems

Ferroelectricity is the feature of certain crystals which exhibit spontaneous electric polarization P that can be reversed by applying an external electric field E. [65]. The thermodynamic state of a ferroelectric system can be specified by the temperature T, the electric field E, and the polarization P. The polarization is the vector field that expresses the density of permanent or induced electric dipole moments in a dielectric material [66]. In a homogeneous linear and isotropic dielectric medium, the polarization P is aligned with and proportional to the electric field E:

$$P = \varepsilon_0 \chi E \tag{2.3}$$

where ε_0 is the electric permittivity of vacuum, and χ is the electric susceptibility of the medium. The electric susceptibility χ of a dielectric material is a measure of how easily it polarizes in response to an electric field.

Many properties of a ferroelectric phase transition is quite similar to those of found for liquid-gas and magnetic critical points. The behavior of the dielectric susceptibility characterizes the ferroelectric transition with the critical temperature above which the crystal becomes *paraelectric*. The term paraelectric suggests an analogy with paramagnetism: there is usually a rapid drop in the dielectric constant as the temperature increases[67]. The dielectric constant of an isotropic or cubic medium is defined in terms of the dielectric susceptibility as

$$\varepsilon = 1 + \chi \tag{2.4}$$

2.2 Critical Exponents and Critical Points

The investigations on the critical phenomena have been changed to focusing on the region near the critical point instead of looking at the whole phase diagram during 1964-1972 [4]. There are basically two reasons why we should focus on a quantity such as the critical exponent, which contains considerably less information than the complete functional form: *i*) The experimental results clearly show that the behavior of the leading terms dominates near the critical point. Therefore, the log-log plots of experimental data gives a straight line close to the critical point and the critical exponents are easily determined by the slope of this straight line. Hence, the critical exponent is measurable while the complete function may not be. *ii*) The second reason to focus on the critical exponents is that there are many relations between the exponents resulting from the thermodynamic and mechanical relations, and those relations are applicable for any system. The functional expression $f(\varepsilon)$ defined in Chapter 1 has different

behaviors in different systems, and its behavior has one-to-one relationship between the magnitude of the critical exponent near the critical point ($\varepsilon = 0$) [4].

The most commonly used critical exponent for fluid and magnetic systems are α, β, γ, δ, ν and η. In general, the same notation for a critical exponent is for the analogous fluid and magnetic functions, so that it is convenient to treat them together[4]. The temperature dependence of the liquid-gas density difference and the magnetization are analogous [4]:

$$\frac{\rho_L(T)-\rho_G(T)}{2\rho_c} = B(1-\frac{T}{T_c})^{\beta}(1+...)\,; \tag{2.5}$$

$$\frac{M_0(T)}{M_0(0)} = B(1-\frac{T}{T_c})^{\beta}(1+...)\,. \tag{2.6}$$

where M_0 is the zero-field magnetization. We can write shortly as ρ_L- $\rho_G \sim (-\varepsilon)^{\beta}$ and $M \sim (-\varepsilon)^{\beta}$. The constant B varies slightly between different systems because the density and magnetization are normalized by the constants ρ_c and $M_0(0)$. Also the isothermal compressibility and the isothermal susceptibility can be written as [4]:

$$\frac{\kappa_T}{\kappa_T^0} = \begin{cases} C'(-\varepsilon)^{-\gamma'}(1+...), & T<T_c, \quad \rho=\rho_L \text{ or } \rho_G \\ C\varepsilon^{-\gamma}(1+...), & T>T_c, \quad \rho=\rho_c \end{cases} \quad ; \tag{2.7}$$

$$\frac{\chi_T}{\chi_T^0} = \begin{cases} C'(-\varepsilon)^{-\gamma'}(1+...), & T<T_c, \quad H=0 \\ C\varepsilon^{-\gamma}(1+...), & T>T_c, \quad H=0 \end{cases} . \tag{2.8}$$

Here, κ_T^0 is the compressibility of an ideal gas of density ρ_c and χ_T^0 is the susceptibility of a system of non-interacting magnetic moments (paramagnet) at critical temperature T_c.

The specific heat can be expressed in terms of critical exponents as [4]:

$$C_V = \begin{cases} A'(-\varepsilon)^{-\alpha'}(1+...), & T<T_c, \quad \rho=\rho_L \text{ or } \rho_G \\ A\varepsilon^{-\alpha}(1+...), & T>T_c, \quad \rho=\rho_c \end{cases} \quad ; \tag{2.9}$$

$$C_H = \begin{cases} A'(-\varepsilon)^{-\alpha'}(1+...), & T < T_c, \quad H = 0 \\ A\varepsilon^{-\alpha}(1+...), & T > T_c, \quad H = 0 \end{cases}. \tag{2.10}$$

The remaining critical exponents δ, ν and η refer to the behavior of other physical quantities. δ is the exponent which characterizes the density dependence of the pressure along a liquid-gas critical isotherm, and also used for the temperature dependence of the magnetization in a magnetic system. ν and η describe the behavior of the pair correlation function $G(r)$ in the critical region.

The quantitative results have been found by many observations for the critical exponents. Although, the value of the critical temperatures vary from material to material, there is a similarity of the exponent values among the different experimental studies [4]. The following table gives a summary of the values of the critical exponents obtained from different observations [68].

Table 2.1 Experimental data on critical exponents.

Critical exponents	Magnetic systems	Fluid systems	Binary fluid mixtures	Binary alloys	Ferroelectric systems	Superfluid He	Mean field results
α,α'	0.0–0.2	0.1–0.2	0.05–0.15	– – –	– – –	–0.026	0
β	0.30–0.36	0.32–0.35	0.30–0.34	0.305 ± 0.005	0.33–0.34	– – –	1/2
γ	1.2–1.4	1.2–1.3	1.2–1.4	1.24 ± 0.015	1.0 ± 0.2	inaccessible	1
γ'	1.0–1.2	1.1–1.2	– – –	1.23 ± 0.025	1.23 ± 0.02	inaccessible	1
δ	4.2–4.8	4.6–5.0	4.0–5.0	– – –	– – –	inaccessible	3
ν	0.62–0.68	– – –	– – –	0.65 ± 0.02	0.5–0.8	0.675	1/2
η	0.03–0.15	– – –	– – –	0.03–0.06	– – –	– – –	0

It has been shown that there are certain quite general inequalities between the exponents α', β, γ' (for $T<T_c$), and δ [1]. In 1963, Rushbrooke derived the proof of the inequality $\alpha'+2\beta+\gamma' \geq 2$ for a ferromagnet [69], and later the corresponding analogy was set up for a fluid by Fisher[70] .

Another inequality was derived by Griffiths [71] as $\alpha'+\beta(1+\delta) \geq 2$ by directly using the convexity properties of the free energy.

2.3 Raman Spectroscopy

Raman spectroscopy is a method for measuring the vibrational, rotational or other low frequency waves in a molecule [72]. Monochromatic light is used to interact with the phonons in the system. Raman effect is an inelastic scattering involving two photons and one phonon. [73]. The incident photon excites the molecule from the ground state to a virtual energy state. Here, the excitation does not result in another discrete energy level as in the fluorescence (light emission with absorption of the energy). Then the molecule emits a photon and turns into another vibrational or rotational state. The scattering photon has a different energy state from the incident photon. This shift in the energy of the incident and scattered photons gives information about the phonon modes in the system. If the vibrational state of the molecule is higher than the initial mode, then the energy of the scattered photon must be lower than the incident photon which is called Stokes shift. If the scattering increases the photon energy, then the molecule will be in a lower vibrational mode, which is the anti-Stokes shift. The energy level diagram in Figure 2.3 shows the Rayleigh, Stokes and anti-Stokes shifts. The incident photon energy is $h\nu_0$ and the difference in the energy levels of the incident and scattered photons yield the change in the phonon mode of the target molecule.

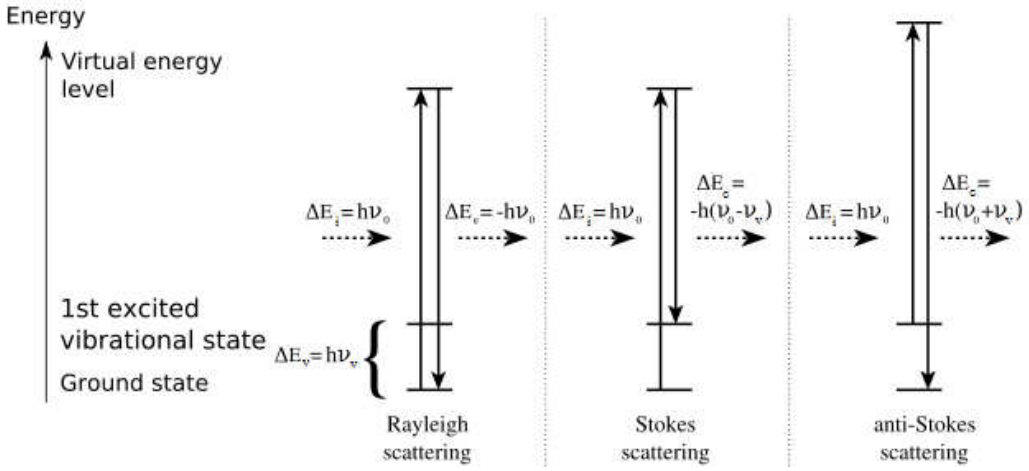

Figure 2.3 Energy level diagram for the Rayleigh, Stokes and anti-Stokes scatterings.

In a Raman spectrometer a lens is used to collect light from a sample illuminated by laser light. The collected beam is sent to a monochromator. The frequencies close to the laser are eliminated from the beam to filter the elastic Rayleigh scattering and the filtered light is sent to a detector. The main difficulty in Raman spectroscopy is to separate the weak inelastically scattered light from the intense elastically (Rayleigh) scattered light. For this filtering, laser rejecting filters or detectors are used.

2.4 Ising Model

An Ising model is a simplified lattice model which is first invented to describe the phase transition in ferromagnetics. It is also applicable to fluid systems. The model is defined on a discrete collection of spins S_i, which interact in pairs. Each site can be either empty or occupied by a spin in the lattice as shown in Fig. 2.4. Only the nearest neighbors interact. The Hamiltonian of the system can be defined as

$$H = -\sum_{ij} J_{ij} S_i S_j \tag{2.11}$$

where J_{ij} is the interaction term [74]. The product of the spins takes the value +1 if they are oriented in the same direction; -1 if they are in opposite directions or 0 if they are not interacting. This means the energy of the system is decreased by J if two neighboring spins are aligned, while it is increased if they are anti-aligned. The system is called to be ferromagnetic for the all spins aligned.

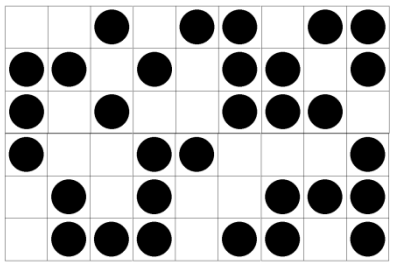

Figure 2.4 The illustrative description of the lattice with occupied and empty sites.

CHAPTER 3

CALCULATIONS AND RESULTS

3.1 Spectroscopic Calculations on Ammonium Halides Using Raman Frequency Data

3.1.1 Calculation of the Raman Frequencies Using Volume Data Close to the Tricritical and Second Order Phase Transitions in NH_4Cl

There are many theoretical models which explain the order-disorder phase transitions in ammonium halides. NH_4Cl is one of the most studied crystal among ammonium halides. In a previous study, λ transition of NH_4Cl and ND_4Cl at high pressures has been investigated by a mean field theory [75].

In this study, we used the data of the length-change measurements in the NH_4Cl crystal [19]. These measurements were done at the pressures of 0 (first order), 1636 (tricritical) and 2841 bars (second order), and the tricritical transition in NH_4Cl was first observed [19]. Here, we give a method [76] of calculating the Raman frequencies for the lattice mode of v_5 TO (174 cm^{-1}) and the internal mode of v_2 (1708 cm^{-1}) at higher pressures, namely, the pressures of 1636 bar (tricritical) and 2841 bar (second order) using the measurements of the length-change at 1 bar [19] in the NH_4Cl crystal [76]. The pressure dependent term was used to calculate the frequencies at higher pressures, and the Raman frequencies were evaluated as a function of temperature for the v_5 TO (174 cm^{-1}) and v_2 (1708 cm^{-1}) modes in the tricritical and second order regions through the length-change

data at zero pressure. Then, we compared these calculated Raman frequencies at the pressures of 1.6 and 2.8 kbars with the observed data for the v_2 (1708 cm^{-1}) mode [77] and v_5 TO (174 cm^{-1}) mode[78].

In a crystalline system, we can relate the vibrational frequency with the volume as a function of temperature by the equation

$$\gamma = -\frac{d\ln\nu(T)}{d\ln V(T)}. \tag{3.1}$$

In this equation, γ stands for the mode Grüneisen parameter and it defines the anharmonicity of the system. At constant pressure, we have the isobaric mode Grüneisen parameter,

$$\gamma_P = -\frac{V}{\nu}\frac{\left(\partial\nu/\partial T\right)_P}{\left(\partial V/\partial T\right)_P} \tag{3.2}$$

which is assumed to remain constant during the phase changes in the system. In order to obtain the temperature dependence of the frequency ν by using a constant mode Grüneisen parameter we solve Eq. (3.2) and modify it to higher pressures as

$$\nu_P(T) = \Delta_P + A(P) + \nu_1 \exp\left[-\gamma_P \ln\left(\frac{V_P(T)}{V_1}\right)\right] \tag{3.3}$$

where Δ_P is the order-disorder contribution to the vibrational frequency and $A(P)$ is the pressure-dependent term which can be written as

$$A(P) = a_0 + a_1 P + a_2 P^2 \tag{3.4}$$

as it has also been introduced in an earlier study [79]. Here, ν_1 and V_1 are the frequency and the volume at T=296 K, P=0. a_0, a_1, and a_2 are constants and they can be obtained from the initial data for the frequency and the volume. We used the length-change data [19] (L_P^T / L_1^{296}) for NH_4Cl to calculate the Raman frequencies as

$$\nu_P(T) = \Delta_P + A(P) + \nu_1 \exp\left[-3\gamma_P \ln(L_P(T)/L_1)\right] \tag{3.5}$$

by replacing the volume term by length in Eq. (3.4). Here, L_1 stands for the length

value at room temperature (T=296 K). Calculation of the Raman frequencies for the lattice mode v_5 (174 cm^{-1}) and the internal mode v_2 (1708 cm^{-1}) by Eq. (3.5) requires the initial volume (or length-change) data for those modes as a function of temperature for the pressures of zero (weakly first order), 1.6 kbar (tricritical) and 2.8 kbar (second order) [19], respectively, for NH_4Cl.

Using only the volume data obtained at atmospheric pressure at various temperatures, we predicted here the Raman frequencies for the lattice mode of v_5 TO (174 cm^{-1}) and the internal mode of v_2 (1708 cm^{-1}) at the pressures of 1.6 kbar (tricritical) and 2.8 kbar (second order) in NH_4Cl. For this prediction of the Raman frequencies, we first determined the coefficients a_0, a_1 and a_2 given in the pressure-dependent term $A(P)$ (Eq. 3.4). As the initial data we used our observed values of the Raman frequencies (Table 3.1) for the v_5 TO (174 cm^{-1}) and the v_2 (1708 cm^{-1}) at 260 K for P=0, 1.6 kbar and 2.8 kbars [78,79] and the observed values of the length-change at 260 K for P=1 bar [19] in Eq. (3.5).

Table 3.1 Observed values of the length-change [19], and of the Raman frequencies for the v_5 (174 cm^{-1}) [78] and v_2 (1708 cm^{-1}) [77] modes. The transition temperatures T_c for the weakly first order (1bar), tricritical (1636 bar) and the second order (2841 bar) from the length-change data [19] and from the observed frequencies [77,78] are given. Values of the order-disorder contribution Δ_P to the v_5 and v_2 modes, are also given here.

P (bar)		1	1636	2841
Length change T_c (K) [19]		242.90	257.17	266.60
Observed frequencies T_c (K) [77,78]		242.5	260.2	268.6
L_P^T / L_1^{296}		0.99816	0.99500	0.99149
v_5 (174 cm^{-1})		169.89	177.46	180.57
Δ_P v_5 (cm^{-1})	$T<T_c$	0.70	0.50	3.30
	$T>T_c$	-	-	3.30
v_2 (1708cm^{-1})		1709.26	1710.50	1711.36
Δ_P v_2 (cm^{-1})	$T<T_c$	0.45	0.60	1.90
	$T>T_c$	0.27	0.90	2.40

We used the constant values of the mode Grüneisen parameter γ_P for the v_5 TO (174 cm^{-1}) and v_2 (1708 cm^{-1}) modes which have been determined at zero pressure previously [77] with the observed values of v_1 and V_1 (T=296K, P=0), (Table 3.2) to evaluate a_0, a_1 and a_2 according to Eq. (3.5), as tabulated in Table 3.2.

Table 3.2 Values of the coefficients a_0, a_1 and a_2 according to Eq. (3.5). Values of the mode Grüneisen parameter γ_P , and the Raman frequencies v_1 at 296 K (1 bar) for the v_5 (174 cm^{-1}) and v_2 (1708 cm^{-1}) modes of NH_4Cl are also given here.

Raman mode	γ_P	v_1 (cm^{-1})	$-a_0$ (cm^{-1})	a_1(cm^{-1}/bar)	$-a_2$(cm^{-1}/bar^2)
v_5 (174 cm^{-1})	2.523	167.86	0.330	4.09×10^{-3}	1.21×10^{-6}
v_2 (1708 cm^{-1})	0.135	1708.61	0.625	-1.61×10^{-4}	2.59×10^{-7}

Using the length-change data at P=1 bar [19] with the coefficients determined, we then predicted the Raman frequencies for the v_5 TO (174 cm^{-1}) and v_2 (1708 cm^{-1}) modes of NH_4Cl close to the tricritical and second order phase transitions at the pressures of 1636 and 2841 bars, respectively, as a function of temperature according to Eq. (3.5). Figs. 3.1 and 3.2 give the plots of the Raman frequencies

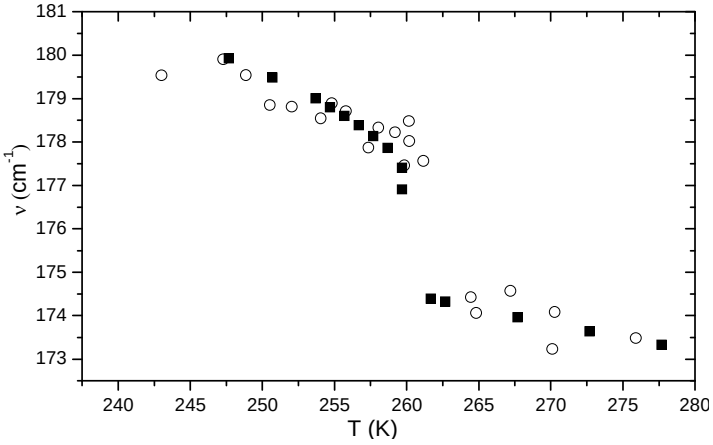

Figure 3.1 Raman frequencies calculated (■) as a function of temperature according to Eq. (3.5) for the lattice mode of v_5 TO (174 cm^{-1}) for the tricritical phase transition (P=1636 bar) in NH_4Cl. The observed (○) Raman frequencies [78] are also shown here.

calculated at various temperatures for the v_5 TO (174 cm^{-1}) mode of NH_4Cl at the pressures of 1636 and 2841 bars, respectively. Plots of the Raman frequencies for the v_2 (1708 cm^{-1}) mode which we calculated as a function of temperature at the same pressures (1636 and 2841 bars), are given in Figs. 3.3 and 3.4, respectively.

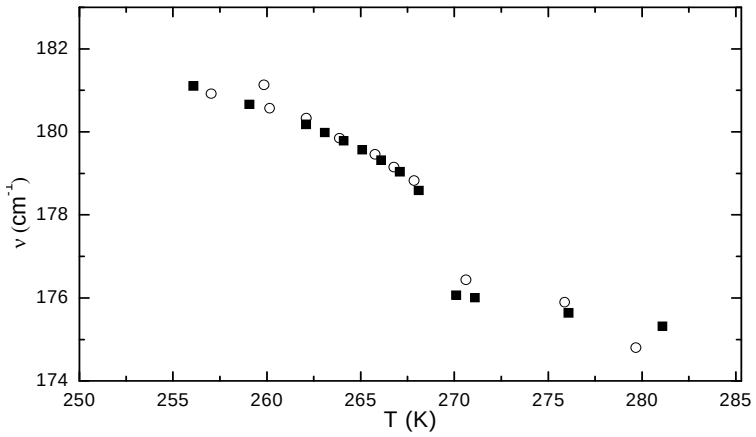

Figure 3.2 Raman frequencies calculated (■) as a function of temperature according to Eq. (3.5) for the lattice mode of v_5 TO (174 cm^{-1}) for the second order phase transition (P=2841 bar) in NH_4Cl. The observed (○) Raman frequencies [78] are also shown here.

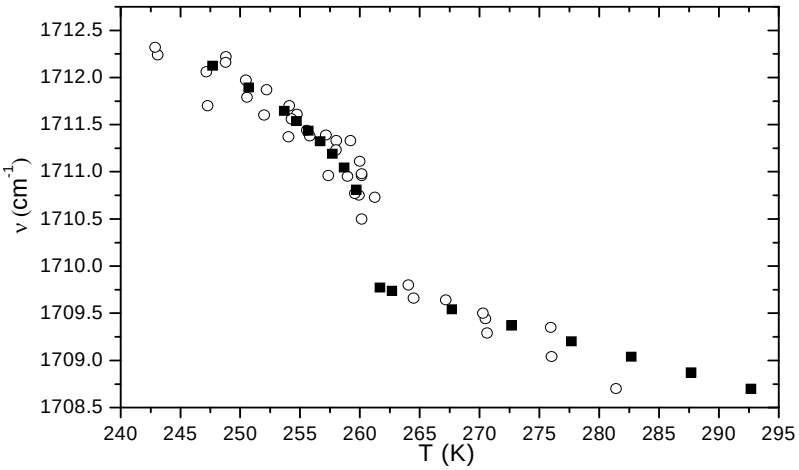

Figure 3.3 Raman frequencies calculated (■) as a function of temperature according to Eq. (3.5) for the internal mode of v_2 (1708 cm^{-1}) for the tricritical phase transition (P=1636 bar) in NH_4Cl. The observed (○) Raman frequencies [77] are also shown here.

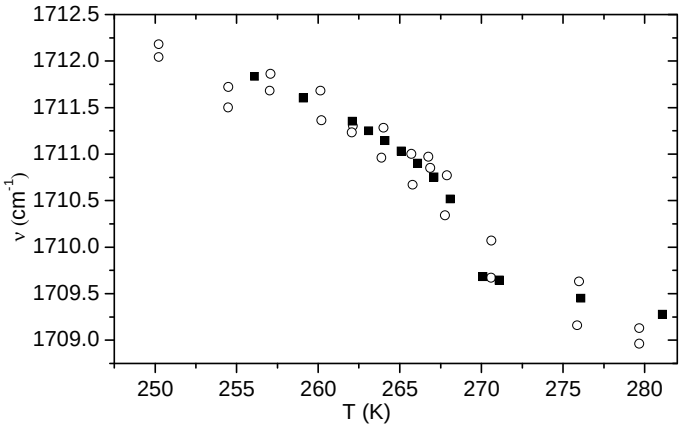

Figure 3.4 Raman frequencies calculated (■) as a function of temperature according to Eq. (3.5) for the internal mode of ν_2 (1708 cm^{-1}) for the second order phase transition (P=2841 bar) in NH_4Cl. The observed (○) Raman frequencies [77] are also shown here.

3.1.2 Calculation of the Specific Heat from the Raman Frequency Shifts Close to the Tricritical and Second Order Phase Transitions in NH_4Cl

Among the ammonium halides, NH_4Cl undergoes a tricritical phase transition at 1.6 kbar which has been experimentally studied before [19]. This is an intermediate transition between first (P=0) and second (P=2.8 kbar) orders. While the discontinuous changes occur in some thermodynamic quantities such as the specific heat during the first order transition, those changes can become continuous during the second order transition. Thus, both discontinuous and continuous changes are characteristic during the tricritical phase transition. We can describe the critical behaviour of the specific heat by a power-law formula using the critical exponent [80]. The critical exponent can be deduced from the frequency shifts of phonons which involve in the phase transition process. The frequency shifts with the temperature for a constant pressure can be described by a power-law formula

$$\frac{1}{\nu}\left(\frac{\partial \nu}{\partial T}\right)_P = A\varepsilon^{-a} \tag{3.6}$$

where a is the critical exponent for the frequency shifts, A is the amplitude and $\varepsilon=|T-T_c|/T_c$ is the reduced temperature.

The frequency shifts (change in the frequencies with the temperature at constant pressure) can be correlated with the thermodynamic quantities such as the thermal expansivity, the specific heat at constant pressure and the isothermal compressibility close to phase transitions. Since the frequency shifts can be described by a power-law formula with the critical exponent a (Eq. 3.6), the critical behaviour of those thermodynamic quantities can also be described by the same critical exponent a. To deduce the critical exponent a, we integrate both sides of the Eq. (3.6) to obtain

$$\ln(\nu/\nu_c) = \left(\frac{AT_c}{1-a}\right)\left|\varepsilon\right|^{1-a} \tag{3.7}$$

where ν_c is the critical frequency at the critical temperature T_c. Then we take the logarithm in Eq. (3.7);

$$\ln\left[\ln(\nu/\nu_c)\right] = \ln\left(\frac{AT_c}{1-a}\right) + (1-a)\ln\left|\varepsilon\right| \tag{3.8}$$

Thus, by plotting in a log-log scale $\ln(\nu/\nu_c)$ against $|\varepsilon|$ we can deduce [81] the critical exponent a for the frequency shifts $\frac{1}{\nu}\left(\frac{\partial \nu}{\partial T}\right)_P$ given in Eq. (3.6).

On the other hand, we can derive a power-law formula for the specific heat C_{VI} using the Ising free energy F_I as

$$F_I = A_0 + A_1\left|\varepsilon\right|^{2-a} \tag{3.9}$$

where A_0 and A_1 are constants. Then taking the second derivative of F_I with respect to the temperature, C_{VI} can be written as a power-law formula

$$C_{VI} = -J^2\frac{A_1 T}{T_c^{\,2}}(1-a)(2-a)\left|\varepsilon\right|^{-a} \tag{3.10}$$

where J is the interaction energy between the nearest-neighbour spins in an Ising system.

The critical exponent a extracted from the plot of Eq. (3.8) is the same as for the critical behaviour of the specific heat (Eq. 3.10) close to the tricritical (P=1.6 kbar) and second order (P=2.8 kbar) phase transitions in the NH_4Cl crystal [81]. The observed Raman frequencies of the ν_5 (174 cm^{-1}) mode were analyzed and plotted in the log-log scale (Eq. 3.8) as a function of temperature for the pressures of 1.6 and 2.8 kbars [81]. Table 3.3 gives our values of the critical exponent a for the frequency shifts $\frac{1}{\nu}\left(\frac{\partial \nu}{\partial T}\right)_P$ of the ν_5 (174 cm^{-1}) Raman mode in NH_4Cl within the intervals of the reduced temperature ε for the pressure of 1.6 kbar, which we extracted in an earlier work [81].

Using our exponent values (Table 3.3), we were then able to calculate the specific heat C_{VI} as a function of temperature for both tricritical (P=1.6 kbar) and second order (2.8 kbar) phase transitions in NH_4Cl.

Table 3.3 Values of the critical exponent a and J^2A_1 for the specific heat C_{VI} according to Eq. (3.10) below and above T_c for the tricritical (P=1.6 kbar, T_c=257.17 K) phase transition in NH_4Cl. Values of the critical exponent a were extracted from the Raman frequency shifts of the ν_5 (174cm^{-1}) mode within the interval of the reduced temperature ε in NH_4Cl [81]. Observed C_P values [82] for the temperatures which we used in our analysis (Eq. 3.10) are also given here.

P=1.6 kbar (T_c=257.17 K)	a	$-J^2A_1$ (J/mol)	$\varepsilon = \lvert T-T_c\rvert/T_c$	T(K)	C_P [82] (J/mol.K)
$T<T_c$	0.11	12290	$9.1\times10^{-3} < \varepsilon < 5.5\times10^{-2}$	250.71	117.49
$T>T_c$	0.11	7135.58	$7.4\times10^{-4} < \varepsilon < 7.3\times10^{-2}$	257.86	89.79

This calculation was performed according to a power-law formula (Eq. 3.10) for the specific heat C_{VI} on the basis of an Ising model. For this calculation of the specific heat C_{VI} close to the tricritical phase transition (P=1.6 kbar), we used the

same value of the critical exponent $a = 0.11$ below and above T_c from our analysis of the frequency shifts $\frac{1}{\nu}\left(\frac{\partial \nu}{\partial T}\right)_P$ for the ν_5 (174 cm^{-1}) Raman mode in NH_4Cl [81]. According to the specific heat relation (Eq. 3.10), we calculated C_{VI} as a function of temperature ($T<T_c$ and $T>T_c$) for the tricritical pressure (P=1.6 kbar, T_c=257.17K).

In order to calculate the specific heat C_{VI} at various temperatures for P=1.6 kbar in NH_4Cl, we used some observed C_P values [82] for the temperatures below and above T_c and our value of $a = 0.11$. We extracted the best-fitted values of J^2A_1, according to Eq. (3.10), as tabulated in Table 3.3. Thus, using those constant values of the critical exponent a and J^2A_1, we were then able to evaluate the specific heat C_{VI} as a function of temperature below and above T_c for the tricritical phase transition (P=1.6 kbar) in NH_4Cl, according to Eq. (3.10). Fig. 3.5 represents our plot of C_{VI} at various temperatures for P=1.6 kbar in NH_4Cl. Observed C_P data [82] obtained at 1.5 kbar (T_c=255.95 K) are also given in our plot.

Similarly, we calculated C_{VI} as a function of temperature using a power-law formula (Eq.3.10) for the second order phase transition in NH_4Cl (P=2.8 kbar). Using the values of $a = 0.18$ ($T<T_c$) and $a = 0.64$ ($T>T_c$), which were extracted from the analysis of our frequency shifts $\frac{1}{\nu}\left(\frac{\partial \nu}{\partial T}\right)_P$ for the ν_5 (174 cm^{-1}) mode in NH_4Cl at the pressure of P=2.8 kbar [81], as also given in Table 3.4, we were able to calculate the specific heat C_{VI} as a function of temperature for this pressure in NH_4Cl as well. For this calculation, as we also performed for P=1.6 kbar, we first determined the best-fitted value of J^2A_1 using some observed C_P data [82] below and above T_c for the temperatures, as given in Table 3.4.

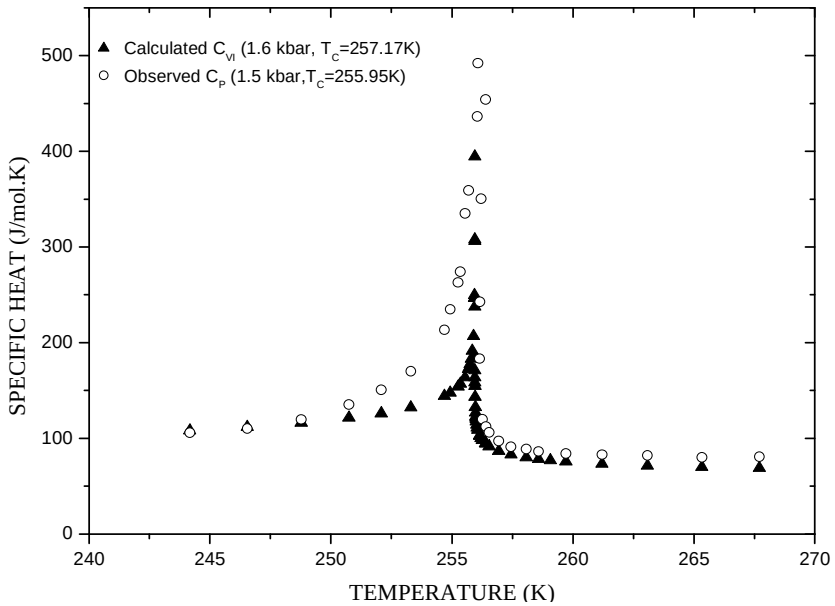

Figure 3.5 Specific heat C_{VI} calculated as a function of temperature according to Eq. (3.10) for the tricritical phase transition (P=1.6 kbar, T_c=257.17 K) in NH_4Cl. Values of the specific heat C_P measured [82] at 1.5 kbar (T_c=255.95 K) are also plotted here.

Table 3.4 Values of the critical exponent a and J^2A_1 for the specific heat C_{VI} according to Eq. (3.10) below and above T_c for the second order (P=2.8 kbar, T_c=266.6 K) phase transition in NH_4Cl. Values of the critical exponent a were extracted from the Raman frequency shifts of the ν_5 (174cm^{-1}) mode within the interval of the reduced temperature ε in NH_4Cl[81]. Observed C_P values [82] for the temperatures which we used in our analysis (Eq. 3.10) are also given here.

P=2.8 kbar (T_c=266.6K)	a	$-J^2A_1$ (J/mol)	$\varepsilon = \lvert T-T_c\rvert/T_c$	T(K)	C_P [82] (J/mol.K)
$T<T_c$	0.18	11178.80	$4.6\text{x}10^{-3}<\varepsilon<6.3\text{x}10^{-2}$	254.76	104.64
$T>T_c$	0.64	3058.21	$1.4\text{x}10^{-2}<\varepsilon<1.1\text{x}10^{-1}$	270	92.74

Those constant values of J^2A_1 were determined by Eq. (3.10). They were then used to calculate the specific heat C_{VI} at various temperatures below and above T_c according to Eq. (3.10) for the second order phase transition (P=2.8 kbar) in NH_4Cl.

In Fig. 3.6 we plot C_{VI} as a function of temperature for P=2.8 kbar in NH_4Cl (T_c =266.6 K). Observed C_P data [82] are also plotted here. In order to compare our calculated C_{VI} values with the C_P measured at the pressure of 3134 bar (T_c =268 K), we shifted our calculated C_{VI} values below T_c by 1.4 K. Thus, for the C_{VI} values (P=2.8 kbar), the transition temperature was taken as T_c =268 K, as determined for the observed C_P data (P=3134 bar) in our plot (Fig. 3.6).

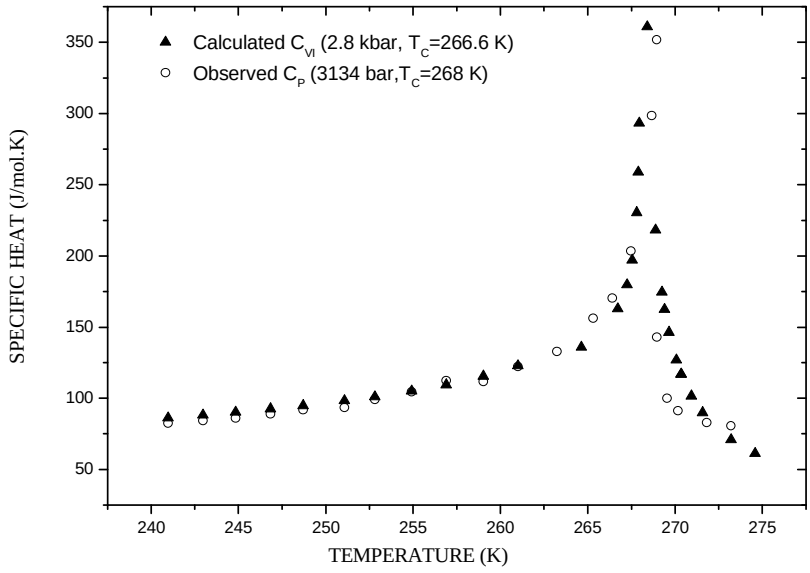

Figure 3.6 Specific heat C_{VI} calculated as a function of temperature according to Eq. (3.10) for the second order phase transition (P=2.8 kbar, T_c=266.6 K) in NH_4Cl. Values of the specific heat C_P measured [82] at 3134 bar (T_c=268 K) are also plotted here.

3.1.3 Calculation of the Raman Frequencies as a Function of Temperature in Phase II of NH_4I

Ammonium iodide exhibits various phase transitions at high pressures as indicated in Chapter 1. At atmospheric pressure it is in the NaCl-type disordered α phase (phase I) and it transforms into the CsCl-type disordered β phase (phase II) at about T=256 K (-16^{o}C). The tetragonal ordered γ phase (phase III) follows as the temperature is lowered down to T=232 K (-42 ^{o}C) in which the NH_4^+ ions become parallel-ordered along c axis and antiparallel-ordered in the a-b plane. This order gives rise to an antiferro-ordered structure [21]. The transition that follows is to phase IV (a ferro-ordered phase) at temperatures below 170 K in which the ammonium ions are completely parallel ordered along c axis [22].

In this study we mostly concentrated on phase II of ammonium iodide [83]. We calculated the Raman frequencies of the lattice mode ν_5 (125 cm^{-1}) as a function of temperature at 706, 1080 and 6355 bars [83]. In this calculation the volume data obtained at zero pressure, is used through the mode Grüneisen parameter for the disordered phase II (β phase) which has the CsCl structure of NH_4I. For the calculation of the Raman frequencies, we used a similar technique as in Part 3.1.1. We first considered the volume dependence of the vibrational frequencies by the mode Grüneisen parameter γ_i as

$$\gamma_i = -\frac{d(\ln \nu_i)}{d(\ln V)} \quad . \tag{3.11}$$

Under constant pressures and temperatures, the isobaric and isothermal mode Grüneisen parameters can be defined as

$$\gamma_P = -\frac{V}{\nu}\left(\frac{\partial \nu}{\partial V}\right)_P \tag{3.12}$$

and

$$\gamma_T = -\frac{V}{\nu}\left(\frac{\partial \nu}{\partial V}\right)_T \tag{3.13}$$

respectively. Using the definition of the thermal expansivity $\alpha_P \equiv (1/V)(\partial V/\partial T)_P$ and the isothermal compressibility $\kappa_T \equiv -(1/V)(\partial V/\partial P)_T$, the definitions of γ_P (Eq. 3.12) and γ_T (Eq. 3.13) can be written as

$$\gamma_P = -\frac{1}{\alpha_P}\frac{1}{\nu}\left(\frac{\partial \nu}{\partial T}\right)_P \tag{3.14}$$

and

$$\gamma_T = \frac{1}{\kappa_T}\frac{1}{\nu}\left(\frac{\partial \nu}{\partial P}\right)_T . \tag{3.15}$$

We obtain the volume dependence of the vibrational frequency with varying temperatures at constant pressures by solving Eq. (3.14) with the definition of the thermal expansivity α_P as

$$\nu_P(T) = A(P) + \nu_1 \exp\left[-\gamma_P \ln\left(\frac{V_P(T)}{V_1}\right)\right] \tag{3.16}$$

where the pressure dependent term $A(P)$ is defined as in Eq. (3.4) with the constants a_0, a_1 and a_2 . In Eq. (3.16) ν_1 and V_1 denote the values of the vibrational frequency and the crystal volume at a constant temperature, for example, at the room temperature. Thus, the vibrational frequencies can be predicted as a function of temperature by using the volume (or the lattice parameter) data for the crystals under study at constant pressures according to Eq. (3.16).

In this study we calculated the temperature dependence of the ν_5 (125cm^{-1}) and ν_7 (39 cm^{-1}) Raman modes of NH_4I at constant pressures of 706, 1080 and 6355 bars using the lattice parameter data [84] obtained at various temperatures between -3 and 39^{o}C at zero pressure for phase II (disordered phase) by Eq. (3.16). Since the volume of one primitive cell is $V=a^3$ in a CsCl type structure, we simply calculated the values of the molar volume by multiplying a^3 by the Avogadro's number, as given in Table 3.5.

Table 3.5 Observed lattice parameter data[84] and the crystal volume values atzero pressure for the disordered phase II of NH_4I.

T (^oC)	T (K)	Lattice parameter a (A^o) [84]	V (cm^3/mol)
-3	270	4.338	49.135
-10	263	4.337	49.109
-16	257	4.335	49.041
-21	252	4.334	49.007
-26	247	4.332	48.939
-29	244	4.332	48.939
-39	234	4.329	48.838

Then we calculated the vibrational frequencies for the ν_5 (125 cm^{-1}) and ν_7 (39 cm^{-1}) Raman modes at constant pressures by means of the pressure-dependent term $A(P)$. We determine the coefficients a_0, a_1 and a_2 using the initial data for the frequency ν and the volume V as given in Table 3.6 and assuming that the isobaric mode Grüneisen parameter γ_P was kept constant in the disordered phase II of NH_4I (Table 3.6).

Table 3.6 Values of the mode Grüneisen parameter γ_P and ν_1 for the Raman modes of ν_5 (125cm^{-1}) and ν_7 (39 cm^{-1}) at 1080 bar (T=300 K) [28], the observed volume V_1 extrapolated at 300 K (P=1 bar) [84], and the coefficients a_0, a_1 and a_2 according to the solution of Eq. (3.18).

	γ_P [28]	ν_1 (cm^{-1})	V_1 (cm^3/mol)	a_0 (cm^{-1})	$a_1\times10^{-3}$ (cm^{-1}/bar)	$a_2\times10^{-7}$ (cm^{-1}/ bar^2)
ν_5 (125 cm^{-1})	2.4	123	49.41	– 4.16	6.26	– 5.11
ν_7 (39 cm^{-1})	3.8	38	49.41	– 2.15	3.28	– 3.39

The initial volume and the frequency values were chosen according to the extrapolation of the observed results given in Table 3.5. Writing Eq. (3.16) for P=706 bar, we obtain

$$\nu_{706}(300K) = a_0 + a_1(706) + a_2(706)^2 + \nu_1 \exp\left[-2.4\ln\left(\frac{V_{706}(300K)}{V_1}\right)\right]. \quad (3.17)$$

Since the volume value was kept constant as V_1 at 300 K for zero pressure as given in Table 3.6, the exponential in the above equation gives unity and last term equals ν_1 which corresponds to the vibrational frequency value[28] for the pressures indicated at T=300 K (Table 3.7). Eq. (3.17) then becomes

$$\nu_{706} = a_0 + a_1(706) + a_2(706)^2 + \nu_1 \ . \tag{3.18a}$$

When we insert the other values of the observed frequency for two different pressures, we obtain

$$\nu_{1080} = a_0 + a_1(1080) + a_2(1080)^2 + \nu_1 \tag{3.18b}$$

and

$$\nu_{6355} = a_0 + a_1(6355) + a_2(6355)^2 + \nu_1 . \tag{3.18c}$$

This set of three equations gives the constants a_0, a_1 and a_2 for both ν_5 (125 cm^{-1}) and ν_7 (39 cm^{-1}) Raman modes, as given in Table 3.6. Eq. (3.18) was solved for the two Raman modes separately to obtain the constants a_0, a_1 and a_2 (Table 3.6).

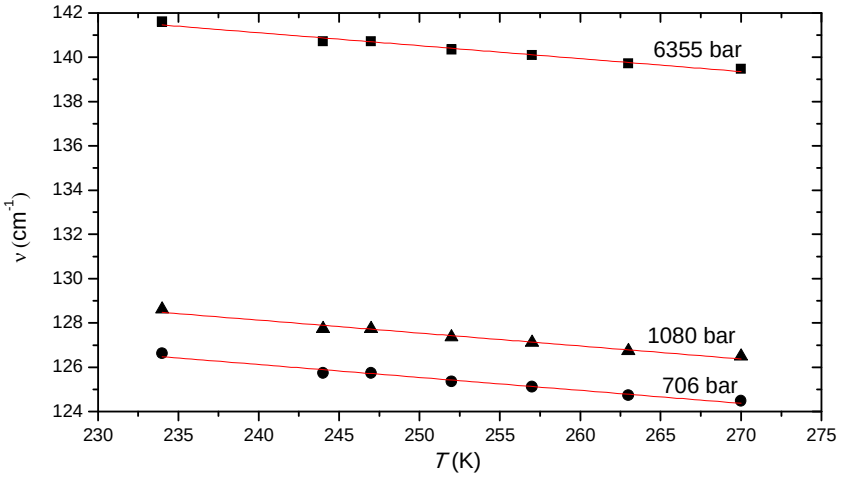

Figure 3.7 Calculated frequencies of the ν_5 (125 cm^{-1}) Raman mode as a function of temperature according to Eq. (3.16) in the disordered phase II of NH_4I for the constant pressures of 706 (●), 1080(▲) and 6355(■) bars. Deviations in the ν values are due to the observed volume data [84] which was used in Eq. (3.16).

Solid lines represent the best fit to the ν values with the parameters a and b (Table 3.7).

Using the a_0, a_1 and a_2 values together with the ν_1, V_1 and γ_P, we then calculated the frequencies for the two Raman modes of ν_5 (125 cm^{-1}) and ν_7 (39 cm^{-1}) as a function of temperature for fixed pressures of 706, 1080 and 6355 bars in the disordered phase II of NH_4I. Then we plotted the calculated frequency versus temperature for fixed pressures for both modes (Fig. 3.7 and Fig. 3.8).

The scattering of the calculated Raman frequencies is due to the deviation in the observed data. We obtained a linear fit for this data by the equation

$$\nu = aT + b \tag{3.19}$$

with the values of the slope a and the intercept b for the fixed pressures studied here, as given in Table 3.7.

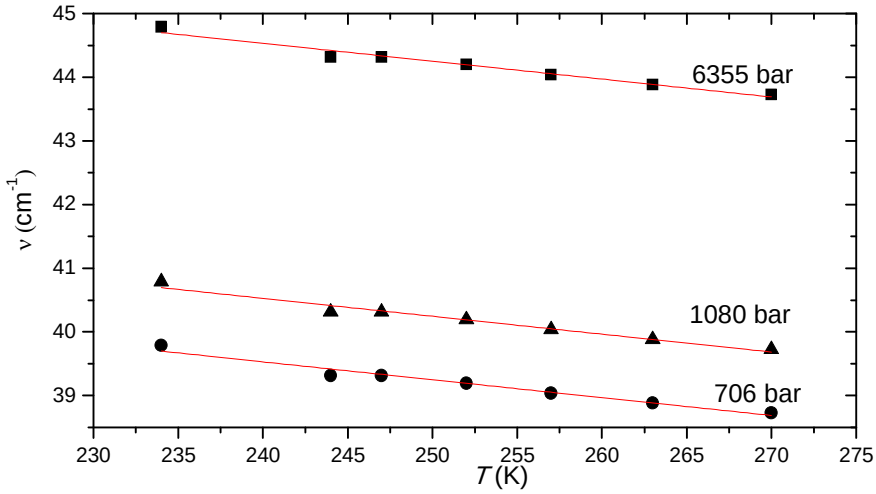

Figure 3.8 Calculated frequencies of the ν_7 (39 cm^{-1}) Raman mode as a function of temperature according to Eq. (3.16) in the disordered phase II of NH_4I for the constant pressures of 706 (●), 1080(▲) and 6355(■) bars. Deviations in the ν values are due to the observed volume data [84] which was used in Eq. (3.16).

Solid lines represent the best fit to the ν values with the parameters *a* and *b* (Table 3.7).

Table 3.7 Observed[28] values of the ν_5 (125 cm^{-1}) Raman mode of NH_4I in the disordered phase II according to Eq. (3.16) at 300 K for the pressures indicated. Values of the slope *a* and the intercept *b* from our calculated ν values (Eq. 3.19) are also given here.

	P (bar)	ν_{obs} (cm^{-1})	$-a$(cm^{-1}/K)	*b* (cm^{-1})
ν_5 (125 cm^{-1})	706	123	0.058	140.16
	1080	125		142.16
	6355	138		155.14
ν_7 (39 cm^{-1})	706	38	0.028	46.28
	1080	39		47.27
	6355	43		51.28

3.1.4 Calculation of the Raman Frequencies as a Function of Temperature in Phase III of NH_4I

The librational mode ν_6 and its second harmonic $2\nu_6$ are the indicators of the phase transition in NH_4I. These modes have been observed in phase III in small temperature and pressure intervals and they both disappear in phase II with the increase of the temperature [23]. Using a similar method given in Sec. 3.1.1, we calculated here the Raman frequencies for the overtone $2\nu_6$ of the librational mode ν_6 in phase III (tetragonal) of NH_4I as a function of temperature at zero pressure (*P*=0) [85]. This calculation was carried out by means of the volume dependence of the $2\nu_6$ mode frequency, which is defined as the isothermal mode Grüneisen parameter γ_P of this mode. Starting from Eq. 3.1 and considering the fixed pressure condition (*P*=0), we can write the temperature dependence of the Raman frequency of $2\nu_6$ as

$$\nu_P(T) = \Delta_P + \nu_1 \exp\left[-\gamma_P \ln\left(\frac{V_P(T)}{V_1}\right)\right] \tag{3.20}$$

where ν_1 and V_1 are constant values of the Raman frequency of $2\nu_6$ and the crystal volume, respectively. Δ_P is defined as the order-disorder contribution to the librational mode $2\nu_6$. Here, we used the experimental values of the lattice parameter (volume) [84] as the initial data, which is given in Table 3.8 for the phase III of NH_4I at low temperatures (P=0), and the values of the crystal volume obtained at various temperatures in this phase.

Table 3.8 Observed values of the lattice parameter a [84], the molar volume V and the infrared frequencies of the overtone $2\nu_6$ (I) of the librational mode ν_6 [25] in phase III (tetragonal) of NH_4I. Values of a and $V(=V_1)$ at 100 K were obtained by extrapolation. The V values were extracted from the lattice parameter a for the CsCl structure (bcc) of phase III in NH_4I.

T (K)	a (Å)	V (cm^3/mol)	$2\nu_6$ (I) (cm^{-1})
208	4.317	48.43	553.09
193	4.315	48.37	554.46
100	4.303	47.95	569.00

By working back from Eq. (3.20), the volume was obtained as a function of temperature according to the relation,

$$V_P(T) = V_1 \exp\left[-\frac{1}{\gamma_P} \ln\left(\frac{\nu_P(T) - \Delta_P}{\nu_1} \right) \right] \tag{3.21}$$

where the observed infrared frequencies[25] of the $2\nu_6$ (I) were used. For this calculation of the crystal volume in the temperature interval 100<T(K)<210, V_1 and ν_1 values were taken as extrapolations at 100 K, and the value of the mode Grüneisen parameter γ_P for the $2\nu_6$ mode [24], which we give in Table 3.9, were used in Eq. (3.21).

Table 3.9 Values of the volume, infrared frequency of $2\nu_6$ (I) (Table 3.8), the Raman frequency of $2\nu_6$ at 100 K and the isobaric mode Grüneisen parameter γ_P of $2\nu_6$ for NH_4I.

V_1 (cm^3/mol)	γ_P	ν_1 (cm^{-1}) of $2\nu_6$ (I)	ν_1 (cm^{-1}) of $2\nu_6$ (Raman)
47.95	0.22	569.0	560.0

The order-disorder contribution Δ_P to the overtone $2\nu_6$, as given in Eqs. (3.20) and (3.21), was taken as the temperature dependent according to the relation

$$\Delta_P = a + bT + cT^2 \tag{3.22}$$

where *a*, *b* and *c* are constants. Thus, by using the values of the crystal volume and the infrared frequencies of $2\nu_6$ (I) which are given in Table 3.8, the coefficients *a*, *b* and *c* were determined through Eq. (3.20), as given in Table 3.10.

Table 3.10 Values of the coefficients *a*, *b* and *c* for the order-disorder contribution Δ_P to the infrared $2\nu_6$ (I) and the Raman $2\nu_6$ (Eq. 3.22) in NH_4I.

Δ_P (cm^{-1})	*a* (cm^{-1})	*b* (cm^{-1}/K)	$c \times 10^{-4}$ (cm^{-1}/K^2)
Infrared $2\nu_6$ (I)	27.43	-0.338	6.43
Raman $2\nu_6$	-16.26	-0.021	3.20

Once, the coefficients *a*, *b* and *c* were determined, using the observed infrared frequencies of $2\nu_6$ [25], the volume values were predicted as a function of temperature according to Eq. (3.21). Fig. 3.9 gives the experimental infrared frequencies of the $2\nu_6$ (I) and $2\nu_6$ (II) modes [25] as a function of temperature (*P*=0).

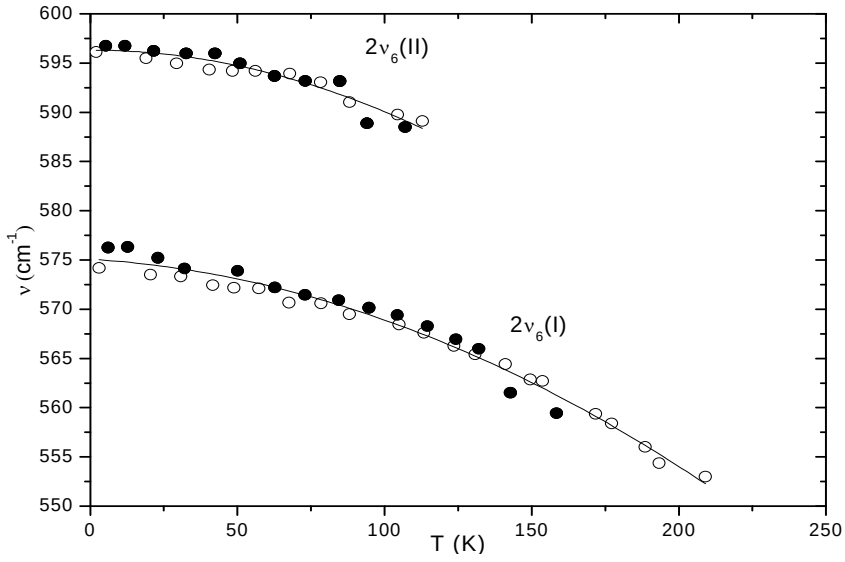

Figure 3.9 The observed infrared frequencies [25] of the overtone $2\nu_6$ (I) and $2\nu_6$ (II) as a function of temperature (*P*=0) in phase III (tetragonal) of NH_4I (● cooling down, ○ warming up).

The solid curves represent a fit to the experimental data according to the quadratic expression

$$\nu_P(T) = a_1 + b_1 T + c_1 T^2 \qquad (3.23)$$

with the values of the coefficients given in Table 3.11. Using the observed infrared frequencies of $2\nu_6$ (I) (Fig. 3.9) in Eq. (3.21), the values of the volume $V_P(T)$ were then calculated as a function of temperature.

Table 3.11 The best-fitted parameters a_1, b_1 and c_1 for the observed infrared values of the overtone $2\nu_6$ (I) and $2\nu_6$ (II) according to Eq. (3.23) in NH_4I (Fig. 3.9).

Infrared mode	a_1 (cm^{-1})	$-b_1 \times 10^{-3}$ (cm^{-1}/K)	$-c_1 \times 10^{-4}$ (cm^{-1}/ K^2)
$2\nu_6$ (I)	575.07	18.4	4.35
$2\nu_6$ (II)	596.31	0.60	6.19

The volume values which we calculated from the observed infrared frequencies of the $2\nu_6$ (I), were used to predict the Raman frequencies of this librational mode in phase III of NH_4I by means of Eq. (3.20). For this calculation, the values of V_1 and ν_1 at 100 K, and γ_P of the $2\nu_6$ (Table 3.9) were used in Eq. (3.20). By comparing with the observed Raman frequencies of the overtone $2\nu_6$ [25], we determined the Δ_P as the temperature-dependent above 110K. ,

This temperature dependence of Δ_P was determined using the three values of the observed Raman frequencies, as tabulated in Table 3.12 with the coefficients *a*, *b* and *c* which we give in Table 3.10 within the temperature interval 113.73<T(K)<209.15. Below 110 K, the order-disorder contribution to the overtone $2\nu_6$ was determined as a constant value of Δ_P = -30.6 cm^{-1} when compared with the observed Raman frequencies [25]. We plot our calculated (solid curve) Raman frequencies of the overtone $2\nu_6$ as a function of temperature in Fig. 3.10, with the observed Raman data [25].

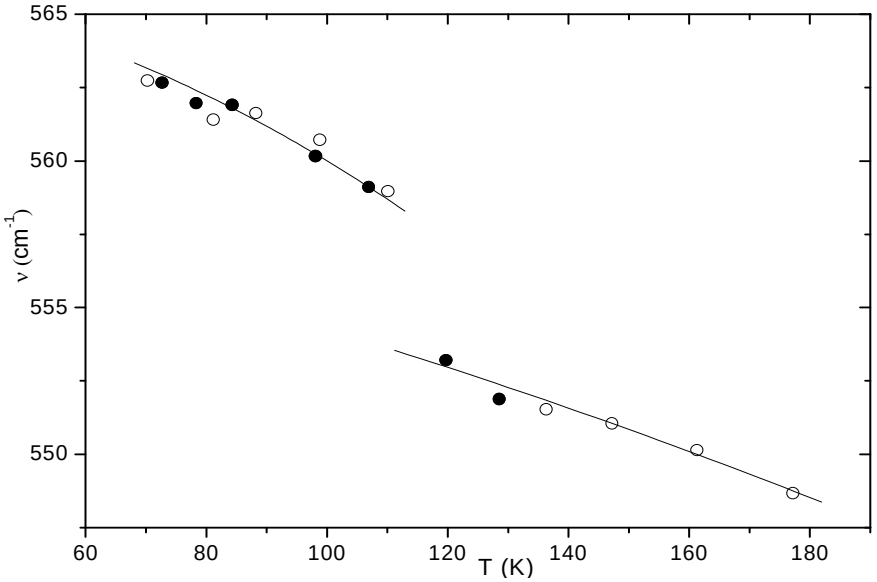

Figure 3.10 Raman frequencies calculated (solid curve) as a function of temperature for the overtone $2\nu_6$ according to Eq. (3.20). The observed Raman frequencies (● cooling down, ○ warming up) [25] of this mode are also plotted here.

Table 3.12 The observed Raman frequencies of the overtone $2\nu_6$, which were used in Eq. (3.20), with the calculated values to determine the order-disorder contribution Δ_P (Eq. 3.22) with the coefficients *a*, *b* and *c* (Table 3.10) in NH_4I.

T (K)	$2\nu_6$ (cm^{-1}) Observed	$2\nu_6$ (cm^{-1}) Calculated
119.14	553.27	558.28
146.64	551.15	554.40
176.98	548.75	549.60

3.2 Studies on Ferroelectric, Ferroelastic and Structural Phase Transitions in some Organic and Inorganic Compounds

3.2.1 Analysis of the Spontaneous Polarization and the Dielectric Constant Near the Ferroelectric Phase Transition in TSCC

The experimental analysis regarding the ferroelectric phase transition in TSCC (Tris-sarcosine calcium chloride or $(CH_3NHCH_2COOH)_3CaCl_2$) was done

and the temperature dependence of the dielectric constant was obtained at 0.001, 1 and 2.2 kbars [29]. Here, we performed [86] the analysis of the spontaneous polarization and the susceptibility for constant pressures of 0.001, 1 and 2.2 kbars using the experimental data for TSCC [29]. We describe the temperature dependence of the spontaneous polarization according to a power-law formula

$$P = A(T_c - T)^{\beta} \tag{3.24}$$

where β is the critical exponent for the spontaneous polarization (order parameter) and A is the amplitude. Taking the logarithm of both sides, we obtain a linear relationship between ln$P$ and ln(T_c-T) as

$$\ln P = \ln A + \beta \ln|T_c - T| \tag{3.25}$$

with the critical exponent β as the slope and the logarithm of the amplitude (ln$A$) as the intercept. From our analysis within the temperature interval studied, we extracted the values of β and the amplitude A, which are tabulated in Table 3.13. We plot the spontaneous polarization as function of temperature for 1 bar (T_c≈130 K), 1 kbar (T_c≈142 K) and 2.2 kbar (T_c≈155 K) in Fig. 3.11 according to our analysis (Eq. 3.24).

Table 3.13 Values of the critical exponent β for the spontaneous polarization P (order parameter) and the amplitude A within the temperature interval ΔT for the pressures indicated from our analysis of TSCC [29] according to Eq. (3.24) in the ferroelectric phase.

P (kbar)	T_c (K)	β	A (C/cm^2.K $^{\beta}$)	ΔT (K)= T_c-T
0.001	129.57	0.32	0.04098	0< ΔT < 29.57
1	142.17	0.28	0.04426	0< ΔT < 42.17
2.2	154.54	0.26	0.05507	0< ΔT < 54.54

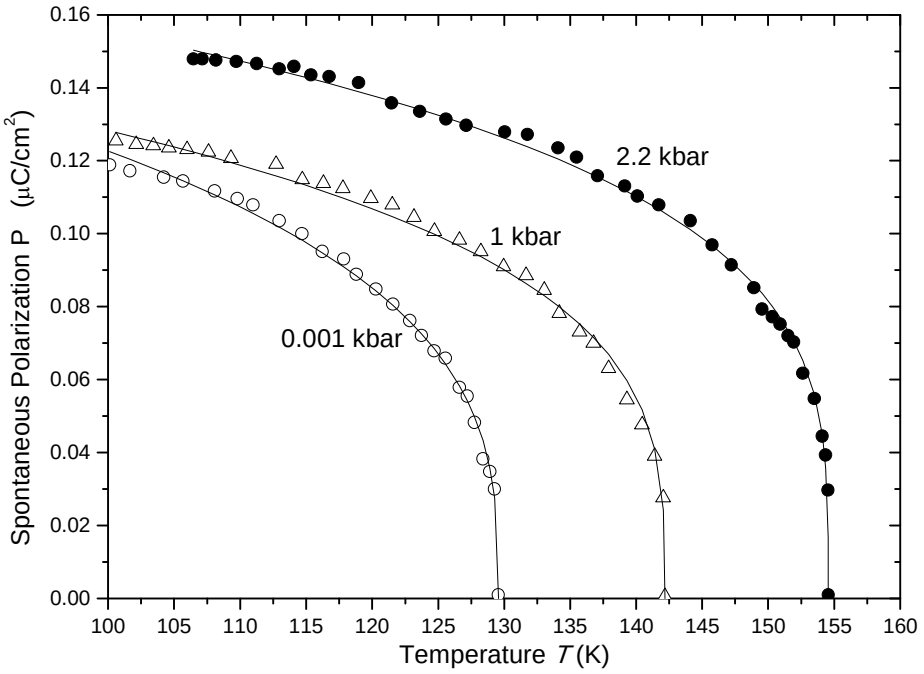

Figure 3.11 Spontaneous polarization (order parameter) as a function of temperature in the ferroelectric phase of TSCC at 1 bar (T_c=129.57 K), 1 kbar (T_c=142.17 K) and 2.2 kbar (T_c=154.54 K) [29] according to Eq. (3.24).

We also analyzed the temperature dependence of the susceptibility χ according to a power-law formula

$$\chi = B\left|T - T_c\right|^{-\gamma} \tag{3.26}$$

for TSCC. Using the observed data for this crystal at 1 bar, the values of the critical exponent γ and the amplitude B were extracted by taking the logarithm of both sides of Eq. (3.26)

$$\ln \chi = \ln B - \gamma \ln\left|T - T_c\right| \tag{3.27}$$

Table 3.14 gives those values of γ and B within the temperature interval ΔT below and above T_c. Figs. 3.12 and 3.13 give our linear plots of $\ln\chi$ against $\ln\left|T - T_c\right|$ for

1 bar, 1 kbar and 2.2 kbar below and above T_c, respectively. Using our exponent value for the susceptibility, the reciprocal dielectric constant $1/\varepsilon$ was calculated according to Eq. (2.4), as plotted as a function of T-T_c in Figs. 3.14-3.16 near the ferroelectric-paraelectric phase transition of TSCC at 1 bar, 1 kbar and 2.2 kbar, respectively.

Table 3.14 Values of the critical exponent γ for the susceptibility χ (dielectric constant ε) and the amplitude B within the temperature interval ΔT for the pressures indicated from our analysis of TSCC [29] close to the paraelectric-ferroelectric phase transition according to Eq. (3.27).

P (kbar)	T_c (K)	T (K)	γ	B (K^{γ})	ΔT (K)=$\lvert T-T_c \rvert$
0.001	129.57	$T<T_c$	1.00	30.99	$-2.91 < \Delta T < 0$
		$T>T_c$	1.01	22.19	$0 < \Delta T < 4.85$
1	142.17	$T<T_c$	1.03	48.78	$-2.94 < \Delta T < 0$
		$T>T_c$	1.17	32.55	$0 < \Delta T < 4.91$
2.2	154.54	$T<T_c$	1.11	74.48	$-2.85 < \Delta T < 0$
		$T>T_c$	1.14	32.42	$0 < \Delta T < 4.91$

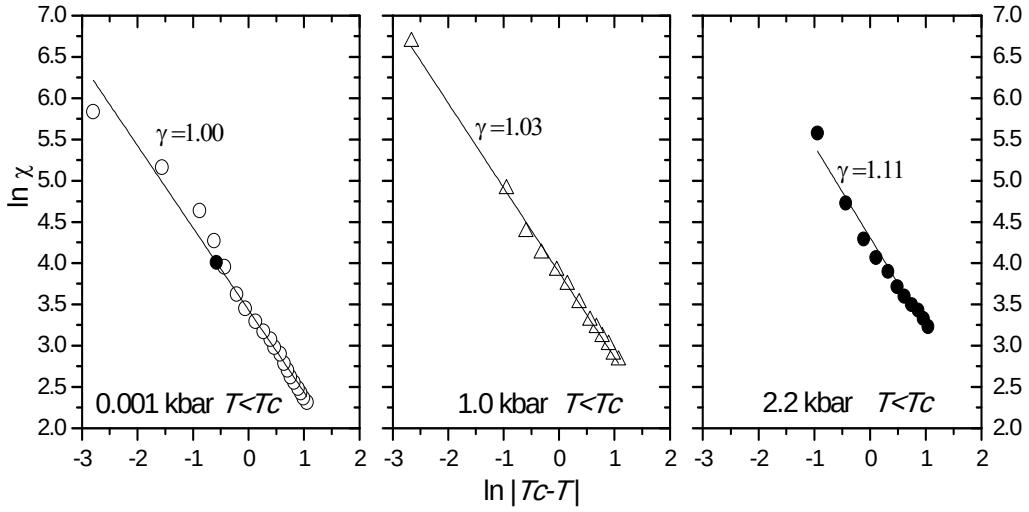

Figure 3.12 Log-log plot of the susceptibility χ against the temperature in the ferroelectric phase ($T<T_c$) of TSCC at 1 bar (T_c=129.57 K), 1 kbar (T_c=142.17 K) and 2.2 kbar (T_c=154.54 K) [29] according to Eq. (3.27).

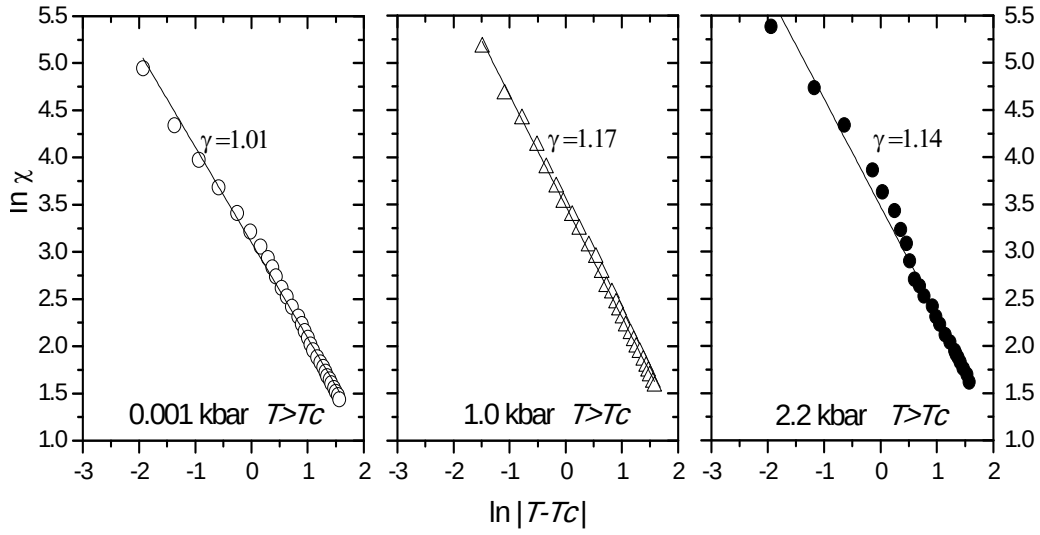

Figure 3.13 Log-log plot of the susceptibility χ against the temperature in the paraelectric phase ($T>T_c$) of TSCC at 1 bar (T_c=129.57 K), 1 kbar (T_c=142.17 K) and 2.2 kbar (T_c=154.54 K) [29] according to Eq. (3.27).

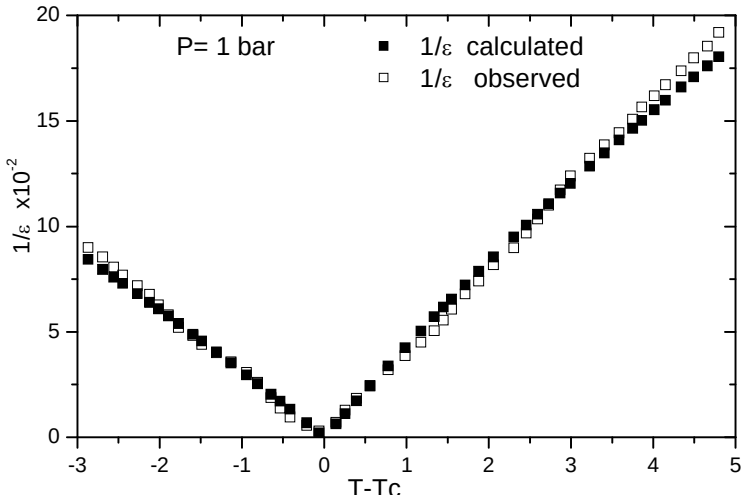

Figure 3.14 The reciprocal dielectric constant 1/ε obtained from the analysis of the observed data [29] according to Eq. (3.26) at 1 bar for TSCC near the ferroelectric-paraelectric phase transition (T_c=129.57 K).

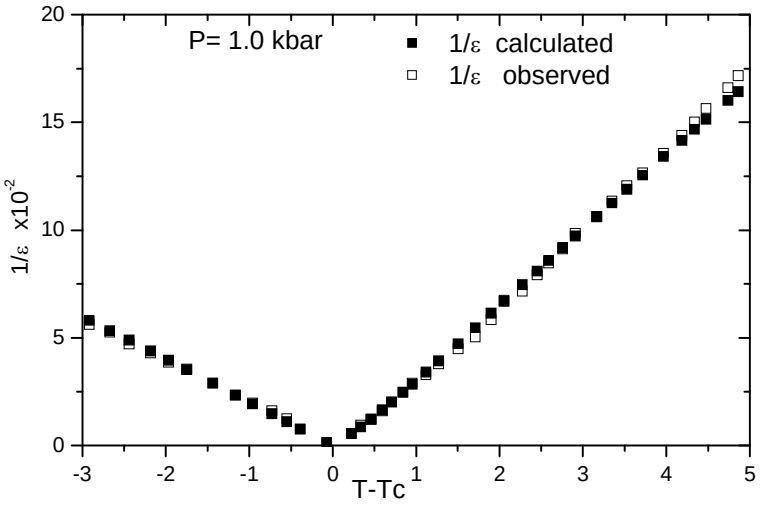

Figure 3.15 The reciprocal dielectric constant 1/ε obtained from the analysis of the observed data [29] according to Eq. (3.26) at 1 kbar for TSCC near the ferroelectric-paraelectric phase transition (T_c=142.17 K).

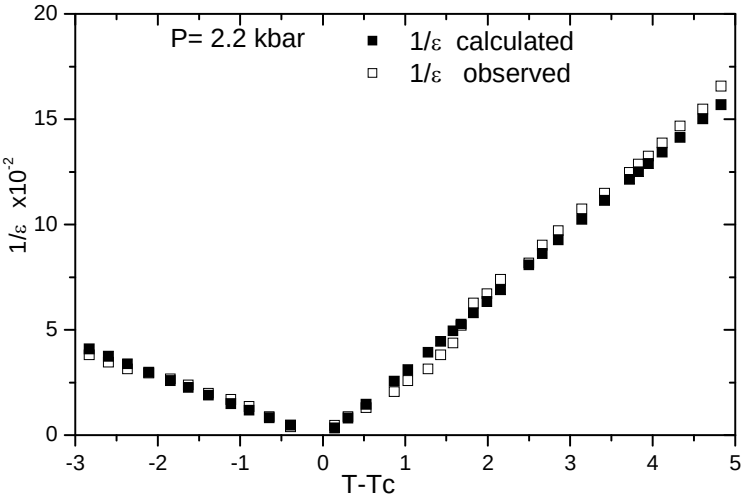

Figure 3.16 The reciprocal dielectric constant 1/ε obtained from the analysis of the observed data [29] according to Eq. (3.26) at 2.2 kbar for TSCC near the ferroelectric-paraelectric phase transition (T_c=154.54 K).

3.2.2 Analysis of the Spontaneous Polarization and the Dielectric Constant Near the Ferroelectric Phase Transition in TSCB

We analyzed the temperature dependences of the spontaneous polarization P and the susceptibility χ using the power-law formulae given by Eq. (3.24) and Eq. (3.26). According to Eq.(3.24), the spontaneous polarization (order parameter) increases in the ferroelectric phase (P=0 in the paraelectric phase) whereas the susceptibility χ diverges as the transition temperature is approached from both phases ($T<T_c$ and $T>T_c$) (Eq. 3.26).

We analyzed the experimental data for the spontaneous polarization of TSCB [87] at various temperatures for a fixed pressure of 2 kbar [29] using Eq.(3.25) and we plotted ln$P$ against ln(T-T_c) in Fig. 3.17.

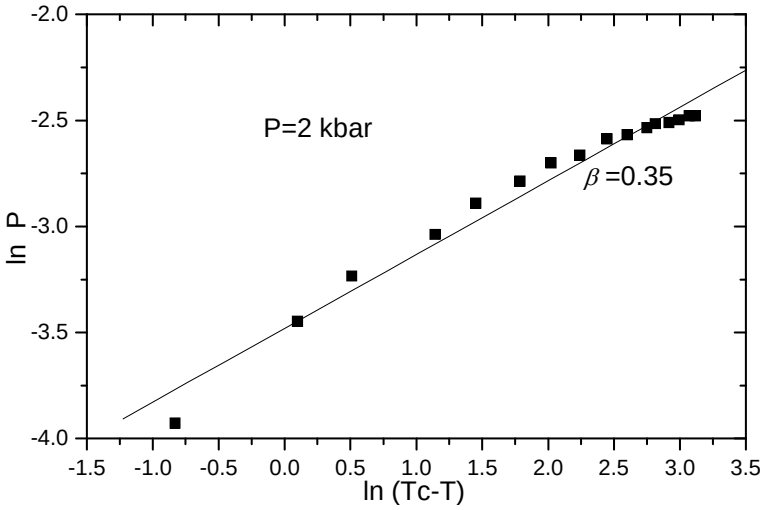

Figure 3.17 A log-log plot of the spontaneous polarization against the temperature in the ferroelectric phase of TSCB at P=2 kbar (T_c=47.2 K) [29] according to Eq. (3.25).

The slope value of β=0.35 was deduced from this plot as the value of the critical exponent for the order parameter (spontaneous polarization). Fig. 3.18 gives a

plot of the spontaneous polarization as a function of temperature for TSCB at 2 kbar [29].

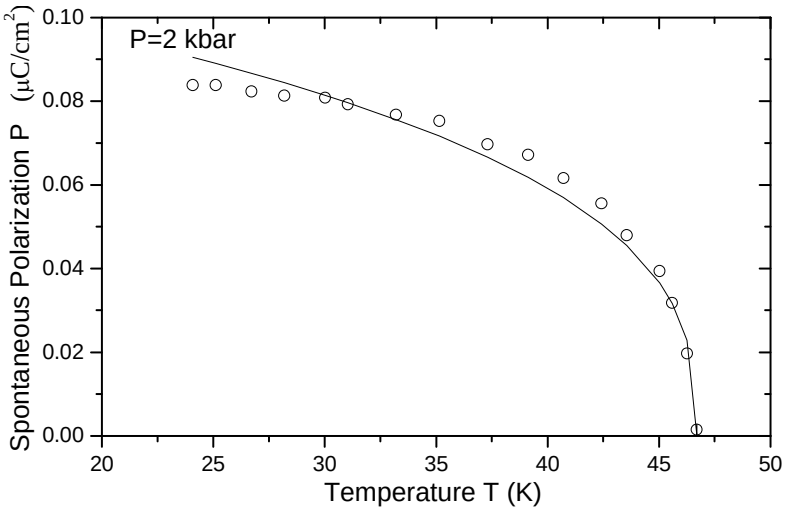

Figure 3.18 Spontaneous polarization (order parameter) as a function of temperature in the ferroelectric phase of TSCB at P=2 kbar (Tc=47.2 K) [[29] according to Eq. (3.24).

The solid curve represents the best fit to the experimental data according to Eq. (3.25). Table 3.15 gives the value of the amplitude *A*.

Table 3.15 The calculated values of the critical exponent β for the spontaneous polarization *P* (order parameter) and the amplitude *A* within the temperature interval ΔT for the pressure indicated from our analysis of TSCB [29] according to Eq. (3.25) in the ferroelectric phase.

P (kbar)	T_c (K)	β	*A* ($C/cm^2.K^{0.35}$)	ΔT (K)= T_c-T
2	47.2	0.35	0.03059	$0< \Delta T <22.2$

We also analyzed the temperature dependence of the susceptibility for constant pressures of 1, 2 and 3 kbars below above T_c close to the paraelectric-ferroelectric phase transition, according to Eq. (3.26). By fitting Eq. (3.27) to the experimental

data for the susceptibility χ for the pressures of 1, 2 and 3 kbars, we deduced the values of the critical exponent γ and also the amplitude B. Table 3.16 gives the values of γ and B with the transition temperatures for the pressures considered here.

Table 3.16 The calculated values of the critical exponent γ for the susceptibility χ (dielectric constant ε) and the amplitude B within the temperature interval ΔT for the pressures indicated from our analysis of TSCB [29] close to the paraelectric-ferroelectric phase transition according to Eq. (3.27).

P (kbar)	T_c (K)	T (K)	γ	B (K$^{\gamma}$)	ΔT (K)=$\lvert T-T_c \rvert$
1	15.7	$T<T_c$	1.17	77.20	$-2.97 < \Delta T < 0$
		$T>T_c$	0.77	54.88	$0 < \Delta T < 4.85$
2	47.2	$T<T_c$	1.0	653.21	$-2.94 < \Delta T < 0$
		$T>T_c$	1.42	70.77	$0 < \Delta T < 4.76$
3	64.3	$T<T_c$	1.0	173.93	$-2.96 < \Delta T < 0$
		$T>T_c$	0.98	59.30	$0 < \Delta T < 4.93$

In Fig. 3.19, we plot lnχ against ln$|T-T_c|$ below ($T<T_c$) and above ($T>T_c$) the transition temperature for P=1 kbar pressure from our analysis. A plot of the inverse dielectric constant ($1/\varepsilon$) against the temperature difference ($T-T_c$) is also given for TSCB at P=1 kbar in Fig. 3.20.

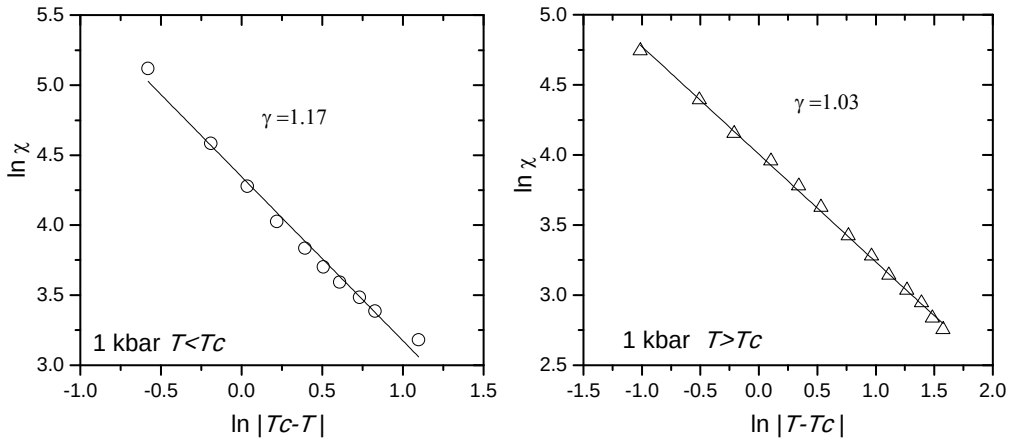

Figure 3.19 Log-log plots of the susceptibility χ against the temperature in the ferroelectric phase ($T<T_c$) and paraelectric phase ($T>T_c$) of TSCB at P=1 kbar (T_c=15.7 K) [29] according to Eq. (3.27).

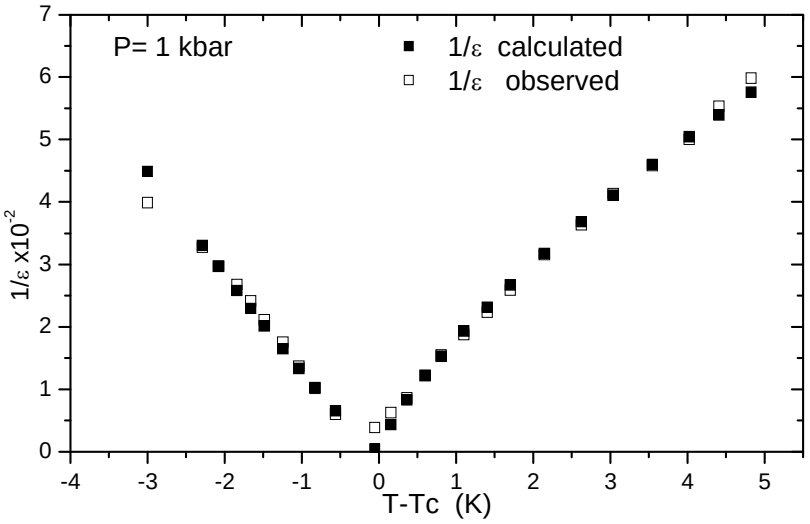

Figure 3.20 The inverse dielectric constant $1/\varepsilon$ obtained from the analysis of the observed data [29] according to Eq. (3.26) at P=1 kbar for TSCB close to the paraelectric-ferroelectric phase transition (T_c=15.7 K).

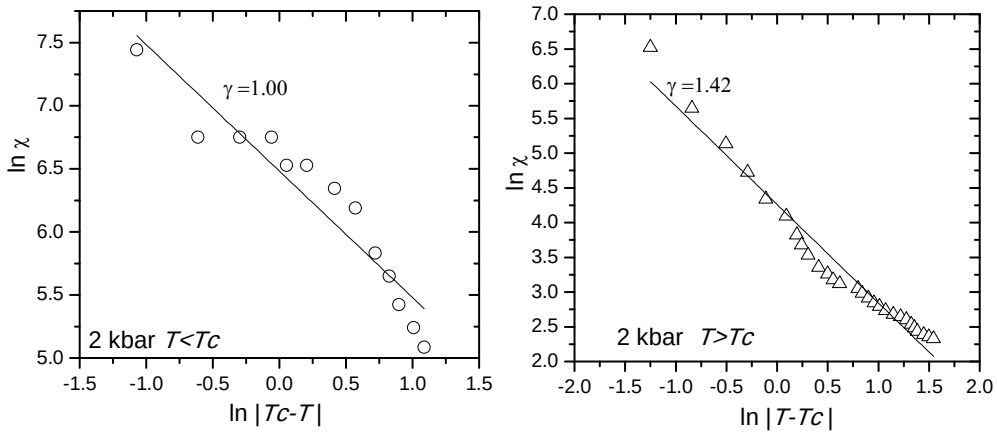

Figure 3.21 Log-log plots of the susceptibility χ against the temperature in the ferroelectric phase ($T<T_c$) and paraelectric phase ($T>T_c$) of TSCB at P=2 kbar (T_c=47.2 K) [29] according to Eq. (3.27).

The analysis of the temperature dependence of the susceptibility was carried out at 2 kbar for TSCB according to Eq. (3.27). From our analysis below and above T_c, the values of γ and B which we deduced, are tabulated in Table 3.16. Log-log plots of χ against T-T_c are given in Fig. 3.21 below and above T_c,

respectively. Fig. 3.22 gives the inverse dielectric constant ($1/\varepsilon$) as a function of T-T_c at 2 kbar for TSCB.

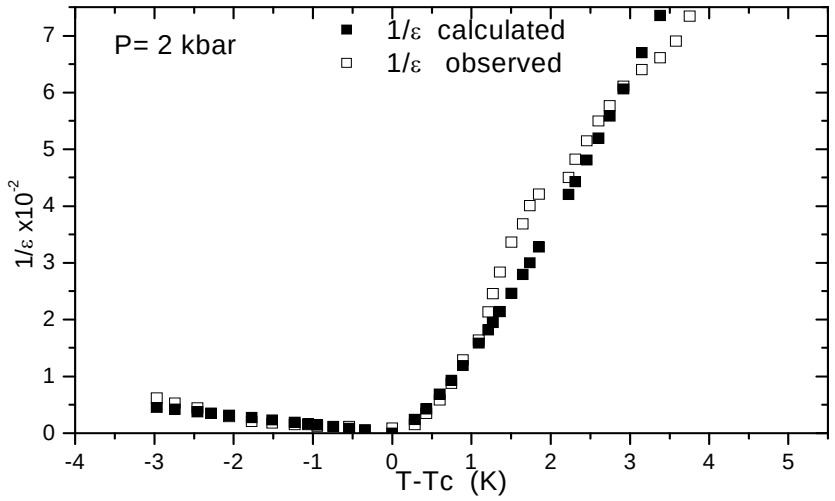

Figure 3.22 The inverse dielectric constant $1/\varepsilon$ obtained from the analysis of the observed data [29] according to Eq. (3.26) at P=2 kbar for TSCB close to the paraelectric-ferroelectric phase transition (T_c=47.2 K).

Finally, the similar analysis was carried out for the susceptibility χ at various temperatures for P=3 kbar close to the paraelectric-ferroelectric phase transition in TSCB. Using the power-law formula in the logarithmic form (Eq. 3.27), the experimental data was analyzed and the values of γ and B were deduced, as tabulated in Table 3.16.

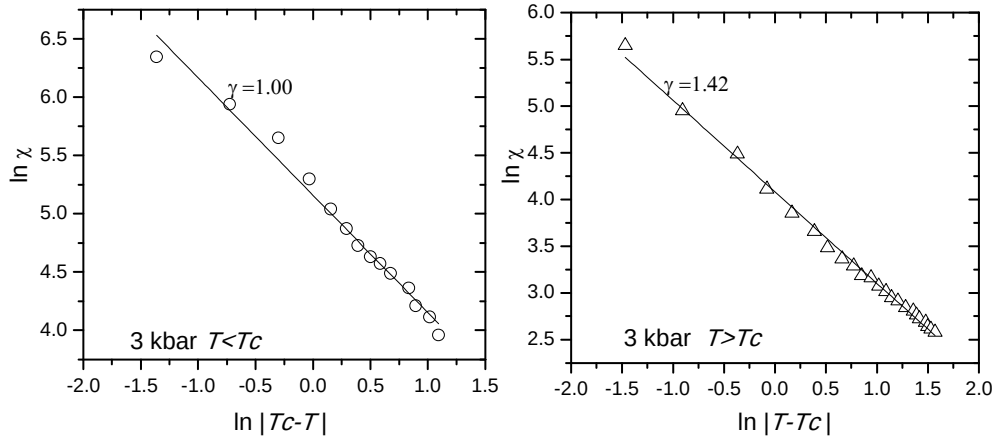

Figure 3.23 Log-log plots of the susceptibility χ against the temperature in the ferroelectric phase (T<T_c) and paraelectric phase (T>T_c) of TSCB at P=3 kbar (T_c=64.3 K) [29] according to Eq. (3.27).

Plots of lnχ against ln|T-T_c| below and above T_c are shown in Fig. 3.23. Fig. 3.24 gives calculated 1/ε at various temperatures (T-T_c) for P=3 kbar with the observed data [29] for TSCB.

From our plots 1/ε against (T-T_c) for P=1, 2 and 3 kbars, as given by Figs. 3.20, 3.22 and 3.24, respectively, we deduced the values of the Curie constant according to the relation

$$\varepsilon = C/(T - T_c) \tag{3.28}$$

in the paraelectric phase of TSCB. Our C values are 1.12, 2.49 and 1.49 K for 1, 2 and 3 kbars, respectively .

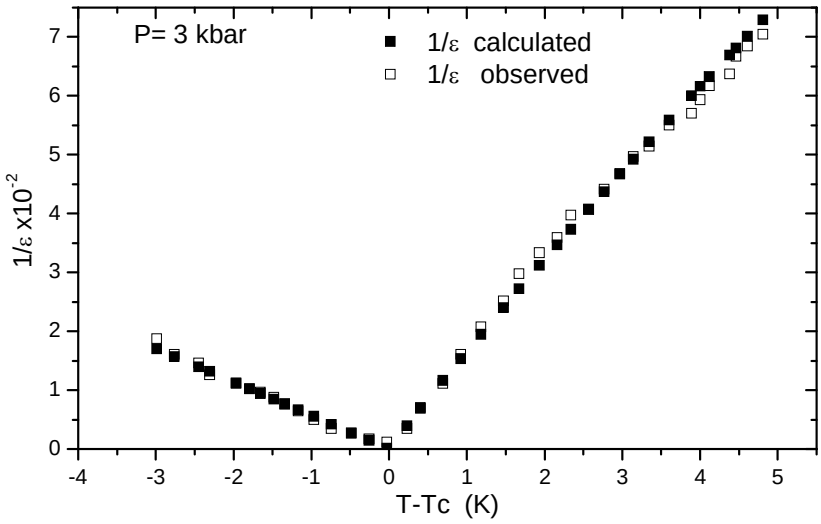

Figure 3.24 The inverse dielectric constant 1/ε obtained from the analysis of the observed data [29] according to Eq. (3.26) at P=3 kbar for TSCB close to the paraelectric-ferroelectric phase transition (T_c=64.3 K).

3.2.3 Pippard Relations for Carbon Tetrachloride near the Melting Point

It has been indicated that carbon tetrachloride undergoes a second order transformation with the premelting effects as shown by the thermal expansivity

α_p, isothermal compressibility κ_T and the specific heat C_p [55]. Divergence behaviour of those thermodynamic quantities, namely, α_p, κ_T and C_p has been described by a power-law formula near the melting point [55].

On the basis of similar critical behaviour of α_p, κ_T and C_p close to the melting point of CCl_4, the Pippard relations [3] can be established for this molecular system. By relating the specific heat C_p to the thermal expansivity α_p (first Pippard relation) and also α_p to the isothermal compressibility κ_T (second Pippard relation) close to the melting point in carbon tetrachloride, the Pippard relations can be examined in this system. From those linear variations of C_p vs. α_p and of α_p vs. κ_T , the rate of change of the melting pressure with the temperature (dp_m/dT) can be predicted for CCl_4 near its melting point.

In this study, by analyzing the experimental data for the thermal expansivity α_p at various pressures [55]. we calculate the pressure dependence of the isothermal compressibility κ_T and of the specific heat C_p in CCl_4 close to the melting point[88,89]. We then establish the Pippard relations and predict the values of the slope dp_m/dT for this molecular organic compound.

The pressure dependence of the thermal expansivity α_p in carbon tetrachloride can be expressed as a power-law formula given by

$$\alpha_p = A(p - p_m)^{-\gamma} \tag{3.29a}$$

or in the logarithmic form as

$$\ln \alpha_P = \ln A - \gamma \ln(p - p_m) \tag{3.29b}$$

where γ is the critical exponent for α_p and A is the amplitude. p_m denotes the melting pressure. Using the thermodynamic relation

$$\alpha_p / \kappa_T = (\partial p_m / \partial T)_V \tag{3.30}$$

the pressure dependence of the isothermal compressibility κ_T can be approximated to the relation

$$\kappa_T = A(dp_m / dT)^{-1}(p_m - p)^{-\gamma} \tag{3.31}$$

for CCl_4 near the melting point.

Also, the specific heat C_p can be calculated as a function of pressure near the melting point for carbon tetrachloride using the thermodynamic relation

$$C_p = TV(\alpha_p{}^2 / \kappa_T). \tag{3.32}$$

By means of Eqs. (3.29) and (3.31), the specific heat C_p can be obtained as

$$C_p = ATV(dp_m / dT)(p_m - p)^{-\gamma} \tag{3.33}$$

for CCl_4 close to the melting point.

By assuming that the specific heat C_p, thermal expansivity α_p and the isothermal compressibility κ_T have similar critical behaviour near the melting point in carbon tetrachloride, the Pippard relations can be established in this system. By relating C_p to α_p linearly,

$$C_p = VT(dp_m / dT)\,\alpha_p + T(dS / dT)_m\ , \tag{3.34}$$

where S is the entropy, and also by relating α_p to κ_T linearly,

$$\alpha_p = (dp_m / dT)\,\kappa_T + \frac{1}{V}(\frac{dV}{dT})_m \tag{3.35}$$

we established the first and second Pippard relations, respectively for CCl_4 system close to the melting point.

We analyzed here the pressure dependence of the thermal expansivity α_p for the liquid and solid phases in carbon tetrachloride using the experimental data [55], as given in Fig. 3.25 according to the power-law formula (Eq. 3.29).

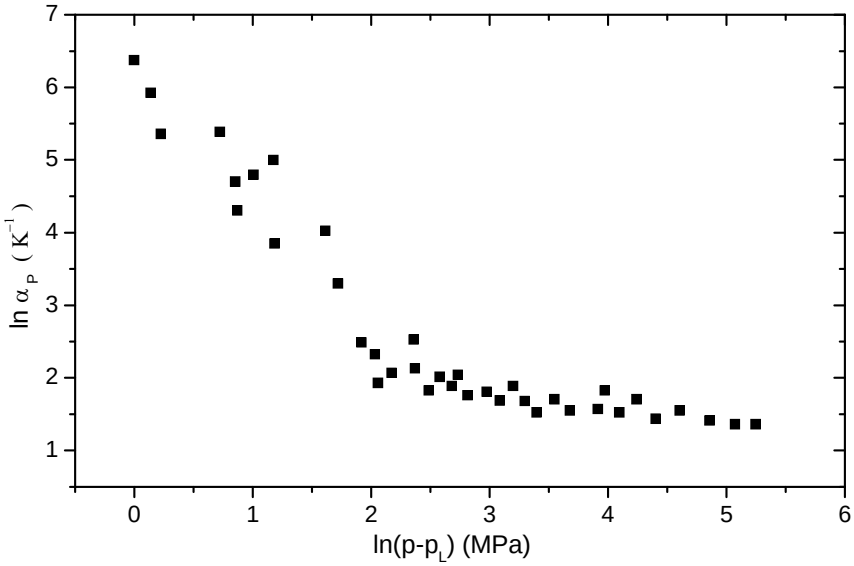

Figure 3.25 Experimental values of the thermal expansivity α_p as a function of pressure p along the isotherms 283, 301.5, 302 and 325 K in a log-log scale in carbon tetrachloride near the melting point [55]. p_L denotes the liquid pressure.

Values of the critical exponent γ and the amplitude A are tabulated in Table 3.17. Figs. 3.26 and 3.27 give our linear plots of $\ln\alpha_p$ against $\ln(p\text{-}p_L)$ for the liquid and solid phases, respectively, in CCl_4.

Table 3.17 Values of the critical exponent γ and the amplitude A for the liquid and solid phases of carbon tetrachloride near the melting point according to the power-law formula (Eq.1).

Phase	γ	A (MPa/K)
Liquid	1.74	515.9
Solid	0.21	11.51

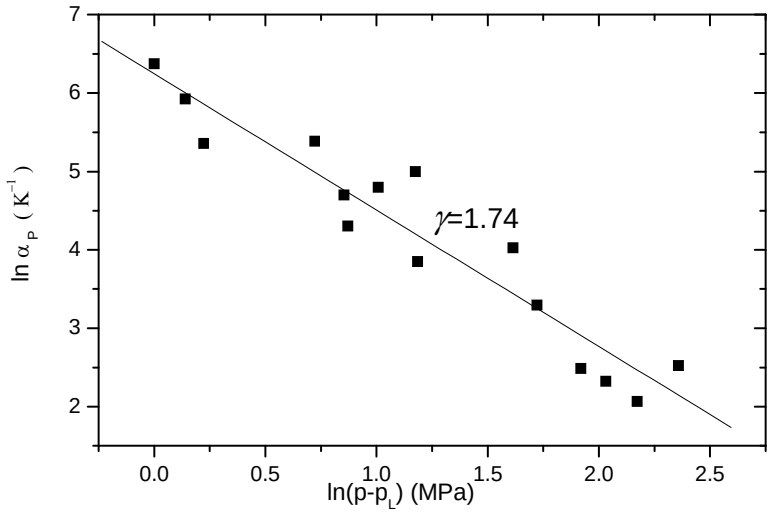

Figure 3.26 A log-log plot of α_p as a function of the pressure in the liquid phase of carbon tetrachloride (Fig. 3.25) according to Eq. (3.29).

Using the experimental data for the thermal expansivity α_p at various pressures [55], we then calculated the pressure dependence of the isothermal compressibility κ_T by means of Eq. (3.31) near the melting point in CCl_4. Also, the specific heat C_p was calculated at various pressures near the melting point in carbon tetrachloride using Eq. (3.33). Thus, we were able to establish the Pippard relations (Eqs. 3.34 and 3.35) near the melting point for CCl_4.

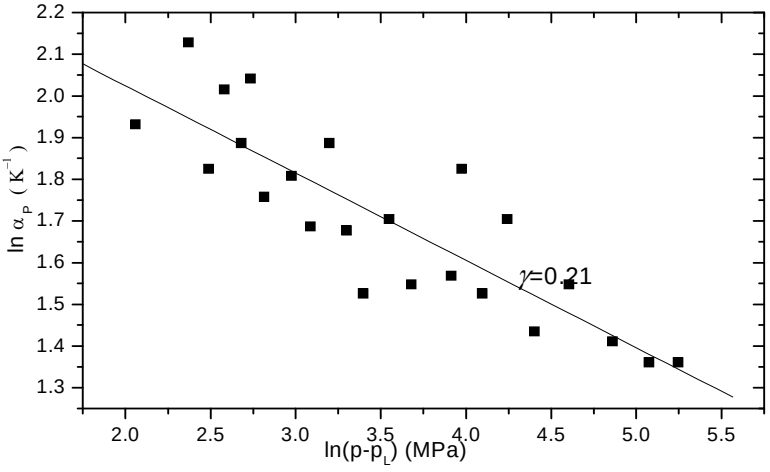

Figure 3.27 A log-log plot of α_p as a function of the pressure in the solid phase of carbon tetrachloride (Fig. 3.25) according to Eq. (3.29).

We first established a linear variation of the thermal expansivity α_p with the isothermal compressibility κ_T in the liquid phase and the solid phase of CCl_4, as given in Figs. 3.28 and 3.29, respectively, according to the second Pippard relation (Eq. 3.35).

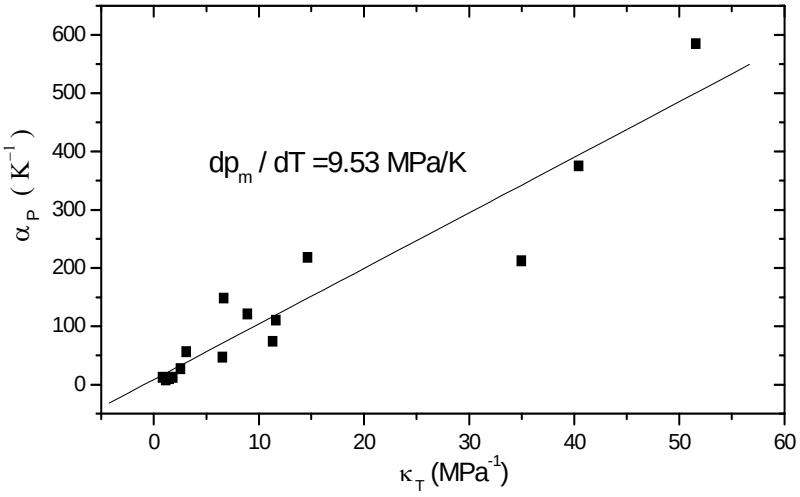

Figure 3.28 The thermal expansivity α_p as a function of the isothermal compressibility κ_T in the liquid phase of carbon tetrachloride according to the second Pippard relation (Eq. 3.35). dp_m/dT denotes the slope value.

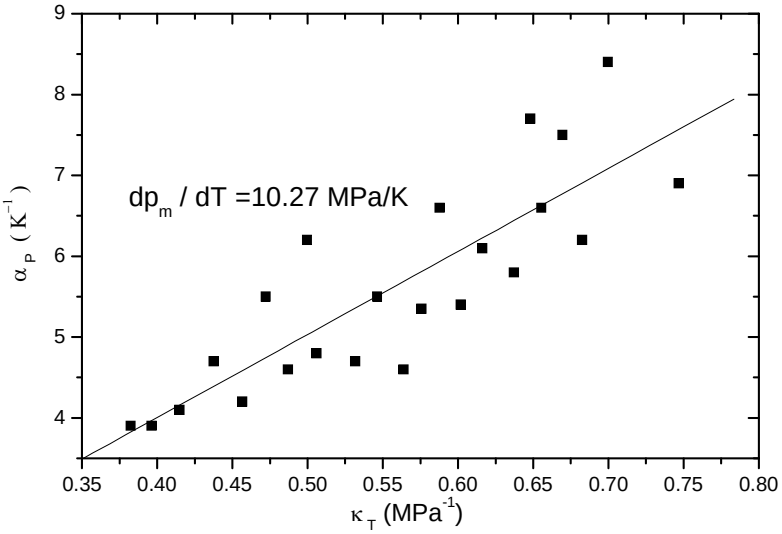

Figure 3.29 The thermal expansivity α_p as a function of the isothermal compressibility κ_T in the solid phase of carbon tetrachloride according to the second Pippard relation (Eq.3.35). dp_m/dT denotes the slope value.

From those linear plots, the values of the slope dp_m/dT and the $(dV/dT)_m$, which we deduced, are given in Table 3.18. To calculate $(dV/dT)_m$ from the intercept $\frac{1}{V}(\frac{dV}{dT})_m$, we used the value of V=96.52x10^{-6} m^3/mol for carbon tetrachloride [90].

Table 3.18 Values of the slope dp_m/dT and the intercepts $(dV/dT)_m$ (Eq. 3.35) and $(dS/dT)_m$ (Eq. 3.34) for the liquid and solid phases of carbon tetrachloride near the melting point (T_m=302 K).

Pippard Relations	α_p vs. κ_T (Eq. 3.35)		C_p/V vs. α_p (Eq. 3.34)	
Phase	dp_m/dT (MPa/K)	$(dV/dT)_m$x10^{-6} (m^3/mol.K)	dp_m/dT (MPa/K)	$(dS/dT)_m$ x10^3 (J/mol.K^2)
Liquid	9.53	819.45	8.36	5.342
Solid	10.27	-9.65	6.67	1.557

We also established linear plots of the C_p/V against α_p for the liquid and solid phases of carbon tetrachloride near the melting point, as plotted in Figs. 3.30 and 3.31, according to the first Pippard relation Eq. (3.34).

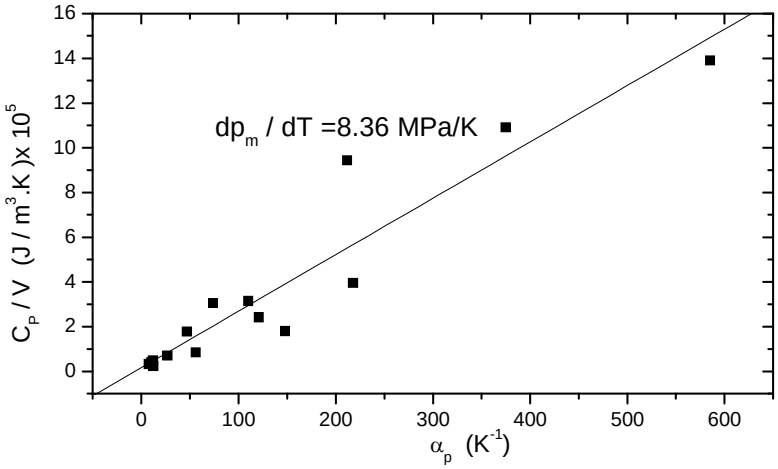

Figure 3.30 The specific heat C_p per unit molar volume V as a function of the thermal expansivity α_p in the liquid phase of carbon tetrachloride according to the first Pippard relation (Eq.3.34). dp_m/dT denotes the slope value at T=302 K.

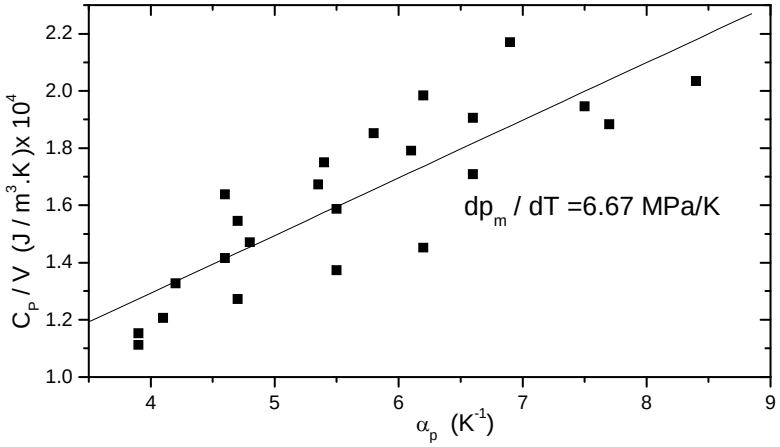

Figure 3.31 The specific heat C_p per unit molar volume V as a function of the thermal expansivity α_p in the solid phase of carbon tetrachloride according to the first Pippard relation (Eq.3.34). dp_m/dT denotes the slope value at T=302 K.

Similarly, our values of the slope dp_m/dT and the intercept $(dS/dT)_m$ for the liquid and solid phases of CCl_4, which were obtained from Eq.(3.34) are tabulated in Table 3.18. In order to obtain the slope and intercept values, we used the melting temperature of T_m=302 K in Eq. (3.34) for the liquid and solid phases of carbon tetrachloride.

3.2.4 Calculation of the Molar Volume in the Solid and Liquid Phases of CCl_4

As stated previously, in carbon tetrachloride the thermodynamic quantities such as the thermal expansivity α_P, isothermal compressibility κ_T and the specific heat C_P can exhibit critical behaviour near the melting point. The pressure dependence of the thermal expansivity α_P can be described by a power-law formula given in Eq. (3.29) with the critical exponent γ and the amplitude A close to the melting pressure p_m, as also represented previously [55]. By means of the thermodynamic relation between α_P and κ_T (Eq. 3.30) near the melting point in CCl_4, the pressure dependence of the isothermal compressibility κ_T can be

obtained as in Eq. (3.31). Along the melting line in carbon tetrachloride, one can approximate the slope as

$$(\partial p_m / \partial T)_V = \frac{p - p_m(T)}{T_m(P) - T} \tag{3.36}$$

where the melting pressure p_m and the melting temperature T_m are the functions of temperature and pressure, respectively. Thus, the temperature dependence of the thermal expansivity α_P can be derived using Eq. (3.36) in Eq. (3.29a), which gives

$$\alpha_P = A(\partial p_m / \partial T)_V^{-\gamma} (T_m - T)^{-\gamma} \tag{3.37}$$

By integrating the definition of the isothermal compressibility, $\kappa_T = -(1/V)(\partial V / \partial P)_T$, the pressure dependence of the volume can be obtained at a constant temperature as

$$V_T(P) = V_m \exp\left[\frac{1}{(\partial p_m / \partial T)_V} \frac{A(p - p_m)^{1-\gamma}}{1-\gamma} \right] \tag{3.38}$$

where V_m represents the melting volume. Similarly, the temperature dependence of the volume can be obtained at a constant pressure by integrating the definition of the thermal expansivity $\alpha_P = (1/V)(\partial V / \partial T)_P$, which gives

$$V_P(T) = V_m \exp\left[\frac{A(T - T_m)^{1-\gamma}}{(\partial p_m / \partial T)_V (1-\gamma)} \right] . \tag{3.39}$$

In order to analyze the experimental data for the pressure dependence of the thermal expansivity α_P in carbon tetrachloride [55], we used Eq. (3.29b).

We first analyzed the experimental data for the thermal expansivity α_P [55] at various pressures for a constant temperature (302 K) in the solid phase ($p<p_m$) of carbon tetrachloride according to Eq. (3.29b) with the values of the critical exponent γ and the amplitude A within the pressure range, as given in Table 3.19.

Table 3.19 The calculated values of the critical exponent γ and the amplitude A from the analysis of the thermal expansivity α_P for carbon tetrachloride at various pressures for a constant temperature of T=302 K [55] according to Eq. (3.29b) in the solid and liquid phases within the pressure and temperature ranges indicated near the melting point.

Phase		γ	A[(MPa)$^{\gamma}$/K]	Pressure range (MPa)	Temperature range (K)
Solid	$p<p_m$ $T>T_m$	0.21	11.51	$1< p-p_m <10.58$	$0.10<T_m-T<1.06$
Liquid	$p>p_m$ $T<T_m$	1.74	515.9	$7.84< p-p_m<190$	$0.78<T_m-T<19.0$

Using the values of γ and A, we then evaluated the molar volume of CCl_4 in the solid phase as a function of pressure with respect to the liquid pressure (p_L) for T=302 K according to Eq. (3.38) where the melting volume was taken as V_m=96.52×10^{-6}m^3/mol [90]. The experimental value of the slope, $(\partial p_m / \partial T)_V$ =10 MPa/K was used in Eq. (3.38) to calculate the molar volume at various pressures in the solid phase of CCl_4 [91]. We plot in Fig. 3.32 $V_T(P)$ against $(p - p_L)$ in the solid phase of CCl_4, where p_m(melting pressure)=p_L(liquid pressure).

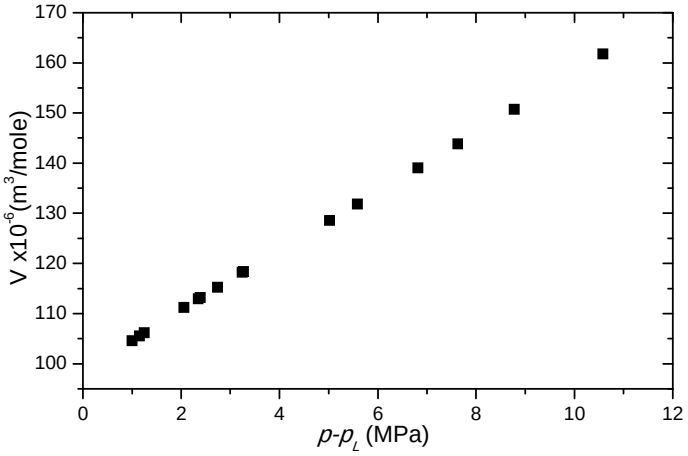

Figure 3.32 The molar volume as a function of pressure at T=302 K for the solid phase of CCl_4 close to the solid-liquid phase transition. p_L denotes the liquid pressure.

Similarly, the experimental data for the thermal expansivity α_P was analyzed for the liquid phase ($p>p_m$) of carbon tetrachloride at T=302 K according to Eq. (3.29b). The values of the critical exponent γ and the amplitude A from our analysis, within the pressure range, are given in Table 3.19. Using the values of γ and A (Table 3.19), $(\partial p_m / \partial T)_V$ and V_m, we evaluated the molar volume $V_T(P)$ as a function of $p - p_L$ for a constant temperature of 302 K in the liquid phase of CCl_4, which did not vary considerably with the pressure [91].

We also calculated the temperature dependence of the molar volume $V_P(T)$ at a constant pressure according to Eq. (3.39) in the solid and liquid phases of carbon tetrachloride near the melting point [91]. Using the values of γ and A within the temperature range in the solid and liquid phases (Table 3.19), we calculated $V_P(T)$ at various temperatures at a constant pressure for the solid phase of CCl_4, as plotted in Fig. 3.33. For the liquid phase, the molar volume did not vary considerably with the temperature, as it was obtained for the pressure dependence of the molar volume in the liquid phase of CCl_4.

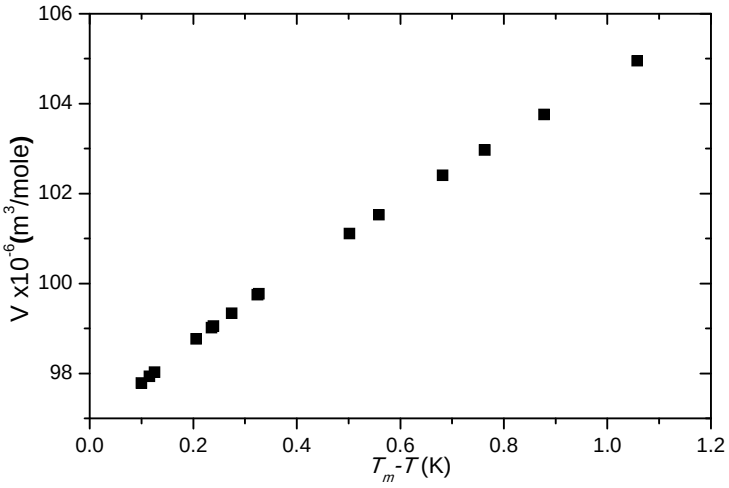

Figure 3.33 The molar volume as a function of temperature for the solid phase of CCl_4 close to the solid-liquid phase transition. T_m denotes the melting temperature.

3.2.5 Temperature Dependence of the Damping Constant close to the I-II Phase Transition in S-triazine

An Ising pseudospin-phonon coupled model due to Yamada et al. [92] considers interactions between phonon and the pseudospin, which has been employed for ammonium halides, in particular for NH_4Br. Matsushita [93] has extended this model by considering interactions between more than one phonon and pseudospins. By treating an Ising pseudospin-phonon coupled model with all these interactions, he was able to derive the temperature dependence of the damping constant for phonons in ammonium halides (NH_4Br and NH_4Cl). The damping constant derived by Matsushita [93] is given by

$$\Gamma(\vec{k}\nu,\omega)=\sum_{q\nu'}\frac{|K_1(\vec{k},\vec{q},\nu,\nu')|^2}{8\omega\omega_0(\vec{k}-\vec{q},\nu')}\times \left\{\left[\frac{n(\omega_0(\vec{k}-\vec{q},\nu'))}{n(\omega-\omega_0(\vec{k}-\vec{q},\nu'))+1}+1\right]S(\vec{q},\omega-\omega_0(\vec{k}-\vec{q},\nu'))\right. \left.+\left[\frac{n(\omega_0(\vec{k}-\vec{q},\nu'))+1}{n(\omega+\omega_0(\vec{k}-\vec{q},\nu'))+1}+1\right]S(\vec{q},\omega+\omega_0(\vec{k}-\vec{q},\nu'))\right\} \tag{3.40}$$

This expression describes the ν th phonon of the wave vector $\vec{k}$ interacting with the ν' th phonon of the wave vector $\vec{k}-\vec{q}$ and with a pseudospin $\sigma(\vec{q})$ of the wave vector $\vec{q}$. ω_0 is the characteristic frequency and the frequency dependence of n is defined as $n(\omega)=(e^{\hbar\omega/kT}-1)^{-1}$ where $\hbar$ is the Planck constant, and k is the Boltzmann's constant. $K_1(\vec{k},\vec{q},\nu,\nu')$ represents the effective coupling constant among the two phonons of $(\vec{k}\nu)$ and $(\vec{k}-\vec{q},\nu')$, and the pseudospin $\sigma(\vec{q})$. This coefficient is related to the force constant and the lattice constant [93]. In Eq. (3.40) $S(\vec{q},\omega)$ is the dynamic scattering function of the pseudospins. This is the Fourier transform of the correlation function of the pseudospin variables $\sigma(\vec{q})$, which is defined as

$$S(\vec{q},\omega) = \int dt\, e^{i\omega t} < \sigma(\vec{q},t)\, \sigma^{*}(\vec{q},0) > \tag{3.41}$$

A sudden change in the dynamic scattering function $S(\vec{q},\omega)$ near the critical temperature T_c is accompanied with a critical behaviour of the damping constant $\Gamma(\vec{k}\nu,\omega)$. Below T_c, $S(\vec{q},\omega)$ is of a Debye type and it increases strongly with temperature at low frequencies near T_c [94,95]. Thus, in Eq. (3.40) the dynamic scattering function will be dominant at the peak frequency $\omega = \omega_\nu$ with $\nu = \nu'$, which is written as

$$S(\vec{q},\, \omega_\nu(\vec{k}) - \omega_\nu(\vec{k} - \vec{q})) \cong S(\vec{q}, \omega = 0) \tag{3.42}$$

where

$$\omega_\nu = \omega_0(\vec{k},\nu) \cong \omega_0(\vec{k} - \vec{q},\nu') \tag{3.43}$$

Eq. (3.43) assumes a very weak dispersion of ω_ν. On the basis of the dominant dynamic scattering function $S(\vec{q},\omega_\nu)$ at $\omega = \omega_\nu$, the damping constant can be written as

$$\Gamma(\vec{k}\nu,\omega) \cong \Gamma(\vec{k}\nu,\omega_\nu) \tag{3.44}$$

which is of a Lorentzian type, as also indicated previously [94,95]. By assuming that K_1, ω's and n's in Eq. (3.40) depend upon the wave vector $\vec{q}$ and the temperature T weakly, and by replacing the summation on q by an integral [94,95], the damping constant $\Gamma(\vec{k}\nu,\omega)$ can be expressed as

$$\Gamma(\vec{k}\nu,\omega_\nu) \cong A \int_{BZ} S(\vec{q},\omega) \left[\frac{n(\omega)}{n(\omega)+1} + 1 \right] d^3\vec{q} + B \tag{3.45}$$

as obtained previously by Laulicht [94,95]. In Eq. (3.45) the integral is taken over all $\vec{q}$ in the Brillouin zone (BZ). A and B are constants. By denoting the damping constant due to pseudospin-phonon (sp) coupling

$$\Gamma(\vec{k}\nu,\omega_\nu) = \Gamma_{sp}(\omega_\nu) \tag{3.46}$$

Equation (3.45) can be written approximately

$$\Gamma_{sp}(\omega_v) \cong A \int_{BZ} S(\vec{q},0)\, dq \tag{3.47}$$

Using the calculations of Lahajnar et al. [96], a strong temperature dependence of the damping constant at the peak frequency ω_v near T_c can be obtained as

$$\Gamma_{sp}(\omega_v) = \Gamma_0 + A(1-P^2)\ln\left[\frac{T_c}{T - T_c(1-P^2)}\right] \tag{3.48}$$

which has been introduced by Laulicht [94,95] for ferroelectric KDP type crystals. In Eq. (3.48), $P=P_s / P_{max}$ is the fractional spontaneous polarization as an order parameter for ferroelectric crystals, which depends on the temperature. The P values vary from 0 to 1. $P=0$ describes the paraelectric (disordered) phase ($T>T_c$), whereas in the ferroelectric (ordered) phase $P\neq 0$ ($T<T_c$). In the damping constant expression Γ_{sp} at the peak frequency ω_v (Eq. 3.48), Γ_0 denotes the background damping constant which is independent of temperature and A is a constant.

Similarly, Schaack and Winterfeldt [97] have calculated using the pseudospin-phonon coupling, a strong temperature dependence of the damping constant near T_c, which is given by

$$\Gamma_{sp}(\omega_v) = \Gamma_0 + A\left[\frac{T(1-P^2)}{T - T_c(1-P^2)}\right]^{1/2} . \tag{3.49}$$

In this expression for the damping constant at the peak frequency ω_v, P is the fractional spontaneous polarization, as given in Eq. (3.48), which varies with the temperature. The temperature independent parameter Γ_0 represents the background damping constant and A is a constant, as before. Thus, both damping constants (Eqs. 3.48 and 3.49) exhibit anomalous behavior due to the pseudospin-phonon coupling at the peak frequency ω_v near T_c. A strong temperature dependence of the damping constant is also contributed by that dependence of the order parameter P below T_c.

The temperature dependence of the damping constant of the Raman mode II was calculated from the order parameter for the I-II phase transition in s-triazine

according to Eqs. (3.48) and (3.49). The temperature dependence of the order parameter (shear strain angle θ) was obtained from the experimental Raman frequencies of mode II using the relation

$$\omega_{II}{}^2 = \omega_0{}^2 - \alpha\theta + \beta_2\theta^2 \tag{3.50}$$

in an earlier study[98]. This is the Raman frequency of the mode II that is degenerate in phase I, which has been expanded in terms of the shear strain angle θ, as proposed by Rae [99]. This is originated from the potential energy of the crystal expressed as a series expansion of the normal mode coordinates of the Raman-active and soft-acoustic phonon modes [98]. In Eq. (3.50) ω_0 is the Raman frequency in the high-temperature phase (phase I), α and β_2 are constants. This equation was fitted to the experimental data for the Raman frequencies ω_{II} of the mode II and for the shear strain angle θ, and the coefficients ω_0, α and β_2 were determined [98], as given in Table 3.20.

Table 3.20 Values of the parameters obtained by fitting Eq. (3.50) to the experimental frequencies of the Raman mode II as a function of the shear strain angle θ (order parameter) in s-triazine. This data is taken from Ref. [90].

	Ref.[98]	Ref.[99]
$\omega_0{}^2$ (cm^{-2})	5314	5002
α (cm^{-2} rad^{-1})	3700	4664
β_2 (cm^{-2} rad^{-2})	101000	132200
Cross-over temperatures	178 >198	189 K 187 K

Thus, from the temperature dependence of the Raman frequencies of mode II, the order parameter was obtained as a function of temperature, as given in Fig. 3.34. The values of the order parameter were then used to determine the damping constant Γ according to the approximate relations, Eqs. (3.48) and (3.49) for the Raman mode II in s-triazine below the transition temperature (T_c=198 K) for the I-II phase transition [100]. In Eqs. (3.48) and (3.49), P denotes the order parameter (shear strain angle θ). Since the order parameter is zero above T_c, the damping

constant was obtained in the simpler form in the case of P=0 or θ= 0 in Eqs. (3.48) and (3.49). We plot the observed values of the damping constant Γ for the Raman mode II [98] as a function of $(1-P^2)\ln[T_c/(T-T_c(1-P^2))]$ according to Eq. (3.48) below T_c in Fig. 3.35 [100]. The observed Γ values are plotted as a function of $\ln[T_c/(T-T_c(1-P^2))]$ above T_c in the case of P=0 or θ=0 in Fig. 3.36, according to Eq. (3.48) [100]. The parameters for a linear fit are given within the temperature interval in Table 3.21.

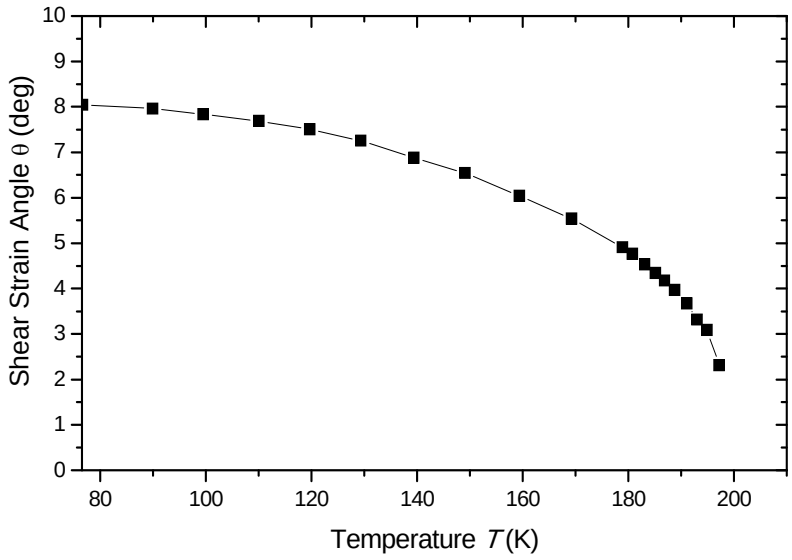

Figure 3.34 Shear strain angle θ (order parameter) obtained from the observed frequencies of the Raman mode II according to Eq. (3.50) [98] as a function of temperature for the I-II phase transition in s-triazine.

Table 3.21 Values of the fitted parameters Γ_0 and A below and above T_c for the temperature intervals given according to Eq. (3.48) for the I-II phase transition ($T_c \approx 200$ K) in s-triazine.

T_c=200 K	Γ_0 (cm^{-1})	-A (cm^{-1})	Temperature Interval (K)
$T< T_c$	4.7710	0.0117	$76.757 \leq T \leq 199.91$
$T> T_c$	7.4483	1.1442	$208.94 \leq T \leq 289.14$

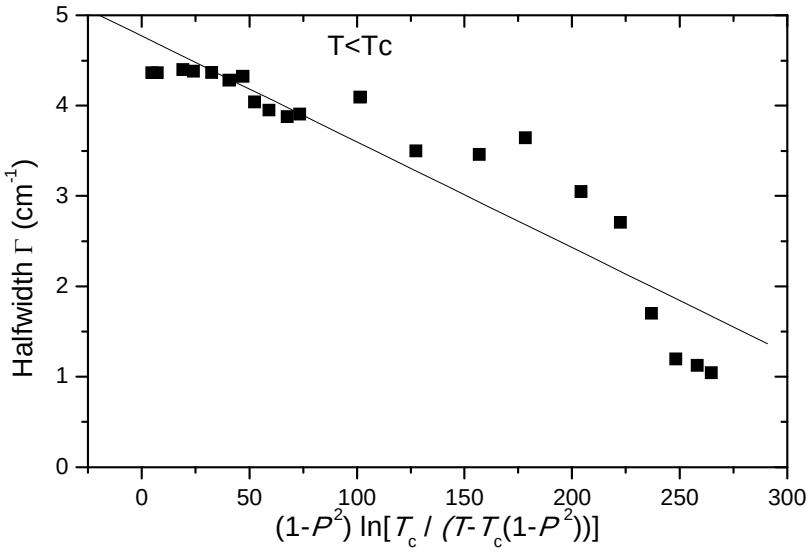

Figure 3.35 Observed halfwidths [98] of the Raman mode II, plotted as a function of $(1-P^2)\ln[T_c/(T-T_c(1-P^2))]$ below T_c according to Eq. (3.48) for the temperature interval (Table 3.21) for the I-II phase transition in s-triazine.

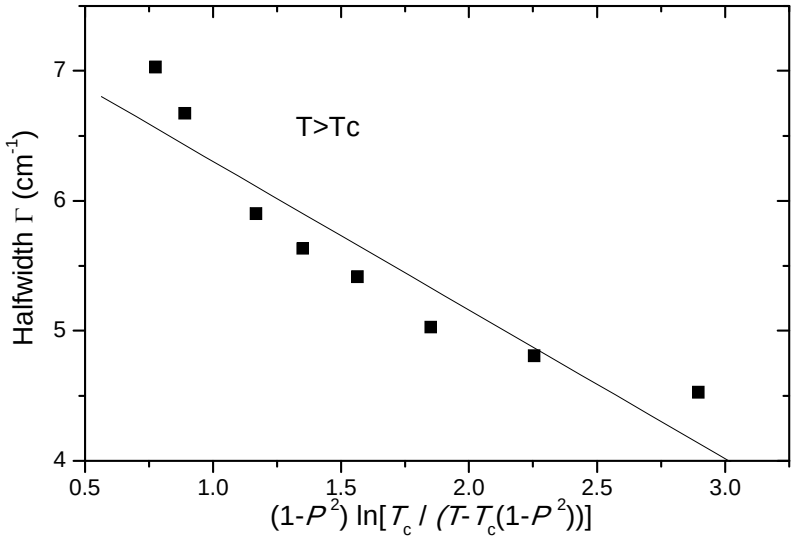

Figure 3.36 Observed halfwidths [98] of the Raman mode II, plotted as a function of $(1-P^2)\ln[T_c/(T-T_c(1-P^2))]$ above T_c (P=0) according to equation (3.48) for the temperature interval (Table 3.21) for the I-II phase transition in s-triazine.

From the linear fit (Fig. 3.35 and Fig. 3.36), the values of the parameters within the temperature range are tabulated in Table 3.21.

Thus, using Eq. (3.48) we were able to calculate the damping constant Γ for the Raman mode II as a function of temperature within the temperature region (Table 3.21) below and above T_c by combining our calculated Γ values below T_c (Fig. 3.35) and above T_c (Fig. 3.36). Fig. 3.37 gives our calculated damping constant Γ with the observed halfwidths of the Raman mode II for the I-II phase transition in s-triazine.

We also calculated the damping constant of the Raman mode II as a function of temperature using the approximate relation given by Eq. (3.49) [100].

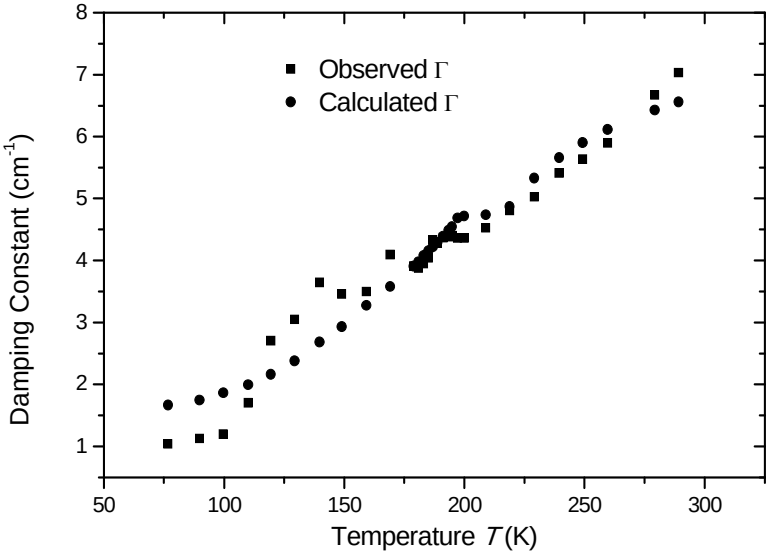

Figure 3.37 Our calculated damping constant Γ of the Raman mode II as a function of temperature for the I-II phase transition ($T_c \approx 198$ K) according to Eq. (3.48) in s-triazine. Observed halfwidths [98] of this Raman band are also plotted here.

Using the values of the order parameter P (shear strain angle θ) obtained from the Raman frequencies in Eq. (3.50), the damping constant Γ of the Raman mode II was calculated below and above T_c for the I-II phase transition in s-triazine. Fig. 3.38 gives our plot of the experimental Γ (halfwidth) as a function of $[T(1-P^2)/(T-T_c(1-P^2))]^{1/2}$ below the transition temperature (T_c=198 K).

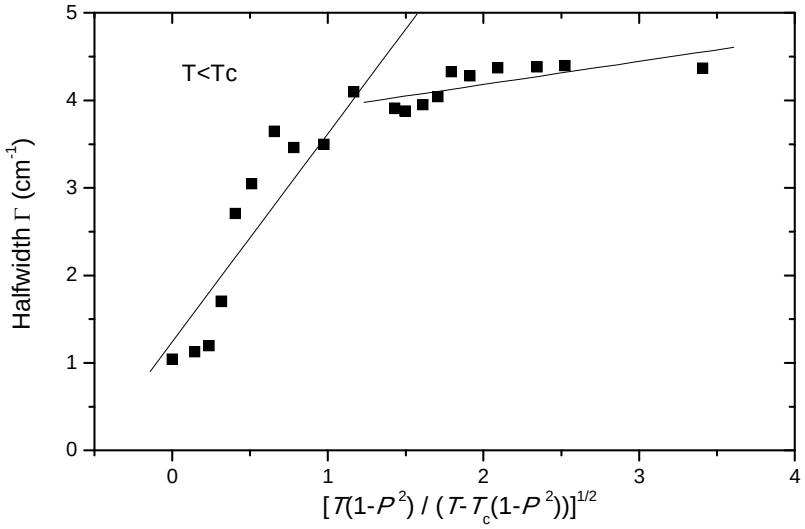

Figure 3.38 Observed halfwidths [98] of the Raman mode II, plotted as a function of $[T(1-P^2)/(T-T_c(1-P^2))]^{1/2}$ below T_c according to Eq. (3.49) for the temperature intervals (Table 3.22) for the I-II phase transition in ($T_c \approx 198$ K) s-triazine.

We established linear fits according to Eq. (3.49) within the two temperature regions below T_c by obtaining the values of the parameters Γ_0 and A, as tabulated in Table 3.22.

Table 3.22 Values of the fitted parameters Γ_0 and A below and above T_c for the temperature intervals given according to Eq. (3.49) for the I-II phase transition ($T_c \approx 200$ K) in s-triazine.

T_c=198 K	Γ_0 (cm^{-1})	A (cm^{-1})	Temperature Interval (K)
$T< T_c$	1.2397	2.3814	$76.757 \leq T \leq 178.96$
$T< T_c$	3.6520	0.2647	$178.96 \leq T \leq 197.24$
$T> T_c$	5.0465	-0.0713	$199.91 \leq T \leq 229.09$
$T> T_c$	11.5107	-2.6136	$239.42 \leq T \leq 289.14$

When we calculated the damping constant Γ as a function of $[T/(T-T_c)]^{1/2}$ according to Eq. (3.49) where P=0 or θ=0 above T_c, we also obtained linear fits within the two temperature regions, as shown in Fig. 3.39. In this figure the observed Γ (halfwidths) of the Raman mode II is plotted and the fitted parameters Γ_0 and A are given in Table 3.22 for the two temperature intervals above T_c in s-triazine. By combining our calculated Γ values below T_c (Fig. 3.38) and above T_c

(Fig. 3.39), we plot in Fig. 3.40 the damping constant Γ as a function of temperature (T_c=198 K) with the observed halfwidths of the Raman mode II.

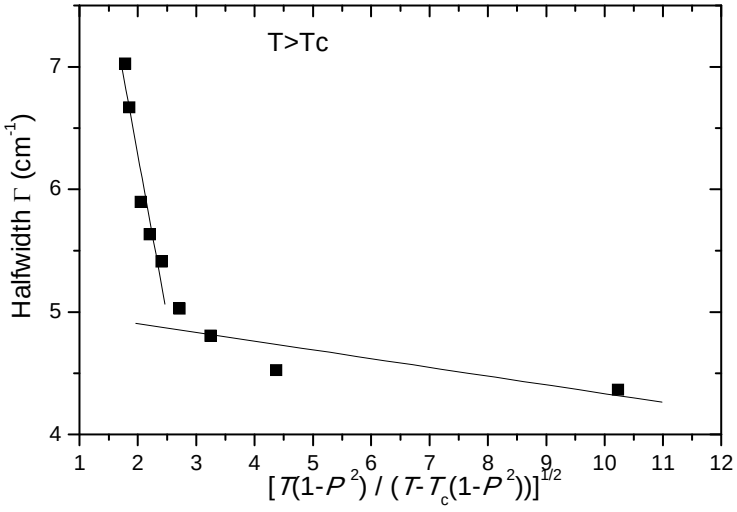

Figure 3.39 Observed halfwidths [98] of the Raman mode II, plotted as a function of $[T(1-P^2)/(T-T_c(1-P^2))]^{1/2}$ above T_c (P=0) according to Eq. (3.49) for the temperature intervals (Table 3.22) for the I-II phase transition in ($T_c \approx 198$ K) s-triazine.

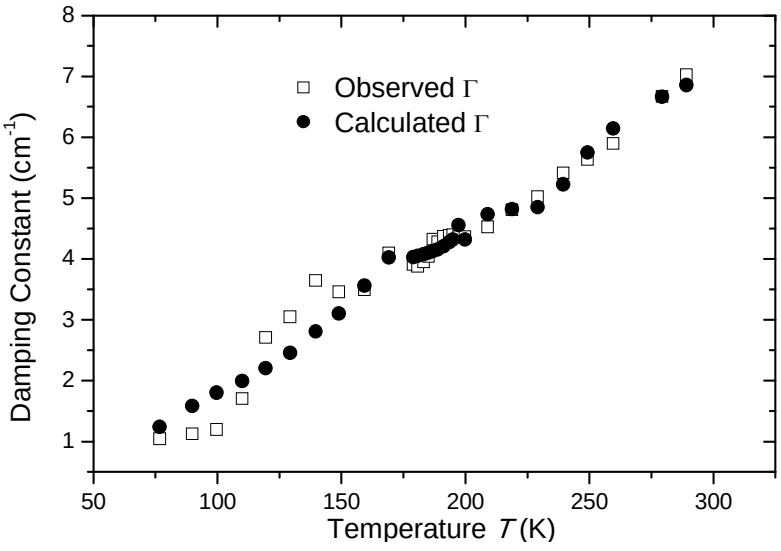

Figure 3.40 Our calculated damping constant Γ of the Raman mode II as a function of temperature for the I-II phase transition ($T_c \approx 198$ K) according to Eq. (3.49) in s-triazine. Observed halfwidths [98] of this Raman band are also plotted here.

CHAPTER 4

DISCUSSION

We calculated first the Raman frequencies of the v_5 TO (174 cm^{-1}) and v_2 (1708 cm^{-1}) modes as a function of temperature for the tricritical (1.6 kbar) and the second order (2.8 kbar) phase transitions in NH_4Cl. For this calculation we used the length-change data at 1 bar in this crystal [19]. From the initial length-change data at 1 bar and 260 K, we deduced the coefficients of the pressure dependent term of the vibrational frequency. Then we predicted the Raman frequencies for higher pressures of 1.6 kbar and 2.8 kbar for the v_5 and v_2 modes below ($T<T_c$) and above ($T>T_c$) the transition temperature T_c, which essentially increase as the pressure increases. The calculated Raman frequencies given in Figs. (3.1-3.4) are in good agreement with the observed data [78] for the phase transitions studied here. This shows that the Raman frequencies of those modes which are associated with the mechanism of phase transitions (tricritical and second order transitions) in NH_4Cl, can be predicted at higher pressures (1636 and 2841 bars) by using the length-change data at 1 bar. We shifted our calculated frequencies with respect to the observed frequencies because of the differences in the critical temperature values of the length-change data [19] and the observed Raman frequencies [77,78] at the pressures of 1, 1636 and 2841 bars (Table 3.1). The temperature shifts were ~3 K for 1636 kbar (Figs. 3.1 and 3.3) and ~2 K for 2841 bar (Figs. 3.2 and 3.4) to obtain the same T_c values for the observed frequencies. Also the order-disorder contribution terms were calculated from Figs. 3.1-3.4. The jumps in the critical frequency values for 1636 kbar were $\Delta v_c \approx 2.3$ cm^{-1} (Fig. 3.1) and ~1 cm^{-1} (Fig. 3.3) for the v_5 TO (174 cm^{-1}) and v_2 (1708 cm^{-1})

Raman modes, respectively. The $\Delta\nu_c$ values were about 2.1 cm^{-1} (Fig. 3.2) and ~0.5 cm^{-1} (Fig. 3.4) for the ν_5 TO (174 cm^{-1}) and ν_2 (1708 cm^{-1}), respectively in the region of the second order phase transition (P=2841 bar) of NH_4Cl. For the tricritical phase transition (P=1636 bar) region there is a discontinuous frequency jump for both Raman modes (Figs. 3.1 and 3.3) but this discontinuity does not occur in the second order transition (Figs. 3.2 and 3.4).

In NH_4Cl, we also calculated the specific heat from the Raman frequency shifts close to the tricritical and second order phase transitions. Using the observed Raman frequencies of the ν_5 (174 cm^{-1}) mode in NH_4Cl for the pressures of 1.6 kbar (Fig. 3.5) and 2.8 kbar (Fig. 3.6), we calculated the specific heat C_{VI} through Eq. 3.10 by using the critical exponent value of a=0.11 which was determined in a previous study [81]. Our calculated C_{VI} values at 1.6 kbar (Fig. 3.5) and 2.8 kbar (Fig. 3.6) are compared with the observed C_P data [82] at 1.5 kbar and 3134 bar. Since there are differences in the pressure values, some discrepancies occur in the Raman frequencies. For example, the critical temperature differs by 1-1.5 K between the observed C_P at P=1.5 kbar and calculated C_{VI} values at P=1.6 kbar. This shift in the transition temperature may be due to the 0.1 kbar difference in the pressure values. Also, this shift becomes higher in the second order transition region (P=2.8 kbar) when compared with the observed C_P data. It is about 1.4 K and this shift again can be due to different pressures at which the C_P data was used.

The next calculation was for the Raman frequencies of the ν_5 (125 cm^{-1}) and ν_7 (39 cm^{-1}) modes as a function of temperature (230 K< T < 270 K) for constant pressures of 706, 1080 and 6355 bars in the disordered phase II of NH_4I. We used the measured Raman frequencies [28] of the ν_5 (125 cm^{-1}) and ν_7 (39 cm^{-1}) modes at fixed pressures of 706, 1080 and 6355 as the initial data (Table 3.7). We determined the coefficients a_0, a_1 and a_2 in this pressure range (Table

3.6). We calculated the temperature dependence of the Raman frequencies of the two modes at constant pressures considered and plotted in Figs. 3.7 and 3.8. Our plots (Figs. 3.7 and 3.8), show that the Raman frequencies decrease as the temperature increases. The slope of our plots gives the value of $d\nu/dT = -0.06$ cm^{-1}/K for the ν_5 (125 cm^{-1}) and $d\nu/dT=-0.03$ cm^{-1}/K for the ν_7 (39 cm^{-1}) mode (Table 3.7) which was deduced from v vs. T (Eq. 3.19) for the fixed pressures of 706, 1080 and 6355 bars in NH_4I. Using the observed values for the temperature dependence of the lattice parameter at zero pressure, we calculated the temperature dependence of the Raman frequencies at higher pressures by Eq. (3.16). We treated $A(P)$ as the temperature independent and obtained the same slope values for the three different pressures for each mode. The discrepancy between the observed and calculated Raman frequencies may be due to a constant value of γ_P=2.4 and the ν_1 value observed at 1080 bar [28], which were both used for the pressures of 706 and 6355 bars in the phase II of NH_4I. Also, the volume (or lattice parameter) data obtained at zero pressure for the disordered phase II of NH_4I [84], was used with a constant V_1 value (Table 3.6) in Eq.(3.16) to calculate the Raman frequencies at higher pressures. This may cause some discrepancies between the calculated frequencies and the frequencies measured as a function of temperature for constant pressures of 706, 1080 and 6355 bars in the disordered phase II of NH_4I. When compared with the observed frequency data of those modes, our method of calculating the Raman frequencies at higher pressures from the volume data at zero pressure seems to be generally applicable. The high pressure measurements for the temperature dependences of the Raman frequencies of those two modes can be performed experimentally. A general applicability of the calculation method used in this work, can initiate the measurements of the Raman frequencies as a function of temperature at high pressures. Spectroscopically, the Raman frequencies can be measured to high accuracy compared to the volume measurements or the measurements of the thermal expansion α_P and of the isothermal compressibility κ_T thermodynamically, which are less accurate and also not easily accessible at high pressures. Thus, our calculation method gives an advantage that the Raman frequencies can be

predicted at high pressures by using precise measurements of volume at various temperatures at zero pressure. The predicted Raman frequencies can then be compared when the experimental data is available in the literature.

In NH_4I, we also calculated the temperature dependence of the Raman frequencies of the overtone $2\nu_6$ mode in phase III (tetragonal) at atmospheric pressure. We used the observed infrared frequencies [25] of $2\nu_6$ (I) to predict the crystal volume at various temperatures according to Eq. (3.21). Using the values of the crystal volume which we calculated, the Raman frequencies of $2\nu_6$ were predicted according to Eq. (3.20). In the interval $5K<T<210K$ there is a continuous change in the infrared measurements of the $2\nu_6$ (I) frequencies at around 110 K (P=0) [25]. The overtone of this mode which is $2\nu_6$ (II) exhibits anomalous behaviour. The same discontinuity has been observed for the Raman frequencies at around 110 K (P=0) [25], which we predicted using the calculated values of the crystal volume according to Eq. (3.20). This indicates that there is a new phase transition around 110 K at zero temperature. Within the temperature interval we studied (in phase III), the ordering type of the NH_4^+ ions can change below 110 K which has tetragonal antiparallel-order CsCl-type in NH_4I. Due to changes in the ordering of the NH_4^+ ions, the Raman frequencies of the $2\nu_6$ mode shift to higher frequencies at around 110 K in NH_4I, as shown in Fig. 3.10. Thus, the frequency shifts of this librational mode due to the torsional motions of NH_4^+ ions are accompanied with the change of order in NH_4I. The orientations of the NH_4^+ ions, as studied in ammonium halides previously [27,101-103], give rise to the orientational degree of order which then affect the surrounding halide ions and therefore the rotation barriers [25]. So, the torsional motions of NH_4^+ ions contribute to the transition of the different phases. We assumed that the order-disorder contribution Δ_P to $2\nu_6$, as the temperature-dependent (Eq. 3.22) in the prediction of the crystal volume (Eq. 3.21) and the Raman frequencies of $2\nu_6$ (Eq. 3.20). We used the observed values of the crystal volume and the Raman frequencies (Table 3.12) at three temperatures (P=0) as the initial data to

determine the temperature dependence of Δ_P. We used the value of γ_P=0.22 as the isobaric mode Grüneisen parameter for our calculation of the $2\nu_6$ Raman mode in the temperature range 70K<T<175K (Fig. 3.10) at zero pressure in NH_4I. The value of γ_P=0.22±0.04 has been given at 100 K and 35 kbar for the $2\nu_6$ (I) and $2\nu_6$ (II) Raman modes located at 603 cm^{-1} and 624 cm^{-1}, respectively [24]. The use of a constant mode Grüneisen parameter gives a good agreement between our calculated and the observed Raman frequencies of the overtone $2\nu_6$ in NH_4I.

We analyzed in this work the temperature dependence of the spontaneous polarization and the susceptibility for tris-sarcosine calcium chloride (TSCC) using the experimental data [29] at the pressures of 0, 1 and 2.2 kbars. We obtained that the values of the critical exponent β for the spontaneous polarization (order parameter) vary from 0.32 to 0.26, as the pressure increases (Table 3.13). Our value of β=0.32 at 0.001 kbar is close to the value of 0.3125 (=5/16) predicted by a three-dimensional Ising model. This indicates that TSCC undergoes a second order phase transition, which has been reported previously [32]. As the pressure increases to 1 and 2.2 kbars, the β value lowers to 0.28 and 0.26, respectively. The decrease in β value with the increasing pressure also indicates that the ferroelectric phase transition in TSCC changes its character from the second order towards a first order. This can be seen from our plots of the spontaneous polarization against the temperature (Fig. 3.1). The sharp discontinuity occurs at about $0.03\text{x}10^{-6}$ C/cm^2 (T_c=129.57 K) at 1 bar in spontaneous polarization, whereas for 1 kbar and 2 kbar discontinuous jump takes place at the values of nearly $0.04\text{x}10^{-6}$ C/cm^2 (T_c=142.17 K) and $0.05\text{x}10^{-6}$ C/cm^2 (T_c=154.54 K). Thus, the discontinuous jump increases as the pressure increases. This is an indication that a second order phase transition (1 bar) changes toward a first order (1 and 2.2 kbars) transition in the ferroelectric TSCC. We also analyzed the critical behavior of the susceptibility with the exponent values that varied from γ=1 to 1.2 (Table 3.14). Our values obtained here for the ferroelectric and paraelectric phases of TSCC, are close to the mean field value (γ =1) and the 3d Ising value (γ=1.25).

Finally, regarding our plots for the reciprocal dielectric constant 1/ε against temperature T-T_c (Figs. 3.14-3.16), we conclude that the slopes in both paraelectric ($T>T_c$) and ferroelectric ($T<T_c$) phases, decrease as the pressure increases.

We performed a similar analysis for tris-sarcosine calcium bromide (TSCB) for the temperature dependence of the spontaneous polarization and of the dielectric constant close to the ferroelectric phase transition at the pressures of 1, 2 and 3 kbars. We found the critical exponent value of β=0.35 for the spontaneous polarization at P=2 kbar in the ferroelectric phase of TSCB. Our β value is very close to the value of 0.3125 (5/16) predicted from a three-dimensional Ising model. Also, the critical exponent value of $\gamma\approx1$ for the susceptibility, which we deduced from our analysis at the pressures of 1, 2 and 3 kbars in the ferroelectric ($T<T_c$) and paraelectric ($T>T_c$) phases of TSCB is close to the value predicted from a three dimensional Ising model (γ=1.25). However, our values of γ=0.77 ($T>T_c$) at 1 kbar and γ=1.42 ($T>T_c$) at 2 kbar are not in agreement with the value of γ=1 as predicted from the mean field theory. Those γ values obtained, refer to the paraelectric phase ($T>T_c$) of TSCB. As given in Table 3.16, the transition temperature T_c shifts as the pressure increases for the ferroelectric materials studied here, but the critical exponent γ for the susceptibility does not change significantly, and it remains almost constant (γ=1). Also, we calculated the temperature dependence of the inverse dielectric constant (1/ε) and our values agree with the experimental data [29] (Figs. 3.20 and 3.22). When we compare the Curie constants (Table 3.16) which we obtained from our plots of 1/ε against T-T_c in the paraelectric phase of TSCB, the Curie constant for P=2kbar (Fig. 3.22) is greater than those obtained for P=1 kbar (Fig. 3.20) and P=3 kbar (Fig. 3.24).

Another study given in this thesis is the Pippard relations for carbon tetrachloride (CCl_4) near the melting point. We obtained in this study the values of the critical exponent γ and the amplitude A. Then we calculated the pressure dependence of the isothermal compressibility κ_T (Eq. 3.31) and the specific heat

C_p (Eq. 3.33). We used the slope value of dp_m/dT =10MPa/K as proposed by Pruzan et al. [55] to calculate the pressure dependence of the isothermal compressibility κ_T for carbon tetrachloride. By plotting α_p against κ_T according to Eq. 3.35 we then obtained the slope dp_m/dT values of 9.53 MPa/K for the liquid phase (Fig. 3.28) and 10.27 MPa/K for the solid phase of CCl_4 (Fig. 3.29). We used those slope values to calculate the pressure dependence of the specific heat C_p using Eq.(3.33). By means of the first Pippard relation (Eq. 3.34), we plotted C_p/V against α_p from which we obtained the slope values of dp_m/dT =8.36 MPa/K (Fig. 3.30) and 6.67 MPa/K (Fig. 3.31) for the liquid and solid phases of carbon tetrachloride, respectively. Our slope value obtained from a linear plot of C_p/V vs. α_p for the liquid phase is close to the expected value of 10 MPa/K.

In order to investigate the other thermodynamic properties of carbon tetrachloride near the melting point, we calculated the pressure dependence and temperature dependence of the molar volume by analyzing the experimental data for the thermal expansivity α_P for this crystal. From our analysis, we deduced the value of γ=0.21 in the solid phase of CCl_4, which is close to the value of 0.15, as obtained by Pruzan et al. [55] from their analysis. Also, the value of γ =1.74 which we deduced for the liquid phase of CCl_4, is close to the value γ_m=1.8 obtained by Pruzan et al. [55]. Our exponent value of γ=0.21 for the solid phase of CCl_4 is small in comparison with the value of 0.5 expected from the theoretical models [104,105]. The same value of 0.5 is also expected from the quasi harmonic theory applied to alkali halides when the experimental data has been analyzed for NaCl [106,107]. Our exponent value of γ=1.74 for the liquid phase of CCl_4 agrees with the exponent value greater than 1 which describes the critical behavior of the thermal expansivity according to the surface melting model [108,109]. We calculated the temperature and pressure dependences of molar volume using these calculated values of the critical exponent γ and the amplitude A. It increases as the pressure increases in the solid phase of CCl_4, as plotted in Fig. 3.32. The molar volume also increases as the temperature increases in the premelting region of

carbon tetrachloride, as shown in Fig. 3.33. In the liquid phase of CCl_4 , the molar volume does not vary considerably with the increase of temperature or pressure.

Finally, we calculated the damping constant Γ of the Raman mode II as a function of temperature on the basis of the soft mode-hard mode coupling model in s-triazine. We used the shear strain angle data (Fig. 3.34) as the order parameter (in Eq. 3.48 and 3.49) which were extracted previously [98] by means of Eq. 3.50. It has been indicated that the behavior of the shear strain angle (order parameter) near T_c is of weakly first order or nearly second order [59,98]. This critical behavior accompanied with a small latent heat discontinuity from the specific heat measurements, has been identified with the quasi-continuous structural phase transition [110]. This transition between phases I and II is driven by a soft acoustic phonon at the center of the Brillouin zone in the high temperature phase (phase I), as stated earlier [98]. Because of the scattered observed halfwidths [98], Eq. (3.48) does not represent the observed behavior adequately, as shown in Figs. 3.35 and 3.36. When we plotted the temperature dependence of the halfwidths calculated (Eq. 3.49) in two temperature intervals as shown in Figs. 3.38 and 3.39, it was obtained that the observed halfwidths were described well by Eq. (3.49) in s-triazine.

CHAPTER 5

CONCLUSION

We calculated the Raman frequencies of the v_5 and v_2 modes at various temperatures for the tricritical (1.6 kbar) and second order (2.8 kbar) phase transitions using the length-change data at 1 bar in NH_4Cl. Our calculated frequencies of the Raman modes studied, are in good agreement with the observed frequency data for the tricritical and second order regions. This supports the method given here to calculate the Raman frequencies at higher pressures from the length-change data obtained at zero pressure. This is useful in the sense that the volume (length-change) measurements are not easily accessible thermodynamically at higher pressures. Using the length-change measurements at atmospheric pressure, the Raman frequencies of those modes which are responsible for the mechanism of phase transitions can be predicted at higher pressures by means of the method given here. These predicted frequencies can then be compared with the frequencies measured spectroscopically at high pressures to high accuracy. Also, the critical behaviour of the specific heat C_{VI} in an Ising model was studied here by means of our frequency shifts for the ν_5 (174 cm^{-1}) Raman mode close to the tricritical and second order phase transitions in NH_4Cl. The specific heat C_{VI} was calculated as a function of temperature using the values of the critical exponent which were deduced from the Raman frequency data for P=1.6 kbar (tricritical) and P=2.8 kbar (second order) in NH_4Cl. Our calculated C_{VI} values are also in good agreement with the observed C_P data for both tricritical and second order phase transitions in NH_4Cl. Our values of the critical exponent $a = 0.11$ ($T<T_c$ and $T>T_c$) at 1.6 kbar and $a = 0.18$ ($T<T_c$) at

2.8kbar, which we deduced from the Raman frequency shifts of the ν_5 (174 cm^{-1}) mode in NH_4Cl, are close to the Ising value of 0.125 for the specific heat C_P.

The Raman frequencies of the ν_5 (125 cm^{-1}) mode were calculated as a function of temperature for constant pressures in the disordered phase II of NH_4I using the volume data at zero pressure. Our calculated frequencies can be compared with the experimentally measured frequencies at various temperatures under the given pressure conditions. This approach given here can be applied to the other phases of NH_4I and also close to the phase transitions between various phases, in particular, between the phases II and III in this crystal. Related to the Raman modes which appear in various phases of NH_4I, the temperature dependence of the Raman frequencies of the $2\nu_6$ mode was calculated in the tetragonal phase III of NH_4I. The Raman frequencies calculated for the overtone $2\nu_6$ exhibit anomalous behaviour at around 110 K (P=0), as observed experimentally. This transition is a precursor to the λ-phase transition within the phase III (tetragonal) in NH_4I, as suggested experimentally. X-ray, Brillouin and neutron scattering data obtained for phase III of NH_4I can provide useful information to investigate the anomalous behaviour in this crystalline system.

In this thesis work, we also analyzed the spontaneous polarization and the dielectric constant at various temperatures for constant pressures of 0.001, 1 and 2.2 kbars using the experimental data from the literature close to the ferroelectric-paraelectric phase transition in TSCC. Our values of the critical exponent β for the spontaneous polarization (order parameter) indicate that the ferroelectric phase transition in TSCC changes from the second order to a first order, as the pressure increases. Our exponent values for the susceptibility give the classical value at zero pressure and non-classical values at higher pressures in TSCC. Also, the slopes of the reciprocal dielectric constant 1/ε against the temperature decrease as the pressure increases below and above T_c in TSCC. We performed similar calculations for TSCB under hydrostatic pressures of 1, 2 and 3 kbars and obtained the exponent values as β=0.35 for the spontaneous polarization and $\gamma \approx 1$ for the susceptibility. Those values of the critical exponents

also indicate that TSCB undergoes a second order phase transition as a quantum ferroelectric under hydrostatic pressures of 1, 2 and 3 kbars.

As an another part of this thesis work, by using the experimental data from the literature, we obtained the value of the critical exponent γ through the first and second Pippard relations for carbon tetrachloride (CCl_4) near the melting point. We then calculated the pressure dependence of the isothermal compressibility κ_T and the specific heat C_p for the liquid and solid phases of this compounds, respectively. Our slope values obtained from a linear plot of C_p/V vs. α_p is close to the expected value of 10 MPa/K. The pressure and temperature dependencies of the molar volume were also studied here for the solid and liquid phases of carbon tetrachloride near the melting point. We used the experimental data for the thermal expansivity α_P at 302 K and evaluated the molar volume at various pressures and temperatures in this molecular organic compound. Our results indicate that the molar volume increases as the pressure and temperature increase in solid phase of CCl_4 close to the melting point, whereas in the liquid phase the molar volume is not dependent essentially on the temperature and pressure in the interval studied. The critical behaviour of the molar volume suggests that carbon tetrachloride exhibits a second order phase transformation prior to melting, which can be examined by the experimental measurements.

In order to investigate the dynamical properties of various crystalline systems, we, in particular studied s-triazine because of the experimental data available in the literature. So, the damping constant was calculated here at various temperatures for the Raman mode II of s-triazine near the I-II phase transition (T_c=198 K). The soft mode-hard mode coupling model was used to calculate the damping constant from the shear strain angle (order parameter), which was fitted to the observed halfwidths of the Raman mode II in s-triazine. This model was used to investigate the mechanism of the ferroelastic phase transition in s-triazine since the soft acoustic mode is coupled to optic modes in this crystal. It is concluded here that the soft mode-hard mode coupling model describes

adequately the observed behaviour of s-triazine which undergoes weakly first order or nearly second order transition.

When our results were compared to the experimental values of the studied thermodynamic and spectroscopic quantities, we can see a close agreement between them. This indicates that our method of calculation is convenient to predict the critical behavior of the studied materials. This study can be a step to some other calculations for the physical quantities to examine the observed critical behavior of various molecular crystals. The future observations will also be a way of verifying our predictions which are based on the measurements of the relevant thermodynamic quantities.

REFERENCES

[1] M. E. Fisher, *Rep. Progr. Phys.* **30** (1967) 615.

[2] Wikipedia, http://en.wikipedia.org/wiki/Phase_transition, visited on December 2, 2010.

[3] A. B. Pippard, The Elements of Classical Thermodynamics, Cambridge University Press, New York, 1957.

[4] H. E. Stanley, Introduction to Phase Transitions and Critical Phenomena, Clarendon Press, Oxford , 1971.

[5] R. G. Ross, P. Anderson, *J. Phys. C: Solid State Phys.* **20** (1987) 4745.

[6] R. G. Ross and O. Sandberg, *J. Phys. C: Solid State Phys.* **12** (1979) 3649.

[7] H. A. Levy and S. W. Peterson, *Phys. Rev.* **86** (1952) 766.

[8] S. M. Clark, E. Doorhyee, *J. Phys. Condens. Matter* **4** (1992) 8669.

[9] O. H. Seeck, D. Hupfeld, H. Krull, A. K. Doerr, J. P. Sclomka, M. Tolan and W. Press, *Phys. Rev. B* **59** (1999) 3474.

[10] G. V. Tikhomirova, A. N. Babushkin, *Phys. Stat. Sol. (b)* **235** (2003) 337.

[11] Y. Yamada, M. Mori, Y. Noda, *J. Phys. Soc. Jpn.* **32** (1972) 1565.

[12] A. Hüller, *Z. Phys.* **270** (1974) 343.

[13] V. G. Vaks, V. E. Schneider, *Phys. Stat. Sol. (a)* **35** (1976) 61.

[14] A. A. Vlasova, E. E. Tornau, V. E. Schneider, *Fiz. Tvern. Tela* **20** (1978) 858.

[15] Wikipedia, http://en.wikipedia.org/wiki/Ammonium_chloride, visited on December 5, 2010.

[16] R. C. Leung, C. Zahradnik and C. W. Garland, *Phys. Rev. B* **19** (1979) 2612.

[17] H. Yurtseven, S. Salihoğlu and A. Tüblek, *Phase Trans.* **54** (1995) 151.

[18] Ö. Tarı, H. Yurtseven and S. Salihoğlu, *Phase Trans.* **72** (2000) 351.

[19] B. B. Weiner and C. W. Garland, *J. Chem. Phys.* **56** (1972) 155.

[20] Ammonium iodide, http://www.iodine.com/ammonium.htm , visited on December 5, 2010.

[21] C. H. Perry and R. P. Lowndes, *J. Chem. Phys.* **51** (1969) 3648.

[22] M. Couzi, J. B. Sokoloff and C. H. Perry, *J. Chem. Phys.* **58** (1973) 2965.

[23] H. D. Hochheimer, E. Spanner and D. Strauch, *J. Chem. Phys.* **64** (1976) 1583.

[24] A. M. Heyns, K. R. Hirsch and W. B. Holzapfel, *J. Chem. Phys.* **73** (1980) 105.

[25] Y. C. Xu, W. F. Sherman and G. R. Wilkinson, J. Phys. C, *Solid State Phys.* **20** (1987) L967.

[26] S. Salihoğlu, Ö. Tarı and H. Yurtseven, *Mater. Chem. and Phys.* **73** (2002) 339.

[27] J. R. Durig and D. J. Antion, *J. Chem. Phys.* **51** (1969) 3639.

[28] H. D. Hochheimer and W. Dultz, *Solid State Commun.* **14** (1974) 475.

[29] T. Hikita and T. Maruyama, *J. Phys. Soc. Jpn.* **61** (1992) 2840.

[30] T. Ashida, S. Bando and M. Kakudo, *Acta Crystallogr. B.* **28** (1972) 1560.

[31] N. Mishima, K. Itoh and E. Nakamura, *Acta Crystallogr. C.* **40** (1984) 1824.

[32] V. H. Schmidt, *Solid State Commun.* **35** (1980) 649.

[33] Y. Makita, *J. Phys. Soc. Jpn.* **20** (1965) 2073.

[34] W. W. Windsch and V. H. Schmidt, *Ferroelectrics* **29** (1980) 229.

[35] G. Sorge and U. Straube, *Phys. Stat. Sol. (a)* **51** (1979) 117.

[36] A. Levstik, C. Filipic and R. Blinc, *Solid State Commun.* **18** (1976) 1231.

[37] R. Navalgund and L.C. Gupta, *J. Phys. Soc. Jpn.* **39** (1975) 880.

[38] S. Fujimoto, N. Yasuda and H. Kashiki, *J. Phys. D.* **15** (1982) 487.

[39]Agency for Toxic Substances and Disease Registry (ATSDR), http://www.atsdr.cdc.gov/tfacts30.pdf , visited on December 20, 2010.

[40] Wikipedia, http://en.wikipedia.org/wiki/Carbon_tetrachloride , visited on December 5, 2010.

[41] R. Rudman and B. Post, *Science* **154** (1966) 1009.

[42] K. Kotake, N. Nakamura and H. Chihara, *Bull. Chem. Soc. Jpn.* **40** (1967) 1018.

[43] L. Silver and R. Rudman, *J. Phys. Chem.* **74** (1970) 3134.

[44] J. G. Arentsen and J.C. van Miltenburg, *J. Chem. Thermodyn.* **4** (1972) 789.

[45] Y. Koga and J. A. Morrison, *J. Chem. Phys.* **62** (1975) 3359.

[46] J. A. Morrison and E. L. Richards, *J. Chem. Thermodyn.* **8** (1976) 1033.

[47] J. P. Badiali, J. Bruneaux-Poulle and A. Defrain, *J. Chim. Phys.* **73** (1976) 113.

[48] M. Maruyama, K. Kawabata and N. Kuribayashi, *J. Crystal Growth* **220** (2000) 161.

[49] G. J. Piermarini and A. B. Braun, *J. Chem. Phys.* **58** (1973) 1974.

[50] D.M. Adams and S. K. Sharma, *J. Chem. Soc. Dalton Trans.* **23** (1976) 2424.

[51] C. E. Weir, G. J. Piermarini and S. Block, *J. Chem. Phys.* **50** (1969) 2089.

[52] L. C. Pardo, M. Barrio, J. L. Tamarit, D. O. Lopez, J. Salud, P. Negrier and D. Mondieig, *Chem. Phys. Lett.* **308** (1999) 204.

[53] I. Kanesaka, T. Tamura and Y. Akizawa, *J. Raman Spectrosc.* **30** (1999) 69.

[54] M. Barrio, L. C. Pardo, J. L. Tamarit, P. Negrier, D. O. Lopez, J. Salud and D. Mondieig, *J. Phys. Chem. B.* **108** (2004) 11089.

[55] Ph. Pruzan, D. H. Liebenberg and R. L. Mills, *J. Phys. Chem. Solids* **47** (1986) 949.

[56] M. T. Dove, P. J. S. Ewen, *J. Chem. Phys.* **82** (1985) 2026.

[57] P. Coppens, *Science* **158** (1967) 1577.

[58] P. Coppens and T. M. Sabine, *Mol. Cryst.* **3** (1968) 507.

[59] J. H. Smith and A. I. M. Rae, *J. Phys. C:Solid State Phys.* **11** (1978)1771.

[60] A. I. M. Rae, *J. Phys. C:Solid State Phys.* **11 (**1978**)** 1779.

[61] I. U. Heilmann, W. D. Ellenson and J. Eckert *J. Phys. C* **12 (**1979**)** L185.

[62] M. T. Dove, I. U.Heilmann, J. K. Kjens, J. Kurittu and G. S. Pawley, *Phys. Stat. Solidi (b)* **120 (**1983**)**173.

[63] A. Yoshihara, C. L. Pan, E. R. Bernstein and J. C. Raich, *J. Chem. Phys.* **76 (**1982**)** 3218.

[64] A. I. M. Rae, *J. Chem. Phys.* **70** (1979) 639.

[65] Wikipedia, http://en.wikipedia.org/wiki/Ferroelectrics , visited on December 5, 2010.

[66] Wikipedia, http://en.wikipedia.org/wiki/Electric_polarization , visited on December 5, 2010.

[67] C. Kittel, Introduction to Solid State Physics, 8th ed., J. Wiley and Sons, U.S.A., 2005.

[68] R. K. Pathria, Statistical Mechanics, 2nd ed., Butterworth-Heinemann, Oxford, 1996.

[69] G. S. Rushbrooke and P. J. Wood, *Molec. Phys.* **6** (1963) 409.

[70] M. E. Fisher, *J. Math. Phys.* **5** (1964) 944.

[71] R. B. Griffiths, *Phys. Rev. Lett.* **14** (1965) 623.

[72] D. J. Gardiner, Practical Raman Spectroscopy, Springer-Verlag, New York, LLC, 1989.

[73] Wikipedia, http://en.wikipedia.org/wiki/Raman_spectroscopy , visited on December 20, 2010.

[74] Wikipedia, http://en.wikipedia.org/wiki/Ising_model , visited on February 14, 2011.

[75] H. Yurtseven, S. Salihoglu and S. Şen, *Phys. Stat. Sol. (b)* **244** (2007) 2589.

[76] H. Yurtseven, D. Kavruk, *J. Mol. Struc.* **924-926** (2009) 544.

[77] H. Yurtseven, W. F. Sherman, *J. Mol. Struc.* **115** (1984) 169.

[78] H. Yurtseven, W. F. Sherman, *High Pressure Research,* **4** (1990) 508.

[79] H. Yurtseven, W. F. Sherman, *Phase Trans.* **54** (1995) 1.

[80] D. Kaya and H.Yurtseven, *J. Phys. Chem. Solids,* **68** (2007) 861.

[81] H. Yurtseven and M. H. Tümkaya, *Chem. Phys.* **323** (2006) 574.

[82] C. W. Garland and J. D. Baloga, *Phys. Rev. B* **16** (1977) 331.

[83] H. Yurtseven and D. Kavruk, "Raman frequencies calculated from the volume data as a function of temperature at high pressures for the disordered phase II of NH_4I", *Int. J. Mod. Phys. B, in press.*

[84] V. Hovi and M. Varteva, in: Proceedings of the 9th International Conference on Low Temperature Physics, Part B, Columbus, Ohio (1965) p.1184.

[85] D.Kavruk and H. Yurtseven, *Mod. Phys. Lett. B* **24** (2010) 817.

[86] H. Yurtseven and D. Kavruk, *Ferroelectrics* **367** (2008) 190.

[87] D. Kavruk and H. Yurtseven in: Proceedings of the 24th International Physics Congress, Malatya, Turkey, *Balkan Phys. Lett.*, (2007) p.555.

[88] D. Kaya Kavruk and H. Yurtseven, *High Temp. Mat. Proc.* **26** (2007) 397.

[89] H. Yurtseven and D. Kavruk, *J. Mol. Liq.* **139** (2008) 117.

[90] J. Timmermans, Physico-Chemical Constants of Pure Organic Compounds, Binary Systems in Concentrated Solutions; Interscience Publishers, New York, (1960) Vol. 4, p. 619.

[91] H. Yurtseven and D. Kavruk, *Mod. Phys. Lett. B* **24** (2010) 75.

[92] Y. Yamada, M. Mori and Y. Noda, *J. Phys. Soc. Jpn.* **32** (1972) 1565.

[93] M. Matsushita, *J. Chem. Phys.* **65 (**1975**)** 23.

[94] I. Laulicht and N. Luknar, *Chem. Phys. Letters* **47 (**1977**)** 237

[95] I. Laulicht, *J. Phys. and Chem. Solids* **39** (1978) 901.

[96] G. Lahajnar, R. Blinc and S. Zumer, *Phys. Cond. Matter* **18 (**1974**)** 301.

[97] G. Schaack and V. Winterfeldt, *Ferroelectrics* **15 (**1977**)** 35.

[98] P. J. S. Ewen and M. T. Dove, *Phil. Mag.* B. **47 (**1983**)** 641.

[99] A. I. M. Rae, *J. Phys* C: *Solid State Phys.* **15 (**1982**)** 1883.

[100] D. Kavruk and H. Yurtseven, *Int. J. Mod. Phys. B.* **24** (2010) 369.

[101] C. C. Stephenson, L. A. Landers and A. G. Cole, *J. Chem. Phys.* **20** (1952) 1044.

[102] V. Brajovic, H. Boutin, G. J. Safford and H. Palevsky, *J. Phys. Chem. Solids* **24** (1963) 617.

[103] G. Kosaly and G. Solt, *Physica* **32** (1966) 1571.

[104] A. Compagner, *Physica* **72** (1974) 115.

[105] R. J. Speedy, *J. Phys. Chem.* **86** (1982) 3002.

[106] L. Li Boyer, *Phys. Rev.* **B23** (1981) 3673.

[107] Thermal Expansion, ed. D.C. Larsen, Plenum, New York (1982) p.131.

[108] R. Lipowsky, *Phys. Rev. Lett.* **49** (1982) 1975.

[109] R. Lipowsky and W. Speth, *Phys. Rev.* **B28** (1983) 3983.

[110] J. H. Smith and A. I. M. Rae, *J. Phys.* C. *Solid State Phys.* **11** (1978)1771.

CURRICULUM VITAE

PERSONAL INFORMATION

Surname, Name: Kavruk, Dilan

Date and Place of Birth: November 6th, 1980, Gaziantep

e-mail: dkavruk@eie.gov.tr

EDUCATION

MS	METU Physics	2004
BS	METU Physics Education	2001
High School	Gaziantep Anatolian High School, Gaziantep	1997

PUBLICATIONS

1. Dilan Kaya and Hamit Yurtseven, *J. Phys. Chem. Solids*, **68** (2007) 861.
2. Dilan Kaya Kavruk and Hamit Yurtseven, *High Temp. Mat. Proc.* **26** (2007) 397.
3. D. Kavruk and H. Yurtseven in: Proceedings of the 24th International Physics Congress, Malatya, Turkey, *Balkan Phys. Lett.*, (2007) p.555.
4. Hamit Yurtseven and Dilan Kavruk, *Ferroelectrics* **367** (2008) 190.
5. Hamit Yurtseven and Dilan Kavruk, *J. Mol. Liq.* **139** (2008) 117.
6. Hamit Yurtseven and Dilan Kavruk, *J. Mol. Struc.* **924-926** (2009) 544.
7. Dilan Kavruk and Hamit Yurtseven, *Mod. Phys. Lett. B* **24** (2010) 817.
8. Hamit Yurtseven and Dilan Kavruk, *Mod. Phys. Lett. B* **24** (2010) 75.
9. Dilan Kavruk and Hamit Yurtseven, *Int. J. Mod. Phys. B.* **24** (2010) 369.

10. Hamit Yurtseven and Dilan Kavruk, “Raman frequencies calculated from the volume data as a function of temperature at high pressures for the disordered phase II of NH_4I”, *Int. J. Mod. Phys. B, in press*.